



HAL
open science

The K2 Galactic Archaeology Program Data Release 3: Age-abundance Patterns in C1-C8 and C10-C18

Joel C. Zinn, Dennis Stello, Yvonne Elsworth, Rafael A. García, Thomas Kallinger, Savita Mathur, Benoît Mosser, Marc Hon, Lisa Bugnet, Caitlin Jones, et al.

► **To cite this version:**

Joel C. Zinn, Dennis Stello, Yvonne Elsworth, Rafael A. García, Thomas Kallinger, et al.. The K2 Galactic Archaeology Program Data Release 3: Age-abundance Patterns in C1-C8 and C10-C18. The Astrophysical Journal, 2022, 926, 10.3847/1538-4357/ac2c83 . insu-03713338

HAL Id: insu-03713338

<https://insu.hal.science/insu-03713338>

Submitted on 4 Jul 2022

HAL is a multi-disciplinary open access archive for the deposit and dissemination of scientific research documents, whether they are published or not. The documents may come from teaching and research institutions in France or abroad, or from public or private research centers.

L'archive ouverte pluridisciplinaire **HAL**, est destinée au dépôt et à la diffusion de documents scientifiques de niveau recherche, publiés ou non, émanant des établissements d'enseignement et de recherche français ou étrangers, des laboratoires publics ou privés.



Distributed under a Creative Commons Attribution 4.0 International License



The K2 Galactic Archaeology Program Data Release 3: Age-abundance Patterns in C1–C8 and C10–C18

Joel C. Zinn^{1,2,25} , Dennis Stello^{2,3,4,5} , Yvonne Elsworth^{4,6} , Rafael A. García⁷ , Thomas Kallinger⁸ , Savita Mathur^{9,10} ,
Benoît Mosser¹¹ , Marc Hon² , Lisa Bugnet^{7,12} , Caitlin Jones⁶ , Claudia Reyes² , Sanjib Sharma^{3,5} , Ralph Schönrich¹³ ,
Jack T. Warfield^{14,15} , Rodrigo Luger^{16,17} , Andrew Vanderburg¹⁸ , Chiaki Kobayashi¹⁹ , Marc H. Pinsonneault¹⁴ ,
Jennifer A. Johnson¹⁴ , Daniel Huber²⁰ , Sven Buder^{5,21} , Meridith Joyce^{5,21} , Joss Bland-Hawthorn^{3,5} ,
Luca Casagrande²² , Geraint F. Lewis³ , Andrea Miglio^{4,6} , Thomas Nordlander^{5,21} , Guy R. Davies^{4,6} ,
Gayandhi De Silva^{5,23,24} , William J. Chaplin^{4,6} , and Victor Silva Aguirre⁴ 

¹ Department of Astrophysics, American Museum of Natural History, Central Park West at 79th Street, New York, NY 10024, USA; jzinn@amnh.org

² School of Physics, University of New South Wales, Barker Street, Sydney, NSW 2052, Australia

³ Sydney Institute for Astronomy, School of Physics, A28, The University of Sydney, NSW 2006, Australia

⁴ Stellar Astrophysics Centre, Department of Physics and Astronomy, Aarhus University, Ny Munkegade 120, DK-8000 Aarhus C, Denmark

⁵ ARC Centre of Excellence for All Sky Astrophysics in 3 Dimensions (ASTRO 3D), Australia

⁶ School of Physics and Astronomy, University of Birmingham, Edgbaston, Birmingham, B15 2TT, UK

⁷ AIM, CEA, CNRS, Université Paris-Saclay, Université Paris Diderot, Sorbonne Paris Cité, F-91191 Gif-sur-Yvette, France

⁸ Institute of Astrophysics, University of Vienna, Türkenschanzstrasse 17, Vienna 1180, Austria

⁹ Instituto de Astrofísica de Canarias, La Laguna, Tenerife, Spain

¹⁰ Departamento de Astrofísica, Universidad de La Laguna, La Laguna, Tenerife, Spain

¹¹ LESIA, Observatoire de Paris, PSL Research University, CNRS, Sorbonne Université, Université de Paris Diderot, 92195 Meudon, France

¹² Flatiron Institute, Simons Foundation, 162 Fifth Ave, New York, NY 10010, USA

¹³ Mullard Space Science Laboratory, University College London, Holmbury St Mary, Dorking RH5 6NT, UK

¹⁴ Department of Astronomy, The Ohio State University, 140 West 18th Avenue, Columbus OH 43210, USA

¹⁵ Department of Physics, The Ohio State University, 191 West Woodruff Avenue, Columbus OH 43210, USA

¹⁶ Center for Computational Astrophysics, Flatiron Institute, New York, NY, USA

¹⁷ Virtual Planetary Laboratory, University of Washington, Seattle, WA, USA

¹⁸ Department of Astronomy, The University of Texas at Austin, Austin, TX 78712, USA

¹⁹ Centre for Astrophysics Research, Department of Physics, Astronomy and Mathematics, University of Hertfordshire, Hatfield, AL10 9AB, UK

²⁰ Institute for Astronomy, University of Hawai'i, 2680 Woodlawn Drive, Honolulu, HI 96822, USA

²¹ Research School of Astronomy and Astrophysics, Australian National University, Canberra, ACT 2611, Australia

²² Research School of Astronomy and Astrophysics, Mount Stromlo Observatory, The Australian National University, ACT 2611, Australia

²³ Australian Astronomical Optics, Faculty of Science and Engineering, Macquarie University, Macquarie Park, NSW 2113, Australia

²⁴ Macquarie University Research Centre for Astronomy, Astrophysics & Astrophotonics, Sydney, NSW 2109, Australia

Received 2021 March 26; revised 2021 September 9; accepted 2021 September 13; published 2022 February 24

Abstract

We present the third and final data release of the K2 Galactic Archaeology Program (K2 GAP) for Campaigns C1–C8 and C10–C18. We provide asteroseismic radius and mass coefficients, κ_R and κ_M , for $\sim 19,000$ red giant stars, which translate directly to radius and mass given a temperature. As such, K2 GAP DR3 represents the largest asteroseismic sample in the literature to date. K2 GAP DR3 stellar parameters are calibrated to be on an absolute parallactic scale based on Gaia DR2, with red giant branch and red clump evolutionary state classifications provided via a machine-learning approach. Combining these stellar parameters with GALAH DR3 spectroscopy, we determine asteroseismic ages with precisions of $\sim 20\%$ – 30% and compare age-abundance relations to Galactic chemical evolution models among both low- and high- α populations for α , light, iron-peak, and neutron-capture elements. We confirm recent indications in the literature of both increased Ba production at late Galactic times as well as significant contributions to r -process enrichment from prompt sources associated with, e.g., core-collapse supernovae. With an eye toward other Galactic archeology applications, we characterize K2 GAP DR3 uncertainties and completeness using injection tests, suggesting that K2 GAP DR3 is largely unbiased in mass/age, with uncertainties of 2.9% (stat.) $\pm 0.1\%$ (syst.) and 6.7% (stat.) $\pm 0.3\%$ (syst.) in κ_R and κ_M for red giant branch stars and 4.7% (stat.) $\pm 0.3\%$ (syst.) and 11% (stat.) $\pm 0.9\%$ (syst.) for red clump stars. We also identify percent-level asteroseismic systematics, which are likely related to the time baseline of the underlying data, and which therefore should be considered in TESS asteroseismic analysis.

Unified Astronomy Thesaurus concepts: Red giant stars (1372); Nucleosynthesis (1131); R-process (1324); S-process (1419); Galactic archaeology (2178); Stellar ages (1581); Asteroseismology (73)

Supporting material: machine-readable tables

²⁵ NSF Astronomy and Astrophysics Postdoctoral Fellow.

1. Introduction

Studies of Galactic chemical evolution have mostly focused on targets in the solar neighborhood, in which stars are relatively easy to observe, and which was the sole domain, historically, of precise parallaxes and, therefore, stellar ages

(e.g., Nordström et al. 2004). Because stars for the most part maintain their birth abundances, stellar abundances and ages can be used to infer the chemical enrichment history of the Galaxy, providing information about the details of contributions to the interstellar medium from nucleosynthetic channels like supernovae and stellar winds.

The local stellar population has been found to have a bimodal chemical distribution in α elements (e.g., O, Mg, Ca, and Si), as seen in $[\alpha/\text{Fe}]$ versus $[\text{Fe}/\text{H}]$:²⁶ there exists one population of low- α stars with spatial distributions apparently more confined to the plane of the Galaxy and with intermediate to young ages, and there exists another population of high- α stars with hotter kinematics, centrally concentrated spatial distributions in the disk, and older ages (e.g., Fuhrmann 1998; Gratton et al. 2000; Prochaska et al. 2000; Bensby et al. 2003; Haywood et al. 2013). With the understanding that α elements are produced primarily in core-collapse supernovae (CCSNe), with some contributions to the heavier nuclei being from Type Ia supernovae (SNe Ia), whereas iron is mostly produced in SNe Ia, the low- α population has been interpreted as mostly having contributions from SNe Ia, and the high- α population has been interpreted as mostly having contributions from CCSNe (Burbidge et al. 1957; Timmes et al. 1995).

Studies of stellar populations beyond the solar neighborhood have shown that the low- α and high- α populations maintain their chemical bimodality, and, to a certain extent, their distinct radial spatial distributions, with the high- α stars being more centrally concentrated (Nidever et al. 2014; Hayden et al. 2015), though not necessarily having a different intrinsic vertical spatial distribution (Hayden et al. 2017). There are also interesting chemical distinctions between these populations when looking at non- α -element abundance ratios (e.g., Prochaska et al. 2000; Bensby et al. 2003; Adibekyan et al. 2012; Griffith et al. 2019; Weinberg et al. 2019; Nissen et al. 2020). Given the expectation that the bimodality is ultimately related to different chemical enrichment histories, it is natural to ask how these populations evolved, and, in so doing, test understandings of the nucleosynthetic production sites’ yields with time. Indeed, the underlying origin of these spatial and chemical distinctions is under debate (e.g., Chiappini et al. 1997; Schönrich & Binney 2009a, 2009b; Kobayashi & Nakasato 2011; Minchev et al. 2015; Hayden et al. 2017; Mackereth et al. 2018; Clarke et al. 2019; Spitoni et al. 2019).

Thanks to an unprecedented collection of well-measured stellar kinematics from Gaia (Gaia Collaboration et al. 2016, 2018), and with large spectroscopic surveys like APOGEE (Majewski et al. 2017), GALactic Archaeology with HERMES (GALAH; De Silva et al. 2015), and LAMOST (Newberg et al. 2012) providing hundreds of thousands of detailed abundance measurements probing well beyond the solar vicinity, the bottleneck to progress on the origin and evolution of the elements in the Galaxy becomes the stellar age.

Stellar composition has historically been used as a proxy for stellar age, based on the idea that Galactic enrichment increases with time, with inputs to the interstellar medium through asymptotic giant branch (AGB) stars, SNe Ia, and CCSNe continually injecting metals over time according to so-called delay-time distributions, in ratios that themselves depend on time, due to the birth compositions of the stars producing the

changing elements (Tinsley 1979; McWilliam 1997). Kinematic information can also serve as an age proxy, with older stellar populations experiencing dynamical heating from discrete merger events (e.g., Grand et al. 2016) as well as from secular processes involving, e.g., spiral arms (Carlberg & Sellwood 1985; Minchev & Quillen 2006), the central bar (Saha et al. 2010; Grand et al. 2016), and giant molecular clouds (e.g., Spitzer & Schwarzschild 1951).

To make precise statements about the chemical evolution of the Galaxy, however, requires genuine stellar age estimates independent of kinematics and abundances, so as to not assume the age-abundance patterns under question. Work appealing to stellar ages in order to solve this conundrum has either made recourse to turnoff stars—whose ages can be reliably determined through isochrone matching (Pont & Eyer 2004; Jørgensen & Lindegren 2005; Lin et al. 2020), but which are relatively dim, and therefore probe predominantly local volumes—or to spectroscopic ages (e.g., Ness et al. 2016; Sun et al. 2020). Although machine learning-based spectroscopic ages have increased sample sizes to hundreds of thousands, they do not seem to yield reliable results for ages > 8 Gyr (Ting & Rix 2019). Another approach is to make reference to Galactic stellar population models, and match the predicted age-color relation to the observed colors (e.g., Bland-Hawthorn et al. 2019). As we will show here, such photometric ages—with typical uncertainties of 30%–50%—are significantly less precise than the 20%–30% K2 asteroseismic age uncertainties we present here.

Because asteroseismic ages do not assume either an age-kinematics relation or an age-metallicity relation, they can provide interesting constraints on Galactic chemical evolution. Indeed, asteroseismic ages have supported the estimates in the literature that the two α populations have different age distributions (e.g., Silva Aguirre et al. 2018; Miglio et al. 2021), while complicating the understanding that the high- α population is uniformly old (Chiappini et al. 2015; Anders et al. 2017; Warfield et al. 2021). These studies have mostly been limited to asteroseismic data from the Kepler mission (Borucki et al. 2010), which probes a single, 100 sq. deg. field of view at a roughly fixed Galactic radius corresponding to that of the Sun. With the extended Kepler mission, K2 (Howell et al. 2014), has access to regions of the sky across the ecliptic, and exploratory work based on data from the four K2 campaigns has shown promise in terms of better understanding the α bimodality (Rendle et al. 2019; Warfield et al. 2021). The K2 Galactic Archaeology Program (GAP; Stello et al. 2015) takes advantage of this opportunity, targeting red giant stars with the express intent of investigating the chemical evolution of the Galaxy beyond the solar vicinity using asteroseismic ages.

In this paper, we describe the final data release of K2 GAP, which combines the red giant asteroseismic data from Campaign 1 (C1) of K2 GAP DR1 (Stello et al. 2017) and the data from C4, C6, and C7 of K2 GAP DR2 (Zinn et al. 2020) with results from the remaining K2 campaigns. In K2 GAP Data Release 3 (DR3), we improve upon K2 GAP DR2 by verifying the accuracy and precision of asteroseismology with an injection test exercise, and calibrate our results against Gaia DR2 (Gaia Collaboration et al. 2018) radii.²⁷ Finally, we

²⁶ Here and throughout the paper we use the standard notation $[X/\text{Fe}] \equiv \log_{10}\left(\frac{X}{\text{Fe}}\right) - \log_{10}\left(\frac{X_{\odot}}{\text{Fe}_{\odot}}\right)$.

²⁷ Here and throughout the text, when we mention Gaia radii, we refer to the radii we calculate using APOGEE spectroscopy and Gaia parallaxes, according to the Stefan-Boltzmann law. These radii are distinct from the `radius_val` values provided as part of Gaia DR2; the latter are not as accurate as we require here, because they do not account for extinction and assume inhomogeneous temperatures. See Section 4 for details.

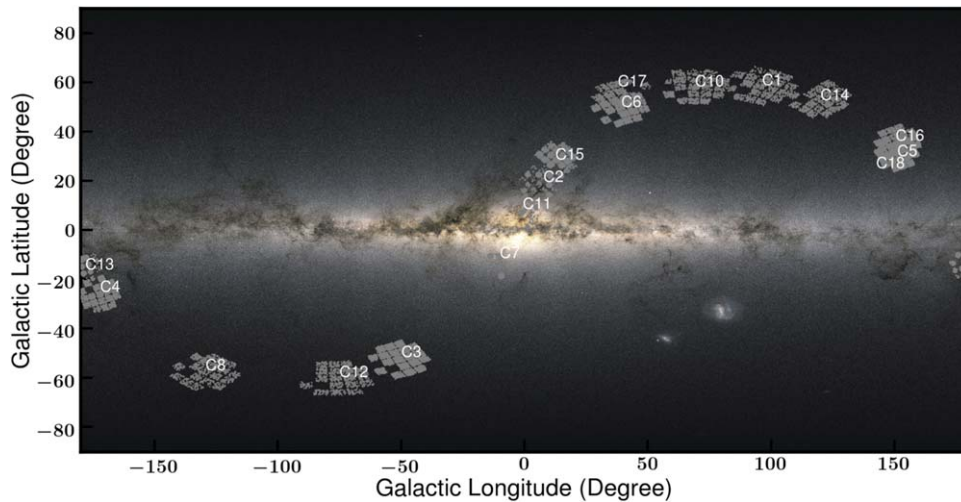


Figure 1. Distribution of the K2 GAP sample across the sky. Targets in dense fields close to the Galactic plane were selected only within 1° circles centered on each module, rather than across entire modules. Also visible are the rectangular gaps corresponding to CCD modules 3 and 7, which failed prior to the start of the K2 mission, and module 4, which failed during C10. Background image is modified from ESA/Gaia/DPAC.

derive ages based on these calibrated asteroseismic masses in order to compare abundance enrichment histories of low- and high- α populations with Galactic chemical evolution models from Kobayashi et al. (2020a).

2. Data

2.1. Asteroseismic Data

In this data release, we add asteroseismic data from C2, C3, C5, C8, and C10–C18 to the results from C1 of K2 GAP DR1 (Stello et al. 2017) and C4, C6, and C7 of K2 GAP DR2 (Zinn et al. 2020). In what follows, we describe the procedure used to derive the asteroseismic values for the stars in these new campaigns, and we also describe how the results from all of the campaigns have been combined together.

The majority of K2 GAP targets were chosen to satisfy simple color and magnitude cuts, with a minority being chosen based on surface gravity selections from spectroscopic surveys—APOGEE (Majewski et al. 2010), SEGUE (Yanny et al. 2009), and RAVE (Steinmetz et al. 2006). Most of the campaigns have targets that were chosen based on a $J - K_s > 0.5$ color cut and a magnitude cut of $9 \lesssim V \lesssim 15$, where the visual magnitude was computed from Two Micron All Sky Survey photometry according to

$$V \approx K_s + 2((J - K_s) + 0.14) + 0.256e^{2(J - K_s)},$$

which is a relation introduced by De Silva et al. (2015). The targets were prioritized for the most part by ranking targets in order of brightest to faintest visual magnitude, with higher priority being given to targets selected based on spectroscopy.

The majority of the targeted stars were observed by K2, and follow the target selection functions, with a few exceptions. Notably, the priorities of C7 targets were mistakenly reversed during the Kepler office target list consolidation. For details of the effects of this on the C7 selection function, see Zinn et al. (2020) and Sharma et al. (2019); the selection functions for all of the campaigns are described in S. Sharma et al. (2021, in preparation). In addition, module 4 failed while taking data in C10. We therefore excluded data from this module in C10 because of the short duration of the data collection before the failure; modules 3 and 7 had already failed by the time when

the K2 mission had begun, and so there are no data for these modules in K2 GAP. These missing modules can be seen in the K2 GAP DR3 footprint shown in Figure 1.

There are known systematics in the K2 light curves that require special processing beyond the raw light curves produced by the K2 office. In particular, the K2 satellite repositioned itself every ~ 6 hr to maintain pointing following the partial failure of its gyroscope system. These thruster firings induce trends in the light curves that would hinder asteroseismic analysis. The light curves used in our analysis were therefore detrended from the raw K2 data using the EVEREST pipeline (Luger et al. 2018) for all of the observed K2 GAP target stars, except C1, for which we used the K2SFF pipeline (Vanderburg & Johnson 2014), and the targets classified as extended in the Ecliptic Plane Input Catalog (EPIC; Huber et al. 2016), which were not processed by EVEREST. C10 suffered a failure of module 4 shortly into the start of the campaign, and so we did not use data from targets on module 4. C11 was separated into two parts due to a roll angle correction, such that some stars had light curves only for one part of the campaign; when available, we combined the light curves of the two parts for the same target. C18 lasted about 50 days, due to the spacecraft running low on fuel, and has correspondingly reduced-quality data. C19 only had about a week’s worth of data with pointing comparable to the previous campaigns, and, as such, we have not considered the data from C19 in this data release.

Following this detrending, we removed nonasteroseismic variability using a boxcar high-pass filter with a width of 4 days, and performed sigma clipping to reject flux values more than $4\text{-}\sigma$ discrepant. For the campaigns new to this data release, we additionally regularized the spectral window function by inpainting any gaps in the light curves according to the algorithm of García et al. (2014) and Pires et al. (2015).

2.2. Spectroscopic Data

APOGEE DR16 (Ahumada et al. 2020) spectroscopic data have been used to calibrate the asteroseismic data (Section 4). APOGEE DR16 is part of Sloan Digital Sky Survey IV (Blanton et al. 2017), which is described in Ahumada et al. (2020). APOGEE observes in the H -band using the

high-resolution ($R \sim 22,500$) APOGEE spectrograph (Wilson et al. 2019) mounted on the Sloan Foundation 2.5 m telescope (Gunn et al. 2006) at Apache Point Observatory. APOGEE observes about half of its targets in the disk, with Galactic latitude $b \leq 16^\circ$, with dedicated selections of the bulge, halo, and special programs comprising the rest of its observing allotment. Targets are selected according to color–magnitude cuts of $J - K_s \geq 0.5$ and $7 \lesssim H \lesssim 14$, across the sky (Zasowski et al. 2013, 2017). The data are reduced according to Nidever et al. (2015), using the APOGEE Stellar Parameters and Chemical Abundances Pipeline (Holtzman et al. 2015; García Pérez et al. 2016). The final stellar parameter calibration and validation process is discussed by Holtzman et al. (2018).

GALAH data have been used for our analysis of age-abundance patterns (Section 5). GALAH is an optical spectroscopic survey targeting stars in the Galactic disk with $12 < V < 14$ and $|b| > 10^\circ$ (Martell et al. 2017). The survey operates from the 3.9 m Anglo-Australian Telescope at Siding Spring Observatory in Australia, using the HERMES multi-object spectrograph (Sheinis et al. 2014). The HERMES high-resolution ($R \sim 28,000$) spectra are reduced according to the procedure documented in Kos et al. (2017). GALAH DR2 presented spectroscopic parameters from the Cannon (Ness et al. 2015), trained on a subset of $\sim 11,000$ stars (Heiter et al. 2015; Buder et al. 2018) using Spectroscopy Made Easy (SME; Valenti & Piskunov 1996; Piskunov & Valenti 2017). In this work, we use abundances from GALAH DR3, which improves upon GALAH DR2 by deriving stellar parameters and abundances for all stars directly through the spectroscopic analysis code SME, which performs on-the-fly spectrum synthesis calculations; this reduces potential bias from selection effects in the Cannon training process (e.g., Holtzman et al. 2018). The SME analysis code utilizes grids of precomputed non-LTE departure coefficients for thirteen chemical elements; these grids and the models they are based on are presented by Amarsi et al. (2020, and references therein) and are publicly available (Amarsi 2020).

3. Methods

3.1. Asteroseismic Radius and Mass Scaling Relations

Given the large sample size of the K2 GAP targets, it is not feasible to fit individual modes for each star in order to determine their mass and radius. Instead, we condense the modes’ information into two quantities, which can be measured relatively straightforwardly and which are related to the mass and radius of a star through so-called scaling relations.

The first of these quantities, the frequency at maximum acoustic power, ν_{\max} , is thought to be related to the acoustic cutoff frequency, and therefore to the surface gravity of the star (Brown et al. 1991; Kjeldsen & Bedding 1995; Chaplin et al. 2008; Belkacem et al. 2011). Assuming that this relation holds homologically across evolutionary state, this implies a scaling relation of the form

$$\frac{\nu_{\max}}{\nu_{\max,\odot}} \approx \frac{M/M_\odot}{(R/R_\odot)^2 \sqrt{T_{\text{eff}}/T_{\text{eff},\odot}}}. \quad (1)$$

The second quantity of interest, the large frequency separation, $\Delta\nu$, describes the frequency difference between modes of consecutive radial order that share the same degree. A second, independent scaling relation relates $\Delta\nu$ to the average

stellar density (Ulrich 1986; Kjeldsen & Bedding 1995):

$$\frac{\Delta\nu}{\Delta\nu_\odot} \approx \sqrt{\frac{M/M_\odot}{(R/R_\odot)^3}}. \quad (2)$$

The latter scaling relation is well understood theoretically, and is valid, strictly speaking, in the limit of large radial order. However, given a stellar structure model, one can compute the expected $\Delta\nu$ at the observed radial order, as well as $\Delta\nu$ in the limit of large radial order, and therefore derive a correction factor, $f_{\Delta\nu}$, to translate the observed $\Delta\nu$ to the large radial order $\Delta\nu$ that enters into Equation (2) (e.g., White et al. 2011; Sharma et al. 2016). We therefore use a modified version of Equation (2):

$$\frac{\Delta\nu}{f_{\Delta\nu} \Delta\nu_\odot} \approx \sqrt{\frac{M/M_\odot}{(R/R_\odot)^3}}. \quad (3)$$

Note that these corrections do not take into account frequency shifts due to the approximations of adiabatic thermal structures and mixing length theory that are widely used in stellar evolution models (e.g., Jørgensen et al. 2020, 2021). However, such considerations are secondary adjustments to $f_{\Delta\nu}$, given the empirical success of $f_{\Delta\nu}$ in producing agreement between asteroseismic radii and masses with independent estimates (e.g., Huber et al. 2017; Brogaard et al. 2018; Zinn et al. 2019b). We opt to use the $f_{\Delta\nu}$ corrections from Sharma et al. (2016), which are computed on a star-by-star basis according to the star’s properties (e.g., temperature, metallicity, etc.), by interpolation in a grid of theoretically computed $f_{\Delta\nu}$. The `asfgrid` code for computing $f_{\Delta\nu}$ values is publicly available (Sharma & Stello 2016; Sharma et al. 2016).²⁸

In analogy with the corrections to the $\Delta\nu$ scaling relation, there are observational indications that the ν_{\max} scaling relation of Equation (1) should also be modified to include a correction to the observed ν_{\max} , $f_{\nu_{\max}}$ (Epstein et al. 2014; Yıldız et al. 2016; Huber et al. 2017; Viani et al. 2017; Kallinger et al. 2018). For this reason, we use a modified ν_{\max} scaling relation:

$$\frac{\nu_{\max}}{f_{\nu_{\max}} \nu_{\max,\odot}} \approx \frac{M/M_\odot}{(R/R_\odot)^2 \sqrt{(T_{\text{eff}}/T_{\text{eff},\odot})}}. \quad (4)$$

Although progress is being made in terms of making robust theoretical predictions of ν_{\max} (e.g., Belkacem et al. 2013; Zhao et al. 2016; Zhou et al. 2020), it cannot yet be computed, based on first principles, to the precision required to be useful, as can be done for $\Delta\nu$. We therefore make empirical estimates of $f_{\nu_{\max}}$ in Section 4 for red giant branch (RGB) and red clump (RC) stars, which, in practice, are scalar values such that we can think of $f_{\nu_{\max}}$ as indistinguishable from a modified $\nu_{\max,\odot}$.

The solar reference values in Equations (3) and (4) should, in theory, be measured using the same analysis as one would use to measure ν_{\max} and $\Delta\nu$. Therefore, each pipeline has different solar reference values, which are listed in Table 1. We assume here a solar temperature of $T_{\text{eff},\odot} = 5772\text{K}$ (Mamajek et al. 2015).

By rearranging Equations (3) and (4), the radius scaling relation is found to be

$$\frac{R}{R_\odot} \approx \left(\frac{\nu_{\max}}{f_{\nu_{\max}} \nu_{\max,\odot}} \right) \left(\frac{\Delta\nu}{f_{\Delta\nu} \Delta\nu_\odot} \right)^{-2} \left(\frac{T_{\text{eff}}}{T_{\text{eff},\odot}} \right)^{1/2} \quad (5)$$

²⁸ <http://www.physics.usyd.edu.au/k2gap/Asfgrid/>

Table 1
Solar Reference Values for each Pipeline Contributing to K2 GAP DR3

Pipeline	$\nu_{\max,\odot}$	$\Delta\nu_{\odot}$
A2Z	3097.33	134.92
CAN	3140	134.92
COR	3050	134.92
SYD	3090	135.1
BAM	3094	134.84
BHM	3050	134.92

$$\equiv \kappa_R \left(\frac{T_{\text{eff}}}{T_{\text{eff},\odot}} \right)^{1/2}, \quad (6)$$

and the mass scaling relation expression is found to be

$$\frac{M}{M_{\odot}} \approx \left(\frac{\nu_{\max}}{f_{\nu_{\max}} \nu_{\max,\odot}} \right)^3 \left(\frac{\Delta\nu}{f_{\Delta\nu} \Delta\nu_{\odot}} \right)^{-4} \left(\frac{T_{\text{eff}}}{T_{\text{eff},\odot}} \right)^{3/2} \quad (7)$$

$$\equiv \kappa_M \left(\frac{T_{\text{eff}}}{T_{\text{eff},\odot}} \right)^{3/2}. \quad (8)$$

Here, we have factored out the dependence on temperature. Since the majority of the K2 GAP DR3 stars do not have spectroscopic temperature estimates, we report, as we did in K2 GAP DR2, the radius and mass coefficients, κ_R and κ_M . This allows the user to compute radii and masses using consistent temperature scales in the context of their work. We also provide the $f_{\Delta\nu}$ that we computed according to Sharma et al. (2016) in Table 2; though, in order to maintain complete consistency, users should recompute these values using the same temperature scale as they use to convert radius and mass coefficients into radii and masses. For reference, should there be a 100K discrepancy between the EPIC temperatures used to compute $f_{\Delta\nu}$ here and the user's temperatures, a 1% systematic would be introduced into $f_{\Delta\nu}$. Users may generate their own $f_{\Delta\nu}$ values using the publicly available `asfgrid` code.

3.2. Derived Asteroseismic Parameters

We make use of the same pipelines as the previous K2 GAP data releases in order to extract aforementioned asteroseismic quantities, ν_{\max} and $\Delta\nu$, from K2 light curves: A2Z (Mathur et al. 2010), BAM (Zinn et al. 2019c), BHM (Hekker et al. 2010), CAN (Kallinger et al. 2010, 2016), COR (Mosser & Appourchaux 2009; Mosser et al. 2010), and SYD (Huber et al. 2009). The generalized problem that each of these pipelines addresses is identification of a regular pattern of solar-like oscillations in the presence of red and white noise. The problem of detecting solar-like oscillations in K2 data also involves systematic noise that can mimic solar-like oscillations (see Stello et al. 2017; Zinn et al. 2019c). Though their implementations vary, the above asteroseismic pipelines share common approaches of (1) fitting a model to the power spectrum to remove the stellar red noise; (2) fitting a Gaussian excess in power above the red noise, with a mean corresponding to ν_{\max} (A2Z, BAM, BHM, CAN, and COR), or heavily smoothing the excess to localize the frequency of its peak as ν_{\max} (SYD); and (3) identifying $\Delta\nu$ using either individually fitted modes (CAN) or some version of the autocorrelation function (A2Z, BAM, BHM, CAN, COR, and SYD). For more details of implementation and methodologies of these pipelines

in the context of K2, please see Stello et al. (2017) and Zinn et al. (2020).²⁹

We follow the procedure laid out in K2 GAP DR2 to derive average asteroseismic parameters for each star. This method is similar to the one adopted for the APOKASC-2 sample, which is described in Pinsonneault et al. (2018). In short, we rescale each of the pipeline ν_{\max} and $\Delta\nu$ values such that the average values for the entire sample across all of the pipelines are the same, which requires an iterative approach and results in averaged values for each star, denoted by $\langle \nu'_{\max} \rangle$ and $\langle \Delta\nu' \rangle$. Three modifications have been implemented here compared to the methodology described in Zinn et al. (2020). First, the A2Z $\Delta\nu$ values are not incorporated into the $\langle \Delta\nu' \rangle$, due to a significant systematic offset from the other pipeline values. Second, for stars that were observed during more than one campaign, variance-weighted averages for each pipeline are computed before proceeding, such that there is only one measurement per star. Third, whereas previously the sigma clipping was done at the end of each iteration, we now allow the average ν_{\max} to converge before performing a 3σ clipping and continuing the iteration process. For each star that has at least two pipeline values returned, we take the average ν_{\max} value, $\langle \nu'_{\max} \rangle$, and adopt the scatter in those ν_{\max} values as the uncertainty on ν_{\max} , $\sigma_{\langle \nu'_{\max} \rangle}$. The same exercise is performed for $\Delta\nu$, to compute $\langle \Delta\nu' \rangle$ and $\sigma_{\langle \Delta\nu' \rangle}$. In so doing, we are assuming that the different pipelines have systematic differences in the $\Delta\nu$ and ν_{\max} measurements that tend to cancel each other out when averaged together. This exercise is conducted separately for RGB and RC stars, based on the evolutionary states computed using the machine-learning approach described in Hon et al. (2017, 2018). In brief, the machine-learning approach takes advantage of the fact that RGB and RC stars exhibit differences in the observed mode structure (Bedding et al. 2011). These differences are detectable by visual inspection, and are therefore amenable to being learned by machine-learning algorithms. The classifier developed by Hon et al. (2017, 2018) uses a convolutional neural network—an architecture optimized for image processing—to learn characteristic red giant and red clump mode features that are present in power spectra rendered as 2D images. In this work, evolutionary states are assigned arbitrarily at the initial iteration, and in subsequent iterations, for stars with defined $\langle \Delta\nu' \rangle$ and $\langle \nu'_{\max} \rangle$, machine-learning evolutionary states are assigned. The final iteration proceeds only with stars with a defined $\langle \Delta\nu' \rangle$ and $\langle \nu'_{\max} \rangle$. As part of this process, each pipeline has assigned scale factors— $X_{\nu_{\max},\text{RGB}}$, $X_{\Delta\nu,\text{RGB}}$, $X_{\nu_{\max},\text{RC}}$, and $X_{\Delta\nu,\text{RC}}$ —that describe by how much the pipeline-specific solar reference value (Table 1) should be multiplied to be put on the $\langle \nu'_{\max} \rangle$ and $\langle \Delta\nu' \rangle$ scale for RGB stars and RC stars, respectively. These modified solar reference values are provided in Table 3. Here, we also indicate the analogous scaling factors from APOKASC-2 (Pinsonneault et al. 2018), where differences are the result of a slightly different methodology and not working with the same pipelines: BAM was not a part of the APOKASC-2 analysis. It is also likely that significant differences were introduced in the pipeline's

²⁹ The following changes were implemented in the SYD pipeline compared to its description and use in K2 GAP DR2: (1) in addition to the nominal ν_{\max} and $\Delta\nu$ confidence cuts mentioned in Zinn et al. (2020), stars are required to fall within the empirical $\Delta\nu$ - ν_{\max} relation from Stello et al. (2009), such that $0.75(0.262\nu_{\max}^{0.772}) < \Delta\nu < 1.5(0.262\nu_{\max}^{0.772})$; and (2) the stars for which $\Delta\nu$ was deemed measurable were determined based on a machine-learning approach from an independent analysis of the K2 data (Reyes et al. 2022).

Table 2
Derived Asteroseismic ν_{\max} and $\Delta\nu$ Values

EPIC ID	$\langle\nu'_{\max}\rangle$ μHz	$\sigma(\nu'_{\max})$ μHz	$\varsigma(\nu'_{\max})$ μHz	$N_{\nu'_{\max}}$	$\langle\Delta\nu'\rangle$ μHz	$\sigma(\Delta\nu')$ μHz	$\varsigma(\Delta\nu')$ μHz	$N_{\Delta\nu'}$	X_{Sharma}	$\sigma_{X_{\text{Sharma}}}$	$\langle\Delta\nu\rangle$ μHz	$\nu'_{\max,\text{A2Z}}$ μHz	$\nu'_{\max,\text{BAM}}$ μHz	$\nu'_{\max,\text{BHM}}$ μHz	$\nu'_{\max,\text{CAN}}$ μHz	$\nu'_{\max,\text{COR}}$ μHz	$\nu'_{\max,\text{SYD}}$ μHz	$\Delta\nu'_{\text{A2Z}}$ μHz	$\Delta\nu'_{\text{BAM}}$ μHz	$\Delta\nu'_{\text{BHM}}$ μHz	$\Delta\nu'_{\text{CAN}}$ μHz	$\Delta\nu'_{\text{COR}}$ μHz	$\Delta\nu'_{\text{SYD}}$ μHz	EPIC K	T_{eff} K	σ_T K	EPIC [Fe/H]	$\sigma_{[\text{Fe}/\text{H}]}$
210306475	28.041	1.274	1.495	5	3.495	0.112	0.176	3	1.026	0.008	3.405	28.575	30.053	26.808	27.801	...	29.351	...	3.361	3.568	3.539	4797	134	-0.266	0.300	
210307958	28.380	0.933	1.308	5	3.965	0.134	0.100	3	1.032	0.014	3.842	27.964	30.233	...	29.399	28.349	28.369	...	3.852	...	4.112	3.925	...	4750	138	-0.359	0.260	
210314854	30.482	1.034	1.669	6	4.171	0.064	0.129	5	1.017	0.019	4.102	29.055	31.776	31.093	30.745	31.639	31.693	...	4.201	4.169	4.119	4.268	4.112	4953	174	-0.510	0.330	
210315825	58.454	0.341	1.990	6	6.093	0.059	0.096	5	1.025	0.011	5.944	59.632	59.091	59.795	59.671	58.958	59.540	...	6.065	6.175	6.083	6.123	6.018	4827	180	-0.298	0.300	
210318976	24.052	0.501	1.350	5	3.541	0.043	0.083	2	1.031	0.014	3.434	24.821	25.012	...	23.772	24.539	24.162	3.568	3.507	...	4680	140	-0.199	0.260	

Note. Asteroseismic values rescaled for scalar offsets among pipelines are denoted by a prime (the pipeline-specific solar reference scale factors are listed in Table 3); mean ν_{\max} and $\Delta\nu$ values for each star across all pipelines are denoted by $\langle\nu'_{\max}\rangle$ and $\langle\Delta\nu'\rangle$; the standard deviations of these values for each star across all pipelines are denoted by $\sigma(\nu'_{\max})$ and $\sigma(\Delta\nu')$, and are the adopted uncertainties for K2 GAP DR3. $\varsigma(\nu'_{\max})$ and $\varsigma(\Delta\nu')$ are conservative estimates of statistical uncertainties based on the reported pipeline statistical uncertainties. $\langle\Delta\nu'\rangle$ is adjusted using theoretically motivated correction factors, X_{Sharma} (Sharma et al. 2016), for use in asteroseismic scaling relations; an uncorrected version of $\langle\Delta\nu'\rangle$ for each star is provided, $\langle\Delta\nu\rangle = \langle\Delta\nu'\rangle/X_{\text{Sharma}}$, should the user wish to compute custom $\Delta\nu$ corrections. EPIC temperatures and metallicities are provided for this purpose, though these are relatively uncertain estimates of the true temperatures and metallicities (these uncertainties are also provided for convenience). The uncertainties in X_{Sharma} and $\sigma_{X_{\text{Sharma}}}$ are computed by perturbing the EPIC temperature and metallicities in a Monte Carlo procedure. Note that $\sigma_{X_{\text{Sharma}}}$ are not provided for EPIC ID 240289249 and EPIC ID 235193028, which have anomalously large EPIC temperature uncertainties. $\langle\nu'_{\max}\rangle$ values have an evolutionary state-dependent correction applied to align their asteroseismic radii with the Gaia radii, per Section 4. Pipeline-specific rescaled values, ν'_{\max} and $\Delta\nu'$, are only provided for targets for which at least two pipelines returned concordant results, and otherwise have a blank entry; the numbers of pipelines returning valid results for ν_{\max} or $\Delta\nu$ are denoted by $N_{\nu'_{\max}}$ and $N_{\Delta\nu'}$. A2Z $\Delta\nu'$ values are not provided, since A2Z $\Delta\nu$ values do not contribute to $\langle\Delta\nu'\rangle$. See the text for details.

(This table is available in its entirety in machine-readable form.)

Table 3
Solar Reference Value Scale Factors and Solar Reference Values

	A2Z	CAN	COR	SYD	BAM	BHM	K2 GAP DR3
$X_{\nu_{\max, \text{RGB}}, \text{APOKASC2}}$	1.00230 ± 0.00002	1.00820 ± 0.00002	0.99890 ± 0.00002	1.00060 ± 0.00002	
$X_{\nu_{\max, \text{RGB}}}$	0.9991 ± 0.0006	0.9953 ± 0.0003	1.0000 ± 0.0003	0.9990 ± 0.0007	1.0027 ± 0.0003	1.0034 ± 0.0003	
$\nu_{\max, \odot, \text{RGB}}$	$3095 \pm 2 \mu\text{Hz}$	$3125 \pm 1 \mu\text{Hz}$	$3050 \pm 1 \mu\text{Hz}$	$3087 \pm 2 \mu\text{Hz}$	$3102 \pm 1 \mu\text{Hz}$	$3060 \pm 1 \mu\text{Hz}$	$3076 \mu\text{Hz}$
$X_{\Delta\nu, \text{RGB}}, \text{APOKASC2}$	0.99930 ± 0.00001	1.00070 ± 0.00001	1.00510 ± 0.00001	0.99950 ± 0.00001	
$X_{\Delta\nu, \text{RGB}}$...	1.0042 ± 0.0002	1.0004 ± 0.0004	1.0001 ± 0.0012	0.9969 ± 0.0007	0.9978 ± 0.0005	
$\Delta\nu_{\odot, \text{RGB}}$...	$135.48 \pm 0.03 \mu\text{Hz}$	$134.97 \pm 0.05 \mu\text{Hz}$	$135.1 \pm 0.2 \mu\text{Hz}$	$134.42 \pm 0.10 \mu\text{Hz}$	$134.62 \pm 0.06 \mu\text{Hz}$	$135.146 \mu\text{Hz}$
$X_{\nu_{\max, \text{RC}}, \text{APOKASC2}}$	1.00350 ± 0.00003	1.00670 ± 0.00002	0.99090 ± 0.00002	1.00100 ± 0.00003	
$X_{\nu_{\max, \text{RC}}}$	0.9951 ± 0.0011	0.9935 ± 0.0006	0.9992 ± 0.0005	0.996 ± 0.001	1.0131 ± 0.0005	1.0024 ± 0.0006	
$\nu_{\max, \odot, \text{RC}}$	$3082 \pm 4 \mu\text{Hz}$	$3120 \pm 2 \mu\text{Hz}$	$3048 \pm 2 \mu\text{Hz}$	$3077 \pm 4 \mu\text{Hz}$	$3134 \pm 1 \mu\text{Hz}$	$3057 \pm 2 \mu\text{Hz}$	$3076 \mu\text{Hz}$
$X_{\Delta\nu, \text{RC}}, \text{APOKASC2}$	0.99650 ± 0.00003	1.01080 ± 0.00002	0.99600 ± 0.00001	1.00320 ± 0.00002	
$X_{\Delta\nu, \text{RC}}$...	1.0066 ± 0.0005	1.0010 ± 0.0005	0.999 ± 0.002	0.993 ± 0.002	0.9971 ± 0.0007	
$\Delta\nu_{\odot, \text{RC}}$...	$135.81 \pm 0.07 \mu\text{Hz}$	$135.06 \pm 0.07 \mu\text{Hz}$	$134.9 \pm 0.3 \mu\text{Hz}$	$133.9 \pm 0.3 \mu\text{Hz}$	$134.53 \pm 0.10 \mu\text{Hz}$	$135.146 \mu\text{Hz}$

Note. Solar reference value scale factors and solar reference values (see Section 3), compared to those computed for some of the same pipelines using a similar method with Kepler data (APOKASC-2; Pinsonneault et al. 2018). The adopted solar reference values for K2 GAP DR3 are listed in the last column. A2Z $\Delta\nu$ solar reference value scale factors and solar reference values are not provided, since A2Z $\Delta\nu$ values do not contribute to $\langle\Delta\nu'\rangle$; see Table 1 for the default A2Z $\Delta\nu_{\odot}$ value.

7

asteroseismic scales, due to the difference between the time baselines of Kepler and K2, which we discuss in Section 4.

We list in Table 2 the individual rescaled pipeline values $\nu'_{\max} = X_{\nu_{\max}} \nu_{\max}$ and $\Delta\nu' = X_{\Delta\nu} \Delta\nu$. As in K2 GAP DR2, we do not list ν'_{\max} or $\Delta\nu'$ if that pipeline value is sigma-clipped in the averaging procedure. We correct the pipeline-specific $\Delta\nu'$ as well as $\langle\Delta\nu'\rangle$ with theoretical $f_{\Delta\nu}$ from Sharma et al. (2016), using the EPIC temperatures and metallicities listed in Table 2. We use these rescaled ν'_{\max} and $\Delta\nu'$ values to compute rescaled $\kappa_{R'}$ and $\kappa_{M'}$ values for each star and each pipeline, using the solar reference values appropriate for each pipeline (see Table 1). Our recommended radius and mass coefficients, $\langle\kappa_{R'}\rangle$ and $\langle\kappa_{M'}\rangle$, are those computed using the average parameters $\langle\nu'_{\max}\rangle$ and $\langle\Delta\nu'\rangle$, and the APOKASC-2 solar reference values are modified so that our radii are on the Gaia parallactic scale (see Section 4): $\nu_{\max\odot, \text{RGB}} = 3081 \mu\text{Hz}$, $\nu_{\max\odot, \text{RC}} = 3096 \mu\text{Hz}$, and $\Delta\nu_{\odot, \text{RGB/RC}} = 135.146 \mu\text{Hz}$ (Pinsonneault et al. 2018). The pipeline-specific and average radius and mass coefficients are provided in Table 4, with their uncertainties being calculated according to standard propagation of uncertainty.³⁰

In K2 GAP DR2, we established that the uncertainties resulting from our averaging process follow χ^2 statistics, and can be described to a good approximation by fractional uncertainties that are mostly a function of evolutionary state. In Table 5 we report median fractional uncertainties in $\langle\nu'_{\max}\rangle$, $\langle\Delta\nu'\rangle$, $\langle\kappa_{R'}\rangle$, and $\langle\kappa_{M'}\rangle$ for both RGB stars and RC stars, which may be considered typical of the uncertainties in our sample. We also include typical fractional uncertainties in these parameters from K2 GAP DR2, APOKASC-2 (Pinsonneault et al. 2018), and another independent analysis of the Kepler data (Yu et al. 2018). The typical $\Delta\nu$ uncertainty for K2 GAP DR3 is somewhat larger than it was for K2 GAP DR2, due to the previously mentioned difference in how the sigma clipping is performed in the averaging procedure used for the two data releases. The resulting precisions in RGB masses, which are determinative in asteroseismic age precisions, are about a factor of two larger than those of Kepler, corresponding to uncertainties of about 20%–30% in age.

We provide all of the results returned by every pipeline in Table 6. Included in this table are machine-learning evolutionary states based on $\langle\Delta\nu'\rangle$ and $\langle\nu'_{\max}\rangle$, as well as evolutionary states based on individual pipeline values, which are taken to be $\Delta\nu'$ and ν'_{\max} .³¹ We also include the EPIC IDs for stars that had no measured asteroseismic parameters from any pipeline, but that were targeted as part of K2 GAP, so that users may investigate asteroseismic selection functions as needed; we quantify K2 GAP DR3 completeness as a function of mass and radius in Section 4.1. The K2 GAP DR3 sample that we refer to in what follows is a subset of the totality of the targeted stars, and consists only of the stars with a valid $\langle\nu'_{\max}\rangle$. There are 19,417 such stars, 18,821 of which also have a valid $\langle\Delta\nu'\rangle$ and therefore $\langle\kappa_{R'}\rangle$ and $\langle\kappa_{M'}\rangle$. Stars with both $\langle\nu'_{\max}\rangle$ and $\langle\Delta\nu'\rangle$ are assigned an evolutionary state, resulting in 12,978 RGB stars and 5843 RC stars. The numbers of stars

³⁰ Since A2Z $\Delta\nu$ values do not contribute to $\langle\Delta\nu'\rangle$, no $\Delta\nu_{\text{A2Z}}$ values are populated in Table 2, and the $\kappa_{R, \text{A2Z}}$ and $\kappa_{M, \text{A2Z}}$ values in Table 4 are calculated using the raw $\Delta\nu$ and rescaled ν'_{\max} values.

³¹ The A2Z evolutionary states are based on raw $\Delta\nu$ and rescaled ν'_{\max} . Also, for the small number of cases for which there were multiple observations of the same star across different campaigns, we adopted the evolutionary state from the campaign with the smallest evolutionary state uncertainty according to the machine-learning approach.

with asteroseismic detections broken down by campaign and pipeline are listed in Table 7. The Kiel diagram for the K2 GAP DR3 sample is shown in Figure 2, and its distribution on the sky is shown in Figure 1; the sample is also shown in Galactocentric coordinates in Figure 3.

4. Validation of Asteroseismic Values in K2 GAP DR3

4.1. Injection Tests

In the previous section, we detailed the dependence of asteroseismic results across pipelines. However, there are likely additional systematics due to the length of the K2 light curves compared to, e.g., Kepler light curves. Indeed, Hekker et al. (2012) revealed nonnegligible variations in the completeness, precision, and accuracy of red giant asteroseismic parameters due to the length of the time series (i.e., the time baseline). In order to test the completeness, precision, and accuracy of the different asteroseismic modeling pipelines for K2-like data, we generated synthetic data for which we knew the “true” ν_{\max} and $\Delta\nu$ from Kepler, and performed blind injection recovery tests.

We first created a grid of magnitude– ν_{\max} space from the distribution of Kepler stars using APOKASC-2 (Pinsonneault et al. 2018), the faint giant sample of Mathur et al. (2016), and the M-giant sample of Stello et al. (2014) in order to select Kepler stars evenly across this parameter space. From each bin, where possible, we generated K2-like light curves based on 80 day segments of Kepler light curves via two methods. First, we attempted to select from each bin three Kepler stars with at least five quarters of data each, from which we created 15 synthetic K2 light curves (selecting five different 80 day sections from three stars). Second, we attempted to generate 15 synthetic K2 light curves from 15 different Kepler stars using a single 80 day section of each of their light curves. In practice, however, not all bins had enough stars to create 30 synthetic K2 light curves via these two methods. Each of the synthetic K2 light curves was created using KASOC v1 Q1–Q14 light curves (Handberg & Lund 2014), linearly interpolating the Kepler flux onto the cadence of a star in K2 C3 in order to mimic the spectral window of actual C3 data and the frequency resolution of K2. We then increased the white noise level for each of the synthetic K2 light curves according to the following procedure. First, the white noise as a function of magnitude was computed for the entire grid of Kepler stars as well as the 10,291 non-GAP C3 targets with EVEREST long-cadence light curves. The white noise for each star was computed by taking the standard deviation of its light curve, filtered to remove variability slower than $\sim 150 \mu\text{Hz}$. For both of these samples, the 20th percentile of the white noise levels as a function of magnitude were fitted using third-degree polynomials. The white noise levels of each synthetic K2 light curve were increased by the ratio of the Kepler-to-K2 white noise if that ratio was less than unity at the Kepler star’s magnitude. In practice, this resulted in increasing the white noise levels of stars fainter than $Kp = 14$, by 10%, on average, and by no more than 20%.

We show in Figure 4(a) the S/N of the synthetic sample.³² We compute the S/N of the synthetic K2 data in a way that takes into account both the expected maximum mode amplitude and the granulation background level at ν_{\max} . To do so, we adopt the approach from Campante et al. (2016), by

³² Note that this is the S/N in power, not amplitude.

Table 4
Radius and Mass Coefficients

EPIC ID	$\langle \kappa_R \rangle$	$\sigma_{\langle \kappa_R \rangle}$	$\langle \kappa_M \rangle$	$\sigma_{\langle \kappa_M \rangle}$	$\kappa'_{R,A2Z}$	$\kappa'_{R,BAM}$	$\kappa'_{R,BHM}$	$\kappa'_{R,CAN}$	$\kappa'_{R,COR}$	$\kappa'_{R,SYD}$	$\sigma_{\kappa'_{R,A2Z}}$	$\sigma_{\kappa'_{R,BAM}}$	$\sigma_{\kappa'_{R,BHM}}$	$\sigma_{\kappa'_{R,CAN}}$	$\sigma_{\kappa'_{R,COR}}$	$\sigma_{\kappa'_{R,SYD}}$	$\kappa'_{M,A2Z}$	$\kappa'_{M,BAM}$	$\kappa'_{M,BHM}$	$\kappa'_{M,CAN}$	$\kappa'_{M,COR}$	$\kappa'_{M,SYD}$	$\sigma_{\kappa'_{M,A2Z}}$	$\sigma_{\kappa'_{M,BAM}}$	$\sigma_{\kappa'_{M,BHM}}$	$\sigma_{\kappa'_{M,CAN}}$	$\sigma_{\kappa'_{M,COR}}$	$\sigma_{\kappa'_{M,SYD}}$
210306475	13.406	1.086	1.694	0.331	12.815	15.798	12.502	13.912	1.012	1.901	1.298	1.573	1.515	2.438	1.362	1.847	0.359	0.605	0.324	0.484
210307958	10.541	0.818	1.060	0.186	...	12.100	...	10.323	10.927	0.836	...	0.594	0.562	1.439	...	1.019	1.100	0.213	...	0.142	0.134	...
210314854	10.232	0.480	1.073	0.133	10.158	10.690	10.625	10.757	10.313	11.131	0.926	0.493	1.029	0.599	0.479	1.870	0.968	1.181	1.141	1.157	1.094	1.277	0.233	0.125	0.236	0.180	0.123	0.552
210315825	9.194	0.193	1.661	0.075	10.034	9.539	9.312	9.576	9.338	9.763	0.818	0.292	0.609	0.335	0.332	0.541	1.938	1.748	1.686	1.779	1.671	1.845	0.412	0.140	0.235	0.151	0.143	0.296
210318976	11.201	0.368	1.015	0.084	13.643	11.089	11.847	...	1.087	0.798	0.623	...	1.492	0.950	1.120	...	0.347	0.175	0.139	...

Note. $\langle \kappa_R \rangle$ and $\langle \kappa_M \rangle$, and their uncertainties, are computed based on $\langle \Delta \nu' \rangle$ and $\langle \nu'_{\max} \rangle$, according to Equations (6) and (8). $\langle \kappa_R \rangle$ and $\langle \kappa_M \rangle$ values have an evolutionary state-dependent correction to align asteroseismic radii with the Gaia radii, per Section 4. The pipeline-specific radius and mass coefficients, κ'_R and κ'_M , are computed with the pipeline-specific asteroseismic parameters $\Delta \nu'$ and ν'_{\max} . See Section 3 for details.

(This table is available in its entirety in machine-readable form.)

6

Table 5
Median Fractional Uncertainties of Kepler and K2 Asteroseismic Quantities (in percent)

	APOKASC-2	RGB or Y18	RGB/AGB K2 GAP DR2	K2 GAP DR3	APOKASC-2	Y18	RC K2 GAP DR2	K2 GAP DR3
$\sigma_{\nu_{\max}}$	0.9	1.0	1.7	1.3	1.3	2.1	2.4	2.2
$\sigma_{\Delta\nu}$	0.4	0.3	1.7	1.1	1.1	1.1	2.3	1.8
σ_{r_R}	1.3	1.1	3.3	2.9	2.7	3.3	5.0	4.7
σ_{r_M}	3.4	3.1	7.7	6.7	6.2	8.4	10.5	11

Note. “APOKASC-2” indicates the median fractional uncertainties from the analysis of Pinsonneault et al. (2018), while “Y18” refers to the analysis of Yu et al. (2018). The K2 GAP DR2 uncertainties are taken from Table 7 of Zinn et al. (2020).

assuming three modes per order, ignoring observation integration time effects, and assuming a noise level according to the observed star-to-star white noise level at high frequencies in the spectra. For the maximum mode amplitude, we adopt the model $\mathcal{M}_{4,\beta}$ from Corsaro et al. (2013). The points are colored by the provenance of the Kepler data, in which there are potentially multiple synthetic stars per KIC ID because of the division of the Kepler light curves into 80 day sections. In total, there are 57 synthetic stars from the M-giant catalog (Stello et al. 2014); 891 synthetic stars from the faint giant catalog (Mathur et al. 2016); and 1691 synthetic stars from the APOKASC-2 catalog (Pinsonneault et al. 2018). The dashed lines demarcate the boundaries of the grid we used to draw the synthetic light curves in ν_{\max} space. We also show the distribution in magnitude space in Figure 4(b), with the vertical lines demarcating the magnitude bins used to populate the synthetic sample.

The analysis of these synthetic K2 data via the pipelines proceeded blindly (i.e., the synthetic data were treated as real data), and the resulting asteroseismic parameters were processed using an iteration of the averaging procedure described in Section 3.2. The average results are denoted in the following figures as “ALL,” and any pipeline-specific results for synthetic K2 data are only shown if they meet the same criteria as the real data (i.e., having at least two pipelines return results).

In Figure 5, we show the accuracy of the recovery for each of the asteroseismic pipelines, based on the ground truth Kepler asteroseismic values. For this exercise, each pipeline analyzed the Kepler light curves to generate ground truth labels. For the purposes of this plot and those that follow, uncertainties on the binned median are computed by inflating the standard uncertainty on the binned mean by a factor of $\sqrt{\frac{\pi}{2}}$ (Kenney & Keeping 1962).

We show the trends in the K2 asteroseismic values as functions of both ν_{\max} and $\Delta\nu$, which are evident at the percent level as functions of ν_{\max} and $\Delta\nu$. There are also biases when the trends are averaged over all of ν_{\max} and $\Delta\nu$, which can be seen by the fact that the trends for some pipelines in Figure 5 are systematically offset below the one-to-one line. This suggests that there are nonnegligible systematics in asteroseismic pipeline recovery that are a function of the baseline, which would result in too-small radii and masses compared to Kepler asteroseismology (see the below comparison between mass distributions in K2 and Kepler). The time baseline seems to have the smallest impact on $\Delta\nu$, since several pipelines report nearly identical $\Delta\nu$ with Kepler as with K2 data (though some pipelines show substantial disagreement). ν_{\max} , however,

suffers from significant biases relating to the time baseline: excursions of 2%–3% and zero-point biases of 1%–2% are observed. There are also indications that some pipelines may have S/N-dependent biases, which manifest as trends in fractional agreement between Kepler and synthetic K2 values as a function of S/N in Figure 6. Note that the S/N shown in this figure is not the same S/N that is shown in Figure 4(a): the S/N in Figure 6 represents the relative S/N at fixed ν_{\max} , and is computed by dividing out the median trend from Figure 4(a).

Although we will be calibrating our K2 data based on independent estimates of radius in Section 4.2, these biases are important to note, and are being investigated in the context of Transiting Exoplanet Survey Satellite (TESS; Ricker et al. 2014; Stello et al. 2021). It should also be noted that additional biases could be introduced in the asteroseismic analysis, based on the preparation of the pixel-level data and the details of processing the light curves into power spectra (e.g., choices of frequency filter). Based on internal consistency checks against K2SFF light curves (Vanderburg & Johnson 2014), such effects are smaller than the time baseline biases shown here (<1%).

As well as testing the ν_{\max} -, $\Delta\nu$ -, S/N-, and time baseline-dependent biases in the pipeline results, we can test the internal consistency of the uncertainties using the synthetic K2 data. Since we have results from precise Kepler data, we can compare these to the less precise, simulated K2 data for the same stars, and evaluate whether the pipeline results are internally consistent to within their reported uncertainties. To do so, the observed distribution of the fractional deviation between the K2 and Kepler measurements (“true” in Figure 7) is compared to the expected distribution (“reported” in Figure 7), created by drawing Gaussian random variables assuming the reported K2 uncertainty for each simulated K2 star. If the reported uncertainties should be self-consistent, then the two distributions would be identical. If the pipeline should tend to overestimate uncertainties, however, the “reported” distribution would be skewed toward higher uncertainties compared to the “true” distribution, and vice versa. The internal consistency is globally good for most pipelines. This plot also indicates the relative precision of the pipelines, with the dashed line indicating $\sigma_{\Delta\nu} = 0.01$ and $\sigma_{\nu_{\max}} = 0.03$, which are representative values for the internal uncertainties for the pipelines. For $\Delta\nu$, there is perhaps a tendency for the pipelines that provide results for fewer stars (and hence that are perhaps more strict in accepting which measurements are valid) to show smaller deviations between the “true” and “reported” values. By the same token, the more values that a pipeline accepts as

Table 6
Raw Asteroseismic ν_{\max} and $\Delta\nu$ Values, with Evolutionary States

ID	EPIC ID	Campaign	Priority	Evo. State	A2Z (EV)	BAM (EV)	BHM (EV)	CAN (EV)	COR (EV)	SYD (EV)	$\nu_{\max,A2Z}$	$\sigma_{\nu_{\max,A2Z}}$	$\Delta\nu_{A2Z}$	$\sigma_{\Delta\nu_{A2Z}}$	$\nu_{\max,BAM}$	$\sigma_{\nu_{\max,BAM}}$	$\Delta\nu_{BAM}$	$\sigma_{\Delta\nu_{BAM}}$	$\nu_{\max,BHM}$	$\sigma_{\nu_{\max,BHM}}$	$\Delta\nu_{BHM}$	$\sigma_{\Delta\nu_{BHM}}$	$\nu_{\max,CAN}$	$\sigma_{\nu_{\max,CAN}}$	$\Delta\nu_{CAN}$	$\sigma_{\Delta\nu_{CAN}}$	$\nu_{\max,COR}$	$\sigma_{\nu_{\max,COR}}$	$\Delta\nu_{COR}$	$\sigma_{\Delta\nu_{COR}}$	$\nu_{\max,SYD}$	$\sigma_{\nu_{\max,SYD}}$	$\Delta\nu_{SYD}$	$\sigma_{\Delta\nu_{SYD}}$
											μHz	μHz	μHz	μHz																				
210306475_4	210306475	4	903	RGB	RGB	RGB	RC	RC	28.550	2.25	3.620	0.010	30.135	0.808	3.277	0.197	26.900	1.4	3.470	0.160	27.670	1.27	29.322	1.742	3.450	0.170
210307958_4	210307958	4	2771	RGB	...	RC	...	RC	RGB	...	27.940	2.47	3.890	...	30.316	0.723	3.723	0.124	29.260	1.03	4.004	0.094	28.350	0.83	3.805	0.083	28.341	1.478
210314854_4	210314854	4	1141	RGB	RGB	RC	RGB	RGB	RC	RC	29.030	2.03	4.100	0.120	31.863	0.743	4.115	0.083	31.200	1.0	4.090	0.190	30.600	1.49	4.066	0.056	31.640	0.89	4.204	0.079	31.662	3.853	4.033	0.238
210315825_4	210315825	4	1651	RGB	RGB	RGB	RGB	RGB	RGB	RGB	59.580	3.63	5.910	0.160	59.253	1.379	5.899	0.060	60.000	1.3	6.010	0.190	59.390	1.28	5.960	0.084	58.960	1.26	5.975	0.087	59.482	3.086	5.873	0.058
210318976_4	210318976	4	988	RGB	RGB	RGB	RGB	...	24.800	1.88	3.270	0.040	25.080	0.841	21.700	1.1	3.080	0.100	23.660	1.22	3.482	0.090	24.540	0.73	3.402	0.076	24.138	2.070

Note. The “raw” asteroseismic parameters returned by a given pipeline, along with their uncertainties, without the rescaling described in Section 3 being applied. Evolutionary states are also given for stars with both $\langle\nu'_{\max}\rangle$ and $\langle\Delta\nu'\rangle$ values (EV), as well for individual pipeline values (A2Z EV, BAM EV, etc.); see the text for details. If classified, a star’s evolutionary state is assigned as “RGB,” “RGB/AGB,” or “RC.” “Priority” refers to the K2 GAP target priority for a given K2 campaign, which is discussed in Section 2 (a smaller numerical value corresponds to a higher priority); serendipitous targets do not have a populated priority entry. “ID” is a unique combination of the EPIC ID and the campaign from which the measurements come (some stars were observed during multiple campaigns).

(This table is available in its entirety in machine-readable form.)

Table 7

Numbers of Stars with Raw Asteroseismic Values (ν_{\max} , $\Delta\nu$), Rescaled Asteroseismic Values (ν'_{\max} , $\Delta\nu'$), and Radius and Mass Coefficients (κ_R' , κ_M'), as a Function of Pipeline and Campaign

		ν_{\max}	ν'_{\max}	$\Delta\nu$	$\Delta\nu'$	κ_R'	κ_M'
C1	A2Z	672	541	672	0	541	541
C2	A2Z	2326	993	1932	0	833	833
C3	A2Z	1418	834	1042	0	636	636
C4	A2Z	1966	1272	1536	0	1116	1116
C5	A2Z	3088	2088	2398	0	1761	1761
C6	A2Z	1086	1311	1086	0	1215	1215
C7	A2Z	993	835	293	0	224	224
C8	A2Z	1254	718	959	0	581	581
C10	A2Z	1660	832	1213	0	629	629
C11	A2Z	1359	670	1058	0	540	540
C12	A2Z	1717	866	1280	0	678	678
C13	A2Z	2393	1578	1924	0	1304	1304
C14	A2Z	1571	799	1138	0	621	621
C15	A2Z	3777	2598	2906	0	2055	2055
C16	A2Z	2685	1621	2025	0	1388	1388
C17	A2Z	1913	1173	1458	0	1016	1016
C18	A2Z	423	230	323	0	221	221
Total	A2Z	30301	17291	23243	0	13827	13827
C1	BAM	948	698	757	457	457	457
C2	BAM	2591	1030	361	264	264	264
C3	BAM	1288	791	493	434	434	434
C4	BAM	2478	1282	844	751	751	751
C5	BAM	3001	2066	1158	1242	1242	1242
C6	BAM	2529	1626	955	1005	1005	1005
C7	BAM	2315	1202	677	587	587	587
C8	BAM	1107	719	426	385	385	385
C10	BAM	1568	852	428	348	348	348
C11	BAM	1339	647	275	229	229	229
C12	BAM	1603	878	471	419	419	419
C13	BAM	2262	1547	817	734	734	734
C14	BAM	1304	810	479	433	433	433
C15	BAM	3526	2589	1367	1261	1261	1261
C16	BAM	2269	1645	2269	1400	1400	1400
C17	BAM	1713	1209	609	763	763	763
C18	BAM	408	227	108	149	149	149
Total	BAM	32249	18115	12494	9641	9641	9641
C1	BHM	1030	670	1030	592	592	592
C2	BHM	1818	1009	1551	933	933	933

Table 7

(Continued)

		ν_{\max}	ν'_{\max}	$\Delta\nu$	$\Delta\nu'$	κ_R'	κ_M'
C3	BHM	1191	842	1086	775	775	775
C4	BHM	1984	1251	1529	1126	1126	1126
C5	BHM	2750	2120	2550	1933	1933	1933
C6	BHM	2275	1606	1702	1370	1370	1370
C7	BHM	1803	1186	1238	989	989	989
C8	BHM	1094	722	869	656	656	656
C10	BHM	1590	871	1081	723	723	723
C11	BHM	1012	612	807	546	546	546
C12	BHM	1416	867	1053	749	749	749
C13	BHM	2112	1548	1764	1403	1403	1403
C14	BHM	1261	817	1003	739	739	739
C15	BHM	3216	2532	2730	2299	2299	2299
C16	BHM	2198	1648	1731	1400	1400	1400
C17	BHM	1697	1226	1307	1069	1069	1069
C18	BHM	344	249	266	218	218	218
Total	BHM	28791	18049	23297	16014	16014	16014
C1	CAN	1105	778	582	482	482	482
C2	CAN	1609	948	616	503	503	503
C3	CAN	1116	816	494	433	433	433
C4	CAN	1897	1204	968	793	793	793
C5	CAN	2530	2030	1559	1458	1458	1458
C6	CAN	1956	1514	1455	1273	1273	1273
C7	CAN	1564	1083	1048	879	879	879
C8	CAN	935	713	785	606	606	606
C10	CAN	1234	840	1093	679	679	679
C11	CAN	1000	612	874	515	515	515
C12	CAN	1181	854	1104	753	753	753
C13	CAN	1975	1548	1851	1326	1326	1326
C14	CAN	958	755	854	677	677	677
C15	CAN	3032	2497	2817	2250	2250	2250
C16	CAN	1814	1581	1633	1336	1336	1336
C17	CAN	780	1039	733	884	884	884
C18	CAN	297	235	260	191	191	191
Total	CAN	24983	17386	18726	13650	13650	13650
C1	COR	777	681	777	610	610	610
C2	COR	1635	960	1635	930	930	930
C3	COR	1022	757	1022	699	699	699
C4	COR	1803	1233	1803	1177	1177	1177
C5	COR	2526	1953	2526	1774	1774	1774

Table 7
(Continued)

		ν_{\max}	ν'_{\max}	$\Delta\nu$	$\Delta\nu'$	$\kappa_{R'}$	$\kappa_{M'}$
C6	COR	1443	1404	1443	1286	1286	1286
C7	COR	1561	1162	1561	1127	1127	1127
C8	COR	955	681	955	617	617	617
C10	COR	1449	824	1449	737	737	737
C11	COR	1048	613	1048	570	570	570
C12	COR	1309	819	1309	740	740	740
C13	COR	1879	1470	1879	1389	1389	1389
C14	COR	1034	755	1034	699	699	699
C15	COR	2944	2432	2944	2342	2342	2342
C16	COR	1833	1490	1833	1323	1323	1323
C17	COR	1368	1080	1368	977	977	977
C18	COR	265	201	265	164	164	164
Total	COR	24851	17019	24851	15850	15850	15850
C1	SYD	558	490	472	418	418	418
C2	SYD	1290	684	486	397	397	397
C3	SYD	1066	752	668	588	588	588
C4	SYD	2151	1270	735	670	670	670
C5	SYD	2627	2001	1627	1515	1515	1515
C6	SYD	2232	1472	782	743	743	743
C7	SYD	1678	1088	505	481	481	481
C8	SYD	937	681	588	518	518	518
C10	SYD	1138	715	466	385	385	385
C11	SYD	1583	699	459	378	378	378
C12	SYD	1097	751	584	511	511	511
C13	SYD	2007	1519	1230	1103	1103	1103
C14	SYD	1079	768	672	586	586	586
C15	SYD	3128	2492	1990	1819	1819	1819
C16	SYD	1886	1598	1229	1184	1184	1184
C17	SYD	598	1091	325	629	629	629
C18	SYD	266	232	176	183	183	183
Total	SYD	25321	16688	12994	11080	11080	11080

being valid, the more results deviating strongly from the truth are reported.

The above exercise tests the internal consistency of the uncertainties reported by each pipeline, but, by comparing the reported uncertainties to the scatter in the pipeline values for each star, $\sigma_{\langle\nu'_{\max}\rangle}$ and $\sigma_{\langle\Delta\nu'\rangle}$ (as described in Section 3), we can better establish the accuracy of the pipeline uncertainties. Indeed, even if a pipeline consistently assigns uncertainties to ν_{\max} and $\Delta\nu$, these uncertainties do not necessarily correspond to the true uncertainties—i.e., including systematic uncertainties—in the physical parameters: each pipeline’s methodology

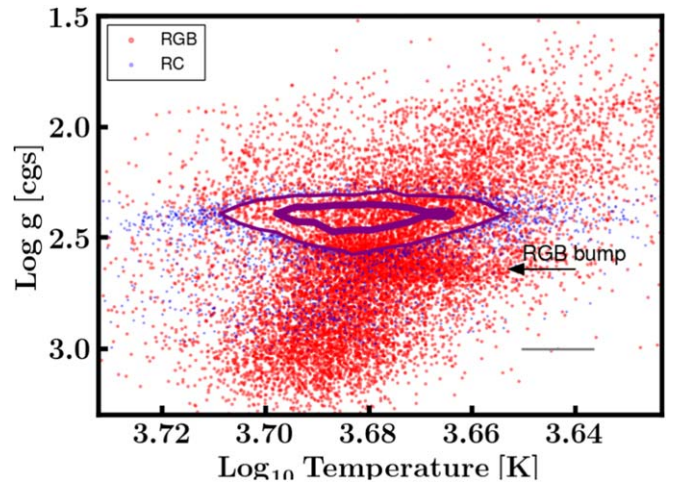


Figure 2. Kiel diagram of K2 GAP DR3, with stars colored red (blue) if they are classified as RGB stars (RC stars). The purple curves delineate the 38% and 68% contours for RC stars, to enhance clarity of the RGB bump (indicated by the arrow). The surface gravity is calculated using the EPIC temperature in combination with $\langle\nu'_{\max}\rangle$, according to Equation (1). The spread in temperature of the red clump is caused in part by its intrinsic width—set by population-level variations in metallicity, mass, and age—and also by the EPIC temperature uncertainty, which is indicated by the typical error bar indicated in the lower right.

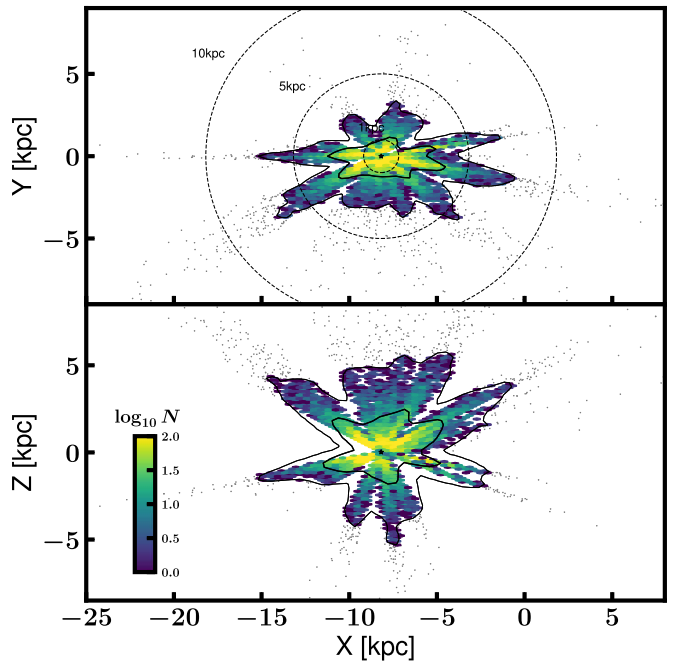


Figure 3. The distribution of K2 GAP DR3 stars (i.e., GAP targets with $\langle\nu'_{\max}\rangle$, as defined in Section 3.2), shown in Galactocentric coordinates. The Sun’s position of $(X, Y, Z) = (-8.18, 0, 0.021)$ kpc is marked as the black star, and is taken from a combination of the distance to Sgr A* (Gravity Collaboration et al. 2019; X) and the Gaia DR2 Galactic disk velocity distribution symmetry analysis from Bennett & Bovy (2019; Z). The inner (outer) contour represents the 68th (98th) percentile of the plotted stars. Within these contours, the logarithmic density of the stars is indicated according to the color bar. Dashed circles indicate distances of 1, 5, and 10 kpc.

is for its own system, and measures ν_{\max} and $\Delta\nu$ in slightly different ways. This can be seen to the extent that the scaling factors for each pipeline, $X_{\nu_{\max}}$ and $X_{\Delta\nu}$, differ from unity, indicating that the pipelines measure asteroseismic values on scales that differ by up to 1%. Even after correction to the mean scale, the top panels of Figures 8–11 show that there are

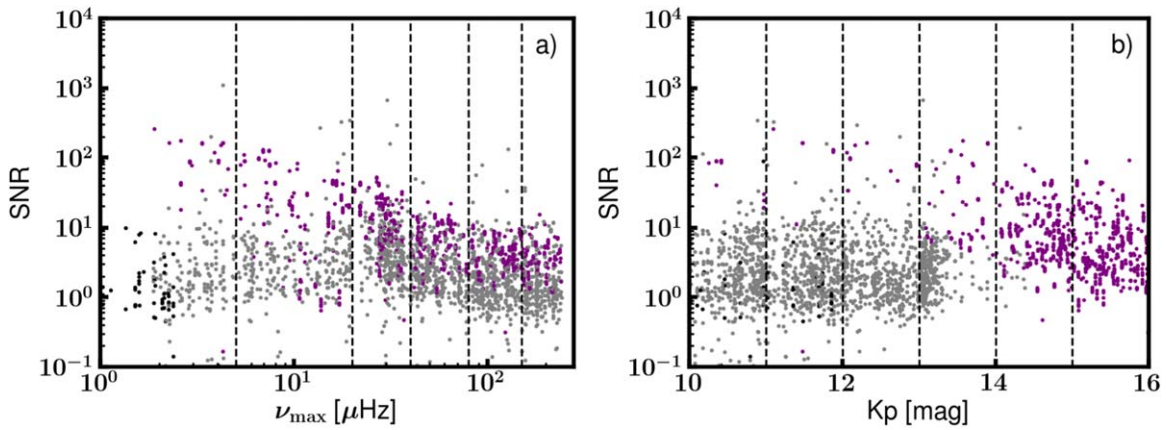


Figure 4. Distribution of the expected S/N for synthetic K2 stars as a function of the Kepler ν_{\max} (a) and Kepler magnitude (b). Synthetic stars are colored according to their provenance: Pinsonneault et al. (2018) (gray); Mathur et al. (2016) (purple); and Stello et al. (2014) (black). The synthetic population was drawn from a range of S/N and ν_{\max} in order to test the accuracy and precision of the asteroseismic pipelines in K2 GAP DR3.

residual fractional deviations between the rescaled pipeline values and the mean values across pipelines, ν'_{\max} and $\langle \nu'_{\max} \rangle$ as a function of ν_{\max} and $\Delta\nu$. By adopting the scatter in asteroseismic values across the pipelines for our uncertainties in K2 GAP DR3, we take into account the uncertainties resulting from these differences in pipeline methodologies. We show comparisons between the internal uncertainties for each pipeline and the K2 GAP DR3 uncertainties in the right panels of Figures 8–11. The region above (below) the dotted lines is the regime where the pipeline-reported uncertainties are larger (smaller) than the K2 GAP DR3 adopted uncertainties. As found in DR2, the pipelines often agree on $\Delta\nu$ and ν_{\max} better than would be expected from their internal uncertainties.

The uncertainties $\sigma_{\langle \nu'_{\max} \rangle}$ and $\sigma_{\langle \Delta\nu' \rangle}$ do not explicitly take into account the reported measurement/statistical uncertainties of the pipelines, but, by virtue of $\sigma_{\langle \nu'_{\max} \rangle}$ and $\sigma_{\langle \Delta\nu' \rangle}$ being defined based on the pipeline-to-pipeline scatter, they capture both systematic uncertainties in the pipeline methods and statistical measurement uncertainties: large bias in the pipeline results would tend to increase the pipeline-to-pipeline scatter, as would large measurement uncertainties. Even if we assume that the reported pipeline measurement uncertainties represent the true uncertainties, which is to varying degrees an inaccurate assumption (cf., Figure 7), it is not clear how the statistical uncertainties in the pipeline measurements should be combined in order to yield a purely statistical uncertainty in $\langle \nu'_{\max} \rangle$ and $\langle \Delta\nu' \rangle$, which are averages of the pipeline measurements. This is because the pipelines will have some degree of correlation between their measurements, owing to all of the pipelines analyzing the same power spectrum for a given star (i.e., there is only one realization of the data). In order to estimate a purely statistical uncertainty on $\langle \nu'_{\max} \rangle$ and $\langle \Delta\nu' \rangle$, we conservatively assume that all of the pipeline measurements are completely correlated, and compute the uncertainties on $\langle \nu'_{\max} \rangle$ and $\langle \Delta\nu' \rangle$, which we report in Table 2 as $\varsigma_{\langle \nu'_{\max} \rangle}$ and $\varsigma_{\langle \Delta\nu' \rangle}$. These latter uncertainties are larger than our adopted empirical uncertainties in this work, $\sigma_{\langle \nu'_{\max} \rangle}$ and $\sigma_{\langle \Delta\nu' \rangle}$, by factors of ~ 2.2 and ~ 1.5 , respectively. Assuming a correlation of 0.1 between all of the pipelines reduces the differences to ~ 1.2 and 0.95. Because the reported pipeline uncertainties are to varying degrees unreliable (Figure 7), and because of the unknown correlations between different pipeline measurements, these uncertainties are not used in this analysis, but are rather provided as a conservative

indication of a purely statistical uncertainty compared to our adopted empirical uncertainties, $\sigma_{\langle \nu'_{\max} \rangle}$ and $\sigma_{\langle \Delta\nu' \rangle}$.

We next estimate the completeness of each pipeline’s results by comparing the number of recovered stars to the total number of synthetic stars. The completeness fraction, where 1.0 indicates a perfect recovery rate, is shown as a function of ν_{\max} , $\Delta\nu$, radius, and mass in Figures 12–15. The synthetic sample was created with a range of S/Ns, and with magnitude-dependent noise consistent with K2 data, but the distribution of the synthetic sample is not, in detail, representative of the K2 GAP DR3 sample. For this reason, the completeness curves plotted in Figures 12–15 are indicative but not determinative of the completeness of the respective parameters in K2 GAP DR3. Note also that the completeness is defined with respect to Kepler results, so this completeness is, strictly speaking, an estimate of the completeness of recovering the K2 data with respect to Kepler, and not necessarily an absolute completeness estimate, which must await a future analysis using Gaia as a reference (e.g., by following the Kepler observation completeness analysis from Wolniewicz et al. 2021).

We see that the completeness curves are peaked in the middle of the parameter space for ν_{\max} and $\Delta\nu$, with lower completeness at the high and low values of ν_{\max} and $\Delta\nu$. This is understood to be related to the frequency resolution: detection of both $\Delta\nu$ and ν_{\max} is limited on the lower end by the time baseline, and on the upper end by the sampling rate of the K2 observations. It is even more difficult to recover ν_{\max} and $\Delta\nu$ at low values because of another effect: there are fewer modes that are excited at low ν_{\max} , and they can be difficult to distinguish from noise, especially at the frequency resolution of K2. This latter effect is the reason why there is a marked decrease in completeness for $\nu_{\max} \lesssim 10 \mu\text{Hz}$. This incompleteness has been noted in previous data releases (Stello et al. 2017; Zinn et al. 2020), but we are able to robustly quantify it here for the first time: although it varies by pipeline, at least $\approx 20\%$ of stars with $\nu_{\max} \lesssim 10 \mu\text{Hz}$ are not detected.

The completeness fractions in radius and mass space are not one-to-one mappings from ν_{\max} and $\Delta\nu$, since, for a given surface gravity (ν_{\max}), there is a spread in mass ($\Delta\nu$). For this reason, we consider the radius and mass completeness curves separately from the ν_{\max} and $\Delta\nu$ cases. The completeness of radius suffers from a drop-off in recovery with increasing radius, due to incompleteness of ν_{\max} and $\Delta\nu$ at lower frequencies. Given the lack of a strong correlation between

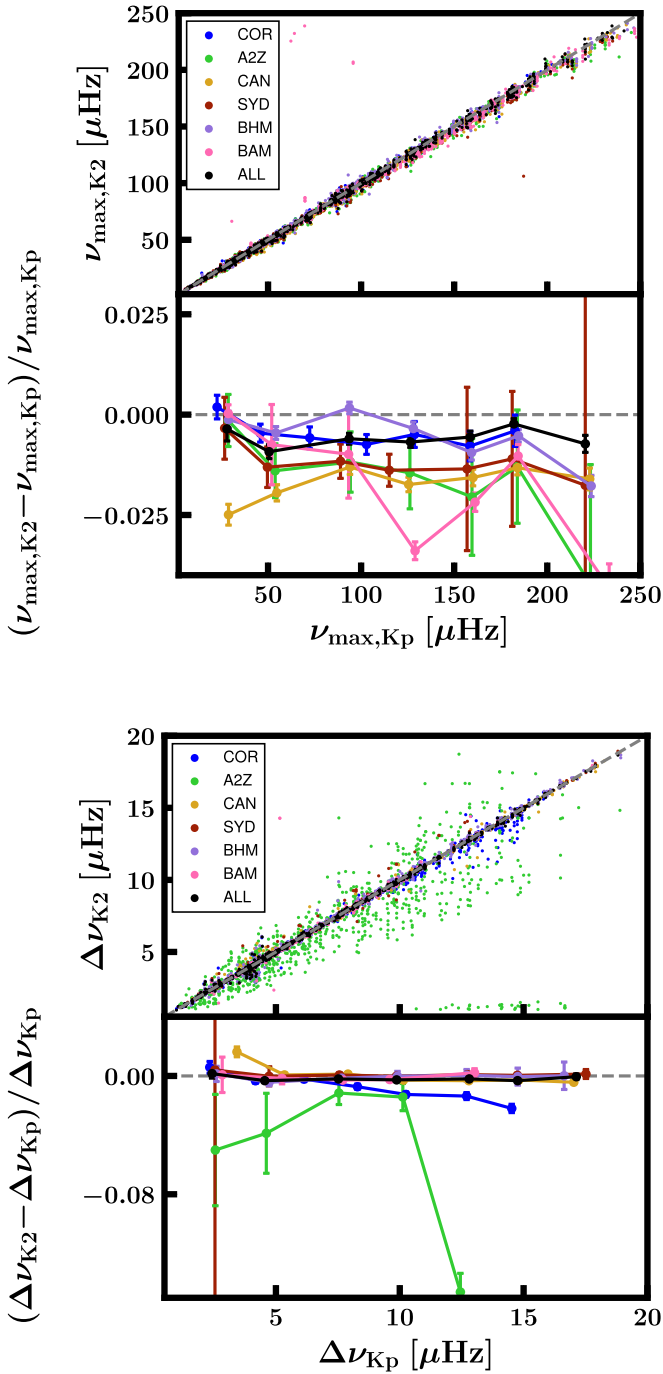


Figure 5. Binned medians and uncertainties on the median of the fractional difference between Kepler and synthetic K2 ν_{\max} (top) and $\Delta\nu$ (bottom) values for each pipeline contributing results to K2 GAP DR3, according to the legend. The deviations from the dashed line indicate that the pipeline returns K2 values that are on a different scale than the pipeline’s Kepler results (labeled as $\nu_{\max,K2}$ and $\nu_{\max,Kp}$ (top) and $\Delta\nu_{K2}$ and $\Delta\nu_{Kp}$ (bottom), respectively).

radius and age for the giant branch (since the majority of a red giant’s lifetime is spent on the main sequence, as opposed to climbing the giant branch), the drop-off in recovery with increasing radius does not require a selection function correction as a function of distance. The completeness curves are much less peaked in mass space. This is of particular interest for Galactic archeology applications of K2 GAP DR3: were completeness a strong function of mass, it

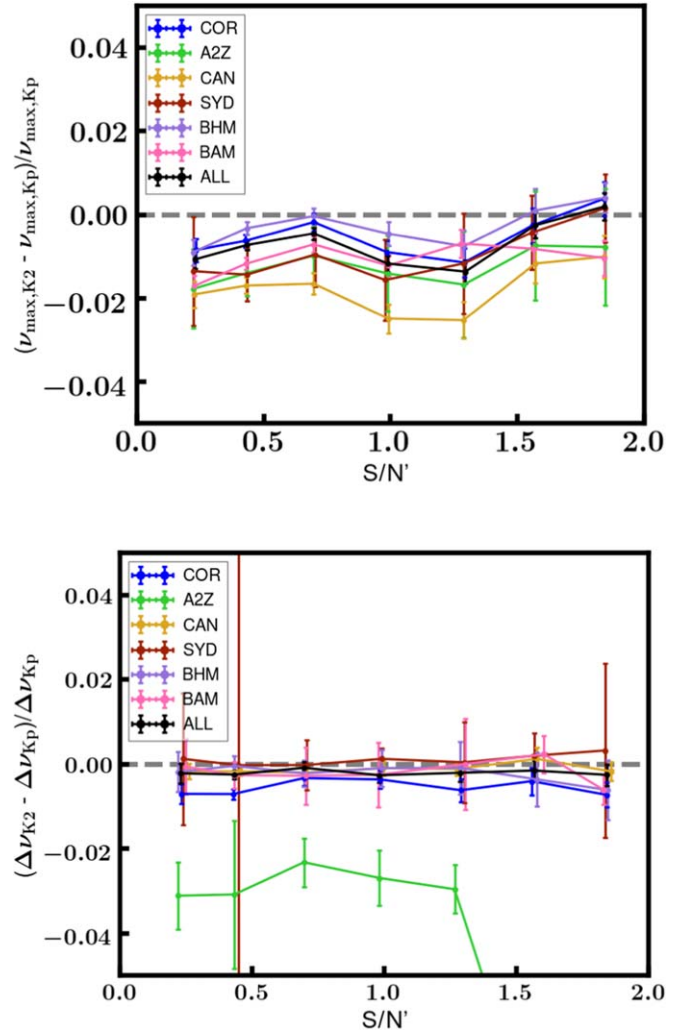


Figure 6. Fractional difference between Kepler and synthetic K2 values, for each pipeline according to the legend, as a function of the synthetic K2 S/N. The differences are shown as binned medians and uncertainties on the medians. Trends as a function of S/N would indicate that a pipeline’s asteroseismic values are noise-dependent.

would require special treatment in the selection function. There is a tendency for low-mass stars to be underrepresented in some pipelines, for $M \lesssim 1.2M_{\odot}$. This may be relevant for detailed studies, since this will map onto an underrepresentation of older stars. Regarding the completeness of the underlying K2 GAP sample itself, typically 97% of the proposed targets in any given campaign were observed, with the targets following simple color–magnitude cuts (S. Sharma et al. 2021, in preparation).

Figure 16(a) is indicative of the mass distribution for those stars in the K2 GAP DR3 sample with both $\langle\nu'_{\max}\rangle$ and $\langle\Delta\nu'\rangle$, where the ordinate is an asteroseismic proxy for mass proposed by Huber et al. (2010) that scales like $M^{0.25}$, given the asteroseismic scaling relations (Equations (3) and (4)). For reference, Figure 16(b) shows the Kepler sample from Yu et al. (2018). Comparing the Kepler and K2 samples, we find a good correspondence, with a couple of differences worth noting. First, the right edge of the clump is better defined in the Kepler data, by virtue of having greater precision and more high-mass secondary RC stars. The Kepler sample also extends to higher frequencies than K2 GAP DR3, presumably as a result of better

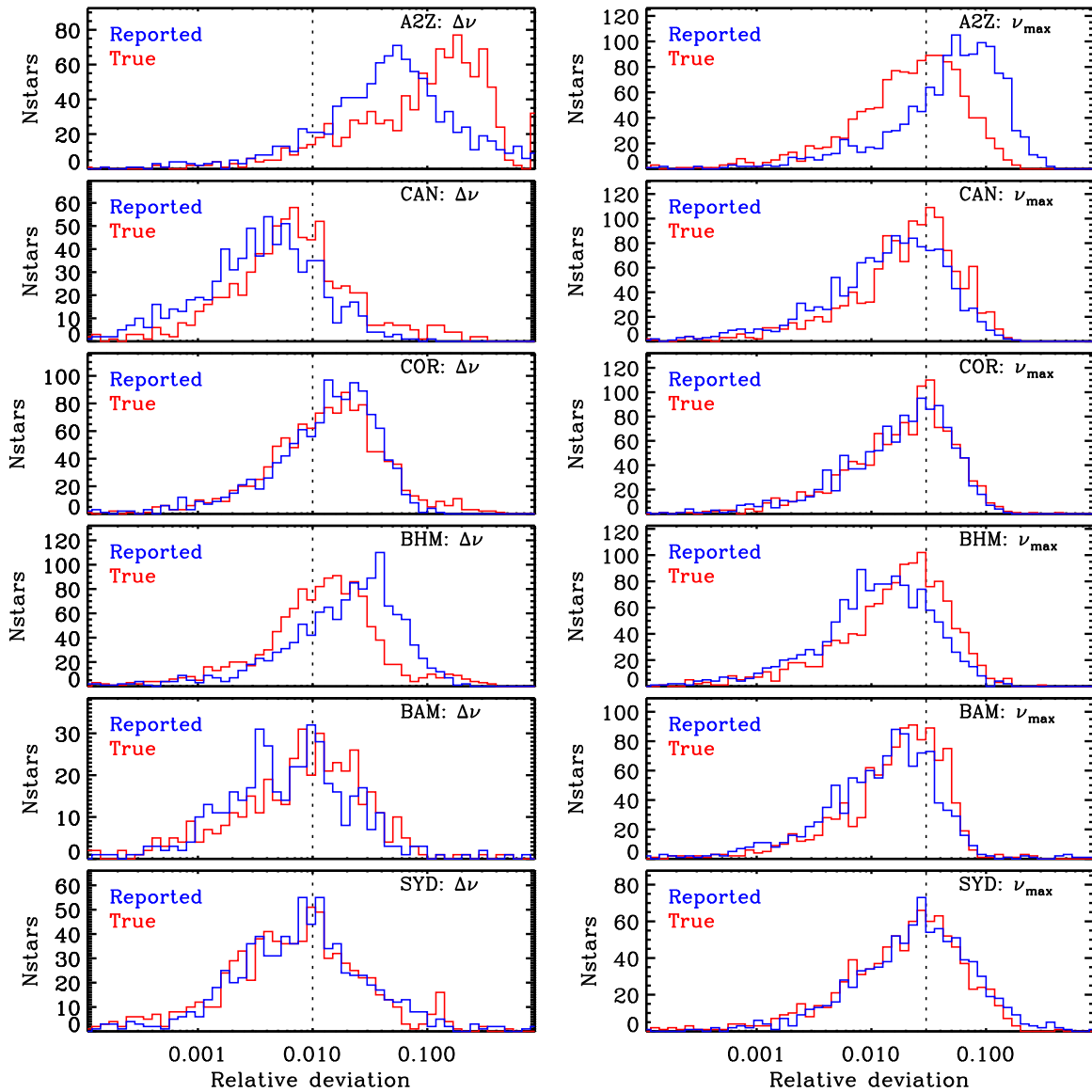


Figure 7. Reported pipeline fractional uncertainty distributions on K2 asteroseismic values (“reported”) and the inferred fractional uncertainty distributions by comparing the Kepler and K2 values (“true”). The dashed lines are shown for reference, and correspond to fractional uncertainties of 1% for $\Delta\nu$ and 3% for ν_{\max} .

noise properties in Kepler compared to K2. However, K2 has double the fraction of low-frequency ($<20 \mu\text{Hz}$) oscillators than Kepler, in spite of the tendency to not recover stars in this frequency regime with K2-like time baselines (Figure 12). Note that the overall shift in mass between the Yu et al. (2018) and K2 GAP DR3 samples is consistent with the time baseline systematics in ν_{\max} (Figure 5), such that the SYD Kepler ν_{\max} values would be expected to be larger by $\sim 1\%$ than the K2 ν_{\max} values.

As with Figure 16(a), Figure 17 shows the K2 GAP DR3 stars in the mass proxy versus ν_{\max} space, but for each pipeline, and separately for raw pipeline results (ν_{\max} , $\Delta\nu$; left panels) and rescaled pipeline values (ν'_{\max} , $\Delta\nu'$; right panels). The structures of the distributions in this space are generally similar across pipelines, though there are differences in detail. For instance, we see that there are some pipeline-dependent differences in the recovery of low-mass RC stars and the recovery of low-frequency stars. There are also differences between the raw and rescaled values, the most salient of which are that (1) raw values have more scatter in the ordinate (due to

the requirement for more than one pipeline to return results in order to define the rescaled values, which tends to favor stars with more precise asteroseismic values); and (2) there tend to be fewer low-frequency and high-frequency rescaled values (a selection effect of it being less likely for multiple pipelines to return values for stars affected by K2’s white noise and time baseline). The diagonal ridge on the left side of the RC distribution is due to the requirement that stars with $\Delta\nu < 3.2$ be assigned an RGB evolutionary state (see Section 3.2). However, we see that this choice does not cut out true RC stars, which are found in the locus where the density of the blue points saturates.

4.2. Asteroseismic Calibration with Gaia

In Section 3, we indicated that it is important to use appropriate solar reference values in accordance with the asteroseismic pipeline that is being used. The K2 GAP DR3 values are averages across pipelines, so the question arises as to what solar reference value scale is appropriate. One proposal

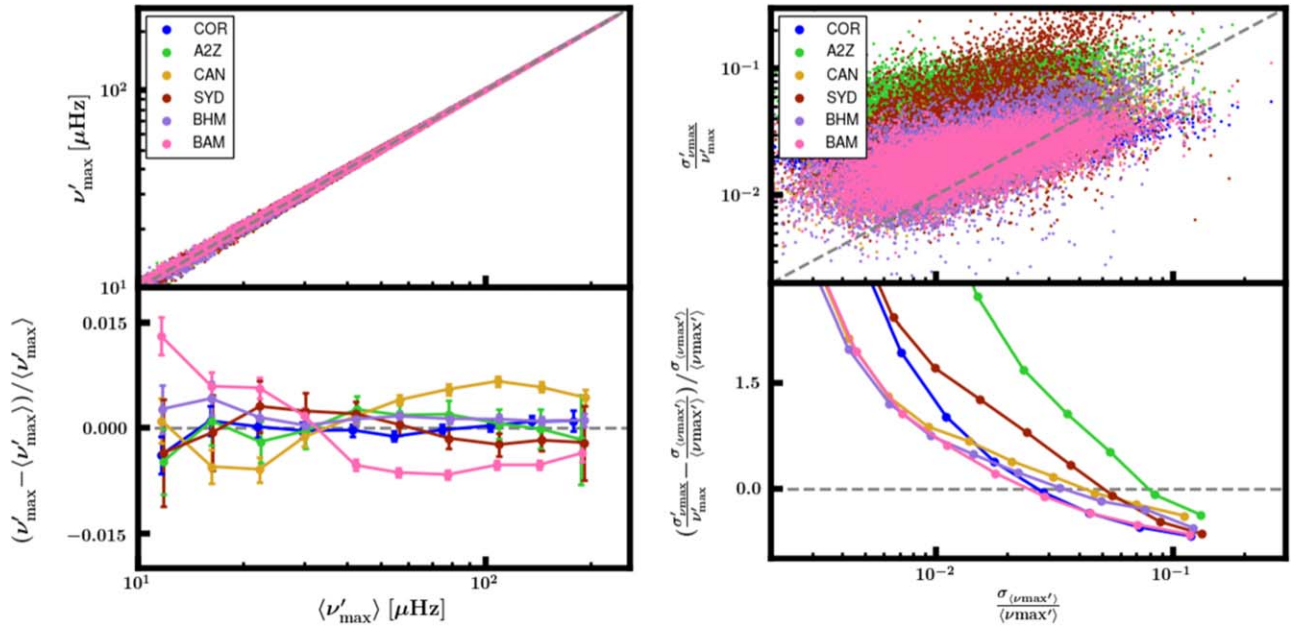


Figure 8. Left: comparison of RGB ν_{\max} between pipelines, showing the rescaled ν'_{\max} from each pipeline vs. the mean $\langle \nu'_{\max} \rangle$ across pipelines in the top panel, and the fractional difference between $\langle \nu'_{\max} \rangle$ and ν'_{\max} in the bottom panel, with error bars showing the binned errors on the median fractional difference, assuming the uncertainty on $\langle \nu'_{\max} \rangle$ to be the standard deviation of the rescaled pipeline ν'_{\max} values, $\sigma(\nu'_{\max})$. Right: the fractional scatter across ν'_{\max} for a given star with multiple pipeline values is plotted against the reported fractional uncertainty on ν'_{\max} for each pipeline. The fractional difference between the two fractional uncertainties is shown in the bottom panel.

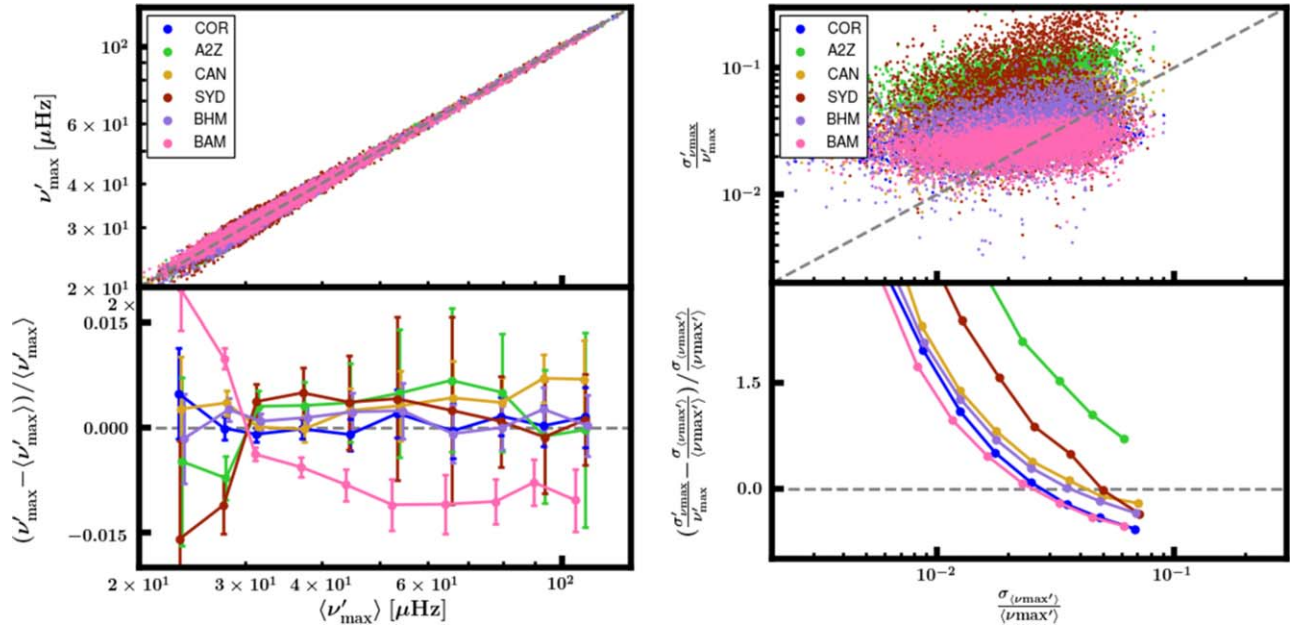


Figure 9. Same as Figure 8, but for RC stars.

would be to adopt the solar reference values from APOKASC-2 (Pinsonneault et al. 2018), $\nu_{\max,\odot} = 3076 \mu\text{Hz}$ and $\Delta\nu_{\odot} = 135.146 \mu\text{Hz}$, given that APOKASC-2 values are also averages across pipelines. Although we follow a very similar methodology of placing the pipeline values on a common scale, it differs in some regards (e.g., sigma clipping and not weighting pipeline values by their uncertainties during the averaging process). We include results from BAM as well, which was not a pipeline that was considered in Pinsonneault et al. (2018). For this reason, we cannot assume that $\langle \nu'_{\max} \rangle$

and $\langle \Delta\nu' \rangle$ are on the same scale as defined by Pinsonneault et al. (2018) just because we use the solar reference values from the cluster calibration procedure in Pinsonneault et al. (2018). It is also possible that the difference between Kepler versus K2 observation durations results in systematically different parameter measurements (see Section 4.1).

With this in mind, in what follows we calibrate the K2 GAP DR3 $\langle \nu'_{\max} \rangle$ values by using a nonunity, scalar $f_{\nu_{\max}}$ (Section 3); or, equivalently, by rescaling the APOKASC-2 $\nu_{\max,\odot}$ value. Our Gaia calibration sample is the subset of stars

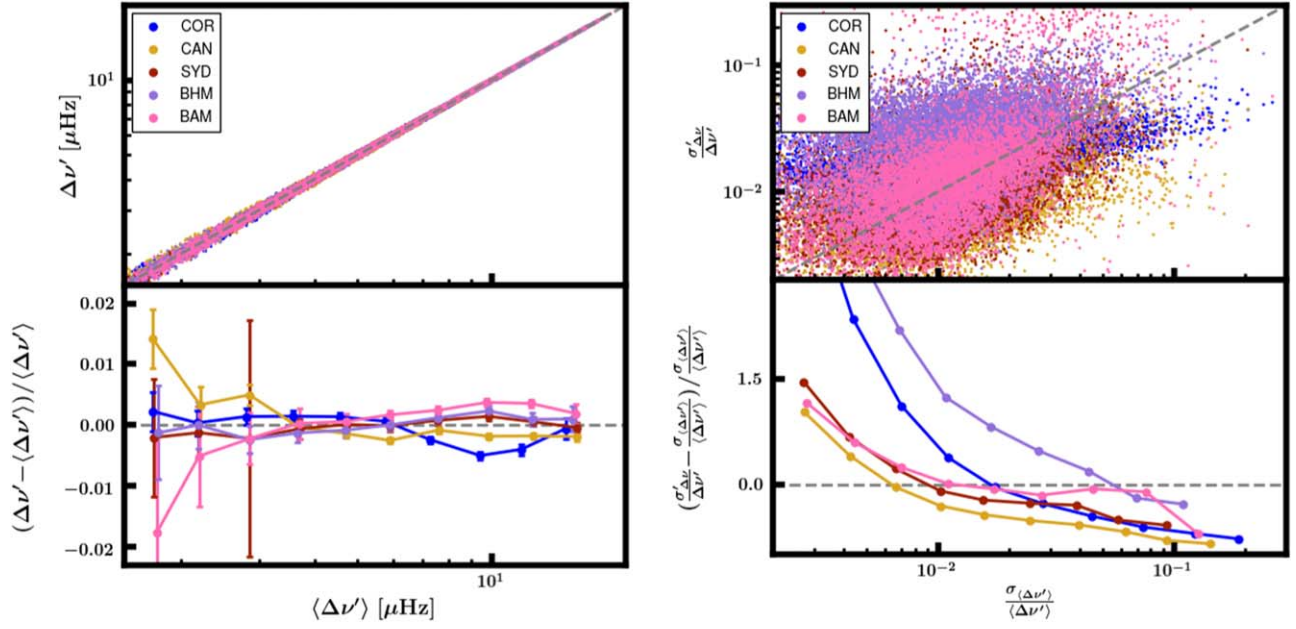
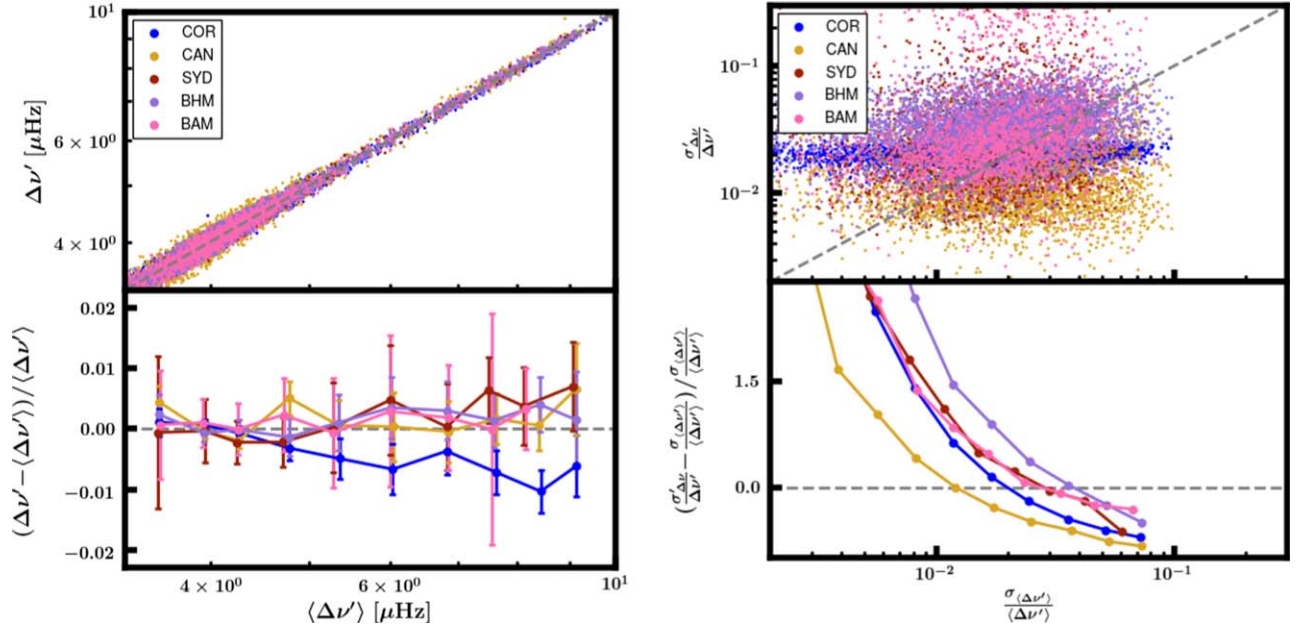

 Figure 10. Same as Figure 8, but for $\Delta\nu'$.


Figure 11. Same as Figure 10, but for RC stars.

in the K2 GAP DR3 sample with $\langle\nu'_{\max}\rangle$ and $\langle\Delta\nu'\rangle$ that have APOGEE DR16 (Ahumada et al. 2020) temperatures and metallicities, and Gaia parallaxes and proper motions from Gaia Data Release 2 (Gaia Collaboration et al. 2018; Lindegren et al. 2018).

With the known zero-point offset in Gaia parallax (e.g., Lindegren et al. 2018; Khan et al. 2019; Zinn et al. 2019a) in mind, we appeal to the methodology described in Schönrich et al. (2019), which infers distances in Gaia-based bulk stellar motions. This method can be sensitive to the selection function of the stellar population, and so we take care to model the selection function of the GAP targets according to Schönrich & Aumer (2017). The resulting parallax zero-points show a scatter of $\sim 10 \mu\text{as}$ across the campaigns, comparable to the

positional variation found by Chan & Bovy (2020) and Khan et al. (2019).

We perform the calibration using a subset of the Gaia–APOGEE–K2 overlap, knowing that there are certain known systematics that could bias the calibration. First, we limit the impact of parallax zero-points by only working with stars with raw Gaia parallaxes of $\pi > 0.4 \text{ mas}$, parallax uncertainties of less than 10%, and Gaia G -band magnitudes $< 13 \text{ mag}$, out of an abundance of caution, in light of the indications of parallax- and magnitude-dependent offsets (Schönrich et al. 2019; Zinn et al. 2019a). We also reject metal-poor stars ($[\text{Fe}/\text{H}] < -1$) from subsequent analysis, since there are also indications that asteroseismic scaling relation systematics could exist in the metal-poor regime (Zinn et al. 2019b; Epstein et al. 2014;

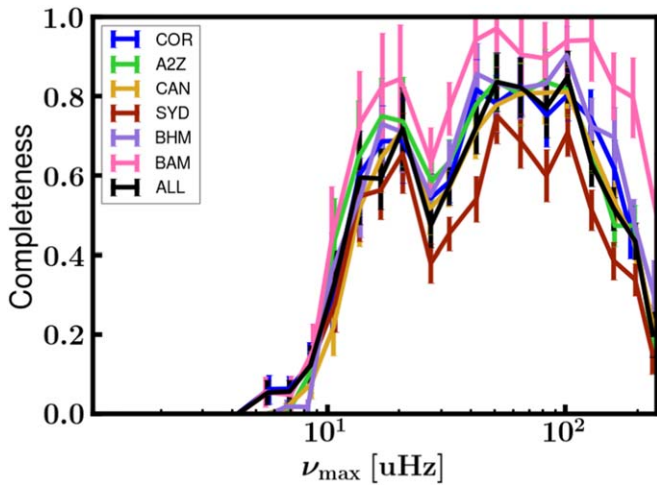


Figure 12. The recovery rate as a function of ν_{\max} for the pipelines contributing to K2 GAP DR3. A completeness of 1 would indicate that the pipelines recover all of the injected synthetic K2 stars generated from Kepler data, and would give confidence that the pipeline is recovering all of the detectable stars in the real K2 data.

though see also Kallinger et al. 2018). We further reject stars that are highly evolved ($R > 30R_{\odot}$), in order to avoid potential systematics in the asteroseismic scale in the luminous regime (Mosser et al. 2013; Stello et al. 2014; Kallinger et al. 2018; Zinn et al. 2019b). Finally, we reject from consideration 12 RGB and 2 RC stars that have asteroseismic and Gaia radius disagreements by more than 3σ , leaving 841 RGB and 214 RC stars for calibration. Since this sample includes APOGEE spectroscopic abundances, we also modify the $f_{\Delta\nu}$ for our calibration sample, by adjusting the metallicity that goes into computing $f_{\Delta\nu}$ to account for nonsolar α abundances according to the Salaris et al. (1993) prescription.

The Gaia radii are computed following the procedure from Zinn et al. (2017), wherein a bolometric flux, Gaia parallax, and APOGEE effective temperature are combined using the Stefan–Boltzmann law. We use a K_s -band bolometric correction (González Hernández & Bonifacio 2009) to minimize extinction effects, and employ the three-dimensional dust map of Green et al. (2015), as implemented in `mw dust` (Bovy et al. 2016).³³

We see in Figure 18 similar trends as we saw in K2 GAP DR2 (Zinn et al. 2020): there is an overestimation of the asteroseismic radii compared to Gaia at and below $R \approx 8R_{\odot}$ among RGB stars.

The strong trend of radius agreement for the RC stars is of astrophysical interest, particularly given constraints on mass loss (e.g., Miglio et al. 2012; Kallinger et al. 2018) that rely on the accuracy of asteroseismic scaling relations for the RC stars. However, as we noted in Zinn et al. 2020, the trend seems to be mostly a function of $\Delta\nu$, and it may therefore be related to inadequacies in the red clump stellar structure models that underpin theoretical $f_{\Delta\nu}$ calculations (An et al. 2019). It is beyond the scope of the present work to further examine the cause of the discrepancy, but developments in terms of better understanding this behavior in the RC stars are in preparation.

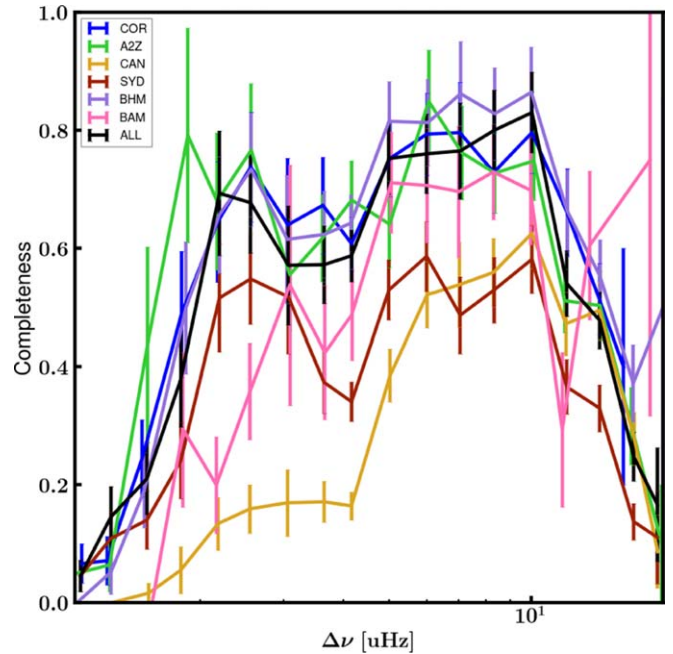


Figure 13. Same as Figure 12, but for $\Delta\nu$.

We calibrate our K2 GAP DR3 asteroseismic values to be on the Gaia parallactic scale by adopting the following:

$$f_{\nu_{\max}} \equiv \langle R_{\text{seis}} / R_{\text{Gaia}} \rangle = \frac{\sum R_{\text{seis}} / \sigma_R^2}{\sum 1 / \sigma_R^2},$$

where $\sigma_R = \frac{R_{\text{seis}}}{R_{\text{Gaia}}} \sqrt{\left(\frac{\sigma_{R,\text{Gaia}}}{R_{\text{Gaia}}}\right)^2 + \left(\frac{\sigma_{R,\text{seis}}}{R_{\text{seis}}}\right)^2}$. We do this separately for RGB and RC stars, finding $f_{\nu_{\max},\text{RGB}} = 1.017 \pm 0.001$ and $f_{\nu_{\max},\text{RC}} = 1.008 \pm 0.003$. This can be thought of as a rescaling of the solar reference value, $\nu_{\max,\odot}$; though, for convenience, we apply this correction directly to the $\langle \nu'_{\max} \rangle$, $\langle \kappa_R \rangle$, and $\langle \kappa_M \rangle$ values provided in Table 2, and thus when working with $\langle \nu'_{\max} \rangle$, the K2 GAP DR3 $\nu_{\max,\odot}$ value given in Table 1 should be used, which is the same as that from Pinsonneault et al. (2018). Even after accounting for this $f_{\nu_{\max}}$, the uncertainty in the $f_{\nu_{\max}}$ becomes a systematic uncertainty in the $\langle \kappa_R \rangle$ and $\langle \kappa_M \rangle$ scales, viz., 0.1% and 0.3% in $\langle \kappa_R \rangle$ and $\langle \kappa_M \rangle$ for RGB stars and 0.3% and 0.9% for RC stars. Note that it is possible that a scalar correction of $\langle \Delta\nu' \rangle$ is required as well. We therefore conservatively treat the uncertainty in $f_{\nu_{\max}}$ as an uncertainty in a scalar contribution to $f_{\Delta\nu}^2$, given that our calibration of the asteroseismic radius, which scales as $f_{\nu_{\max}}^{-1} f_{\Delta\nu}^2$ (Equation (6)), is formally a calibration of the quantity $f_{\nu_{\max}}^{-1} f_{\Delta\nu}^2$. This implies a systematic uncertainty in $\langle \Delta\nu' \rangle$ of 0.05% and 0.15% for RGB stars and RC stars, respectively. As discussed in Zinn et al. (2019b), there are additional systematics in the asteroseismology–Gaia radius comparison that could amount to about $\pm 2\%$ in $f_{\nu_{\max}}$, and that are due to intrinsic uncertainties in the bolometric correction scale, the temperature scale, and the spatial correlations in Gaia parallaxes.

On balance, the modest corrections required to bring the asteroseismic data onto the Gaia parallactic scale support previous findings that the asteroseismic scaling relations are

³³ <https://github.com/jobovy/mw dust>

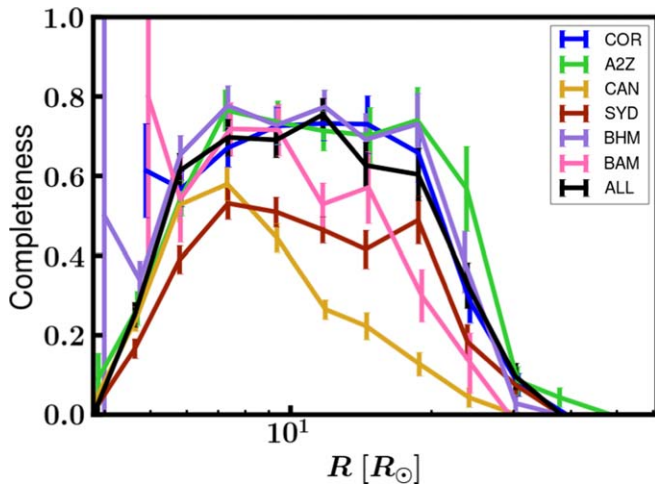


Figure 14. Same as Figure 12, but for radius.

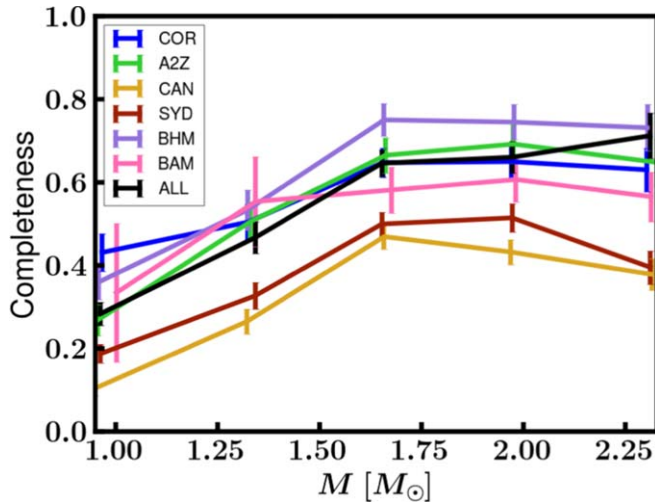


Figure 15. Same as Figure 12, but for mass.

accurate to within a few to several percent on the lower giant branch (e.g., Huber et al. 2012; Silva Aguirre et al. 2012; Hall et al. 2019; Khan et al. 2019; Zinn et al. 2019b). With the assurance that the K2 GAP DR3 asteroseismic masses are well calibrated, we now turn to applications of those data to age-abundance patterns.

5. Age-abundance Patterns in K2 GAP DR3

5.1. Notes on GALAH Abundances

Our examination of age-abundance patterns makes use of GALAH DR3 (Buder et al. 2021) abundances for stars targeted as part of the K2-HERMES (Wittenmyer et al. 2018) program. Although our asteroseismic calibration uses APOGEE temperatures and metallicities for deriving asteroseismic radii (Section 4.2), we note that calibration using GALAH spectroscopic parameters instead results in an equivalent $f_{\nu_{\max}}$ to within uncertainties. We opt to use GALAH abundances in what follows because (1) there are neutron-capture element lines in the optical unavailable to APOGEE’s infrared bandpass, and (2) GALAH abundances are corrected for non-LTE effects for the elements H, Li, C, O, Na, Mg, Al, Si, K, Ca, Mn, Fe, and Ba. On the latter point, non-LTE spectral analysis seems

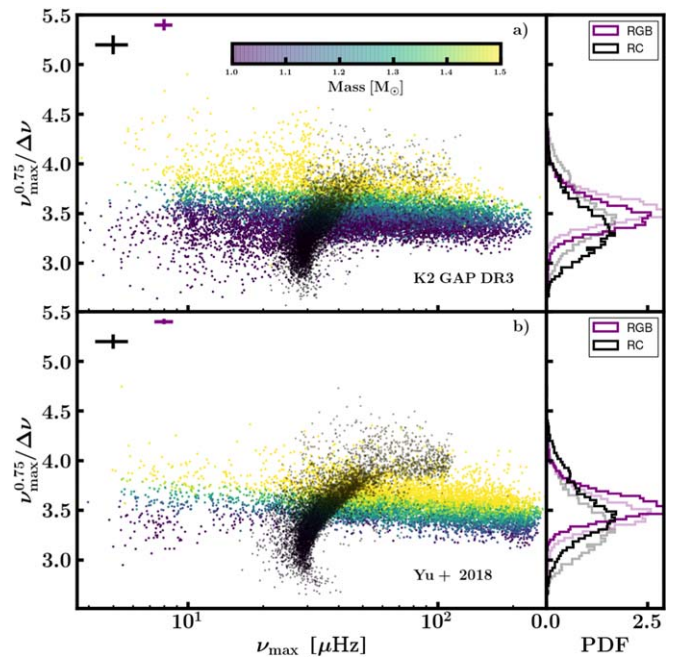


Figure 16. Asteroseismic mass diagrams for K2 GAP DR3 (a) and the Yu et al. (2018) Kepler sample (b), where the ordinate is a proxy for mass. Stars are colored by their asteroseismic mass, which is computed according to Equation (8), using EPIC temperatures. RC stars are indicated by black symbols. Stars are classified as first-ascendant red giants or not based on a machine-learning approach (see Section 3.2). Typical uncertainties for RGB stars and RC stars are indicated by the purple and black error bars. The probability density functions (PDFs) of the RGB and RC mass proxies are shown in the panels on the right, with the lighter curves in each panel showing the bold curves from the other panel, for comparison.

especially important for bringing into agreement dwarf and giant abundances at fixed metallicities within ~ 0.05 dex (Amarsi et al. 2020), though some systematics at the 0.1–0.2 dex level may remain for Al, Ba, and α elements, which are mentioned below.

We note that APOGEE DR16 temperatures and GALAH DR3 temperatures for RGB stars differ by ≈ 30 K, in the sense that APOGEE temperatures tend to be hotter. This difference is at the same level as the intrinsic uncertainty in the APOGEE temperature scale, which is set by the accuracy of the infrared flux method temperature scale for red giants (e.g., Alonso et al. 1999; González Hernández & Bonifacio 2009). The metallicity scales of the two systems differ by ≈ -0.05 dex, in the sense that APOGEE is more metal-rich. The combined effect of these small offsets means that the asteroseismic parameter calibration performed with APOGEE temperatures in Section 4 is consistent to within systematic uncertainties of $f_{\nu_{\max}}$, and thus the calibrated parameters are suitable for the following analysis using GALAH temperatures.

It should also be noted that scattering on background opacities was not included in the GALAH DR3 non-LTE calculations. Background scattering may affect giant abundances at the 0.01dex level for elements other than C, Mg, Ca, and Mn, which can have larger effects due to background scattering at lower metallicities (e.g., Hayek et al. 2011). Among metal-poor giants, Mg, Ca, and Mn may thus be underestimated by up to 0.05 dex for stars with $[\text{Fe}/\text{H}] < -2$ (Amarsi et al. 2020).

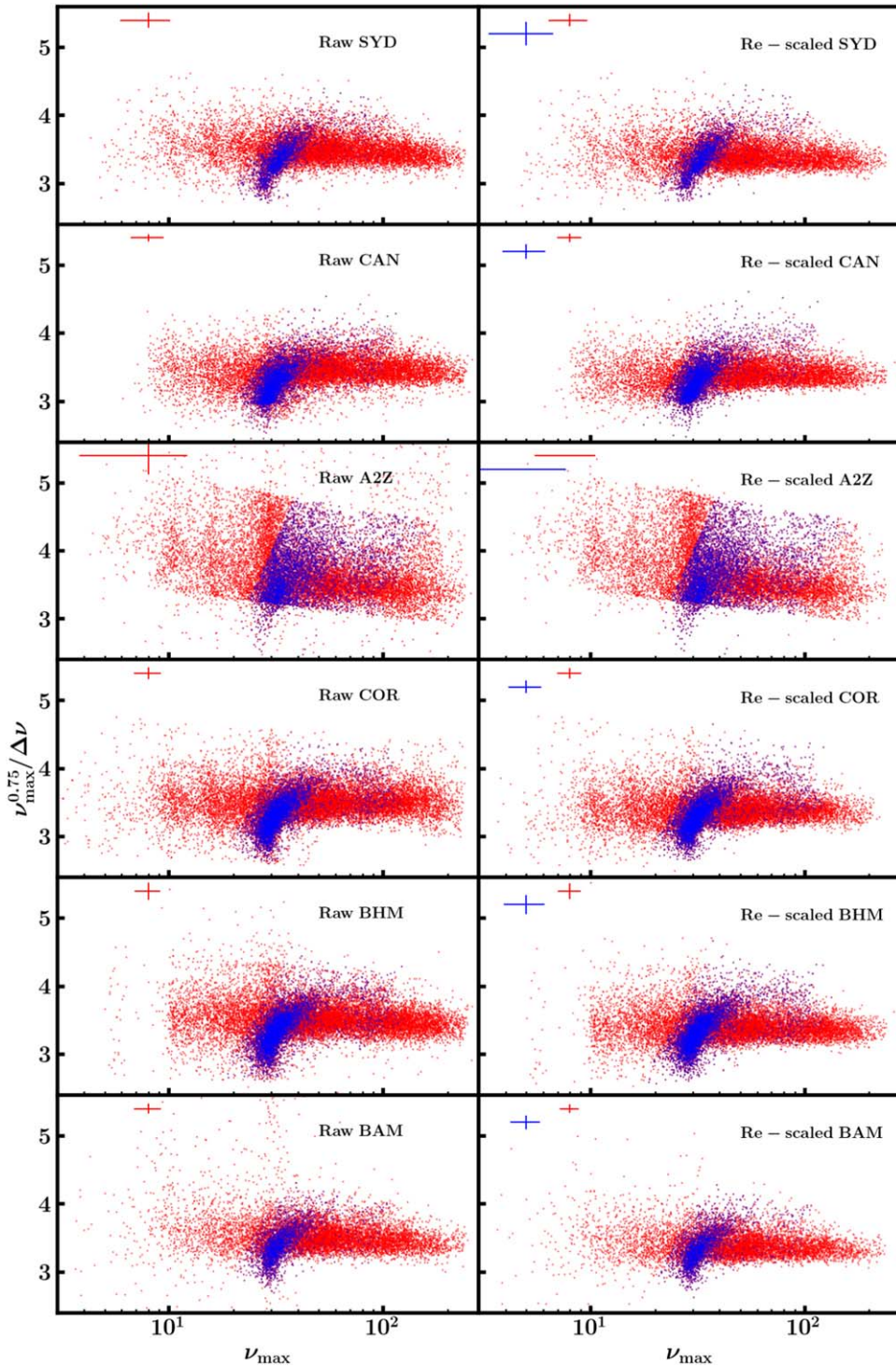


Figure 17. Asteroseismic mass diagrams for each pipeline, where the ordinate is a proxy for mass. RGB stars are shown as red points, and RC stars are shown as blue points. The left column shows the raw pipeline-specific values ($\Delta\nu$, ν_{\max}) and the right column shows the rescaled pipeline-specific values ($\Delta\nu'$, ν'_{\max}), which are only given for stars with results from at least two pipelines (see Section 3.2). Stars are classified as first-ascent red giants or not based on a machine-learning approach, using pipeline-specific asteroseismic values (see Section 3.2). Typical uncertainties for RGB and RC stars are indicated by the red and blue error bars.

5.2. Benchmark Galactic Chemical Evolution Model

We compare our age-abundance patterns to the fiducial abundance models of Kobayashi et al. (2020a, hereafter **K20**). The models use nucleosynthetic yields from CCSNe, SNe Ia, AGB stars, and neutron star mergers, which are discussed as relevant in the discussion that follows. The **K20** models assume a one-zone enrichment model, wherein mixing of the

interstellar medium is instantaneous, and there is pristine gas inflow. The infall rate and star formation efficiency are chosen to match the metallicity distribution function of the solar neighborhood. For the solar neighborhood model considered here, there is assumed to be no gas outflow. **K20** assume single-degenerate SNe Ia, where the total number of SNe is determined from the O/Fe slope. The fraction of main sequence+white dwarf to RGB+white dwarf progenitors is

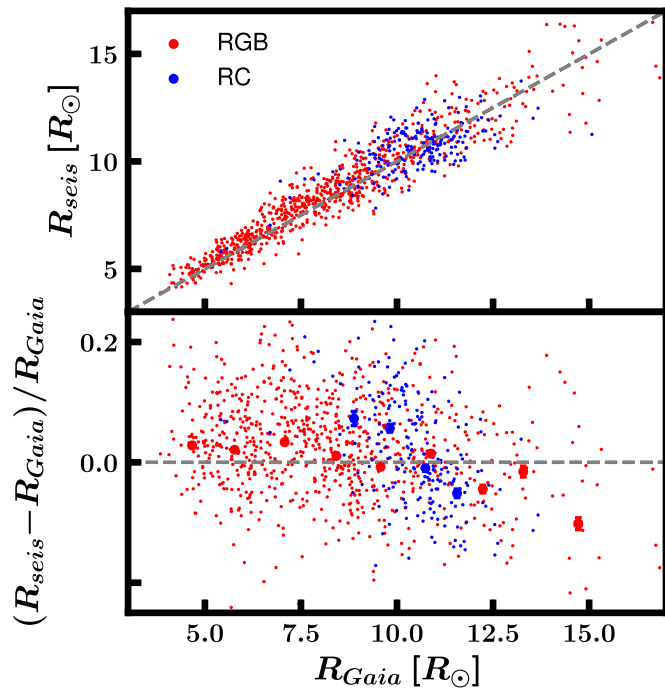


Figure 18. A comparison between Gaia radius and asteroseismic radius for the Gaia–APOGEE–K2 sample used for the calibration of K2 GAP DR3. The binned medians and uncertainties on the medians of the fractional difference between asteroseismic and Gaia radii are plotted as blue (red) error bars for RC (RGB) stars in the bottom panel, while the radii are plotted vs. each other in the top panel. Both panels have a gray dashed line to indicate perfect agreement between the two radii. We separately redefine $\nu_{\max, \odot}$ for the RGB stars and RC stars in K2 GAP DR3, such that their radii agree on average with Gaia radii (see Table 3).

fit to reproduce the observed Galactic metallicity distribution function—see, e.g., Figure A2 of Kobayashi et al. (2020b). We note that the $[\text{Fe}/\text{H}]$ at which SNe Ia begin to go off in the K20 models is not simply determined by the delay-time distribution of SNe Ia, but rather the metallicity dependence of Fe production in SNe Ia (Kobayashi et al. 1998). This is because the K20 models’ SNe Ia single-degenerate scenario assumes that white dwarfs surpass the Chandrasekhar mass limit via metallicity-dependent white dwarf winds that prevent common envelope production and encourage stable mass transfer (see Hachisu et al. 1996; Kobayashi et al. 1998; Kobayashi & Nomoto 2009).

The K20 models that we use are representative of the solar neighborhood, and so we restrict our analysis to K2 GAP DR3 stars with Galactocentric distances between 7 and 9 kpc.

Because the K20 models are calibrated to observations purely in abundance space, and not with reference to stellar age measurements, comparing the observed K2 GAP DR3 age-abundance patterns to the models provides an independent check on the success of the assumed global (star formation rate and infall rate) and local (nucleosynthetic yields) model choices. Of particular interest in what follows are the implications for the nucleosynthetic site of production and yields. For comparisons of the GALAH DR3 abundance ratios to the K20 models, we refer the reader to Amarsi et al. (2020).

5.3. Ages

We derive ages from K2 GAP DR3 asteroseismic masses computed according to Equation (4) with $\langle \kappa_M \rangle$ and GALAH DR3 temperatures. The age inference is performed in a

Bayesian framework using BSTEP (Sharma et al. 2018), a Bayesian stellar parameter estimator that may incorporate asteroseismic parameters, ν_{\max} and $\Delta\nu$, which essentially constrain the mass of the star and therefore its main sequence lifetime. Further details regarding the BSTEP ages used in this work are available in Sharma et al. (2021) (see also Buder et al. 2021). In what follows, we only use the stars that BSTEP classifies with high confidence as RGB, given uncertainties on RC ages due to mass loss (e.g., Casagrande et al. 2016).

5.4. $[\text{Mg}/\text{H}]$ versus $[\text{Fe}/\text{H}]$ Space

We begin by dividing our sample into high- and low- α samples, following the high–low boundary from Weinberg et al. (Weinberg et al. 2019; hereafter, W19):

$$\text{for } [\text{Fe}/\text{H}] < 0: [\text{Fe}/\text{Mg}] > 0.12 - 0.13[\text{Fe}/\text{H}], \quad (9)$$

$$\text{for } [\text{Fe}/\text{H}] > 0: [\text{Fe}/\text{Mg}] > 0.12. \quad (10)$$

The above division was initially used for stars with APOGEE abundances, but it has subsequently been used successfully to divide GALAH DR2 (Buder et al. 2018) abundances into high- and low- α populations by Griffith et al. (2019; hereafter, GJW19), who recently interpreted both APOGEE and GALAH DR2 abundance ratios in the context of Galactic chemical evolution. Following the example of GJW19, we also restrict analysis to those stars with effective temperatures between 4500 and 6200 K, which avoids blending in cool stars from molecular lines and highly broadened lines in fully radiative stars.

We believe there is some contamination from genuinely α -poor stars that, by virtue of their abundance uncertainties, scatter into the high- α selection (and vice versa). For this reason, we require each star’s 2D uncertainty ellipse to have more than 95% of its density on one side or the other of the high-/low- α division line. In order to construct the 2D uncertainty ellipse, we assume a uniform correlation between $[\text{Fe}/\text{H}]$ and $[\text{Mg}/\text{Fe}]$. The Pearson correlation coefficient between $[\text{Fe}/\text{H}]$ and $[\text{Mg}/\text{Fe}]$ is observed to be ~ -0.4 , though the precise value adopted does not significantly affect our results. We also require stars to have $[\text{Fe}/\text{H}] > -1$ at 95% confidence, since the metal-poor stellar population is likely populated by accretion (e.g., Belokurov et al. 2018; Haywood et al. 2018), rather than in situ formation, as the K20 models assume. The resulting division of the GALAH abundances is demonstrated in Figure 19, where each star is colored by its age. The high-/low- α division line is shown in black. The gray curve represents the raw K20 $[\text{Fe}/\text{H}]$ – $[\text{Mg}/\text{Fe}]$ trend, which has been shifted by a scalar offset in $[\text{Fe}/\text{H}]$ and a scalar offset in $[\text{Mg}/\text{Fe}]$ to reflect the same solar abundance scale used by GALAH DR3—see Table A2 of Buder et al. (2021).³⁴ The segmented blue curve represents the K20 $[\text{Fe}/\text{H}]$ – $[\text{Mg}/\text{Fe}]$ trend, rescaled by an additive offset in Mg such that the median predicted $[\text{Mg}/\text{Fe}]$ agrees with the median observed $[\text{Mg}/\text{Fe}]$. The band around the curve corresponds to a 1σ uncertainty in the Asplund et al. (2009) solar abundances, which are used in the K20 models for abundance normalization.³⁵

The sample consists of 396 high- α stars and 208 low- α stars, with typical uncertainties of 20%–30% in age.³⁶ The ages for

³⁴ Where possible, we adopt the “composite” abundance normalizations listed in Table A2 of Buder et al. (2021) and, otherwise, the average of a given element’s line-by-line normalizations.

³⁵ The exception is O, whose solar abundance is taken to be $A_{\odot}(\text{O}) = 8.76 \pm 0.02$ (Steffen et al. (2015)).

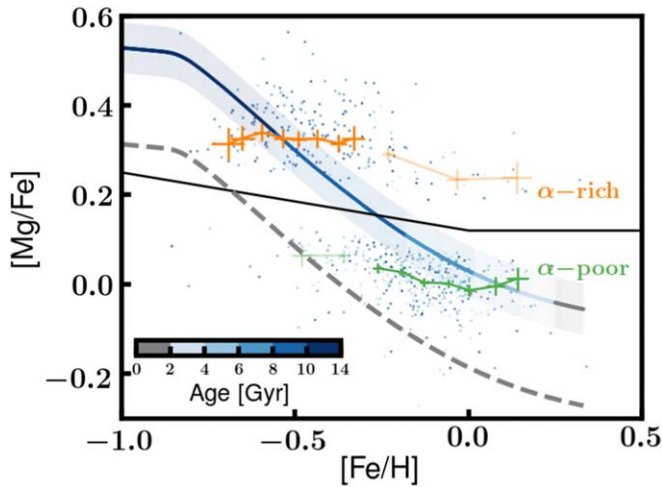


Figure 19. We divide our GALAH DR3 + K2 GAP DR3 sample into high- and low- α samples, following the proposed division from [K20](#) (Equation (9)). The stars indicated by orange points are accordingly classified as high- α stars, and the stars indicated by green points as low- α stars; the green and orange error bars and curves indicate the 2σ uncertainties on the binned weighted mean of the low- α and high- α stars. The Galactic chemical evolution model from [K20](#) is shown before (gray dotted curve) and after (blue segmented curve) an additive correction to $[\text{Mg}/\text{Fe}]$ to enforce agreement with the median $[\text{Mg}/\text{Fe}]$ of the observed stars. The region around the blue segmented curve reflects the 1σ uncertainty in the [K20](#) abundance normalization, taken to be the uncertainties in the solar abundances from [Asplund et al. \(2009\)](#). The transparency of the binned weighted means of the data emphasizes where the [K20](#) models track the high- α stars ($[\text{Fe}/\text{H}] \lesssim -0.3$ and $\tau \gtrsim 8\text{Gyr}$) and the low- α stars ($[\text{Fe}/\text{H}] \gtrsim -0.3$ and $\tau \lesssim 8\text{Gyr}$).

this sample, as well as their GALAH spectroscopic information, and high-/low- α classification are provided in Table 8.

We follow the example of [W19](#) and [GJW19](#) in considering abundance ratio and age-abundance patterns in $[\text{X}/\text{Mg}]$ space instead of only in $[\text{X}/\text{Fe}]$ space, due to the expectation that nearly all Mg production occurs in CCSNe, whereas Fe is produced by both CCSNe and SNe Ia. Therefore, the low- α population can be interpreted as having SNe Ia contributions, and the high- α population as being enriched by CCSNe. Normalizing by Mg means that elements produced only by CCSNe have the same trends in both the low- and high- α regimes. Elements with contributions from SNe Ia, however, will show a separation in $[\text{X}/\text{Mg}]$ versus $[\text{Mg}/\text{H}]$ that depends upon the relative contribution of CCSNe and SNe Ia. We note that other enrichment channels, like AGB winds, that do not behave precisely like CCSNe or SNe Ia in their Mg production and delay-time distributions may complicate interpretations of the $[\text{X}/\text{Mg}]$ versus $[\text{Mg}/\text{H}]$ trends. Ultimately, showing age-abundance patterns and abundance ratios in $[\text{Mg}/\text{H}]$ space in addition to $[\text{Fe}/\text{H}]$ space can offer complementary information to the asteroseismic age information. For instance, CCSNe elements would be expected to (1) have constant $[\text{X}/\text{Mg}]$ as a function of stellar age; (2) have decreasing $[\text{X}/\text{Fe}]$ as a function of stellar age; and (3) show similar $[\text{X}/\text{Mg}]$ trends as a function of $[\text{Mg}/\text{H}]$ for both high- and low- α populations.

We show the distribution of high- α ages in Figure 20. The filled orange histogram shows the distribution of high- α ages larger than 5 Gyr. The orange line indicates the distribution of a

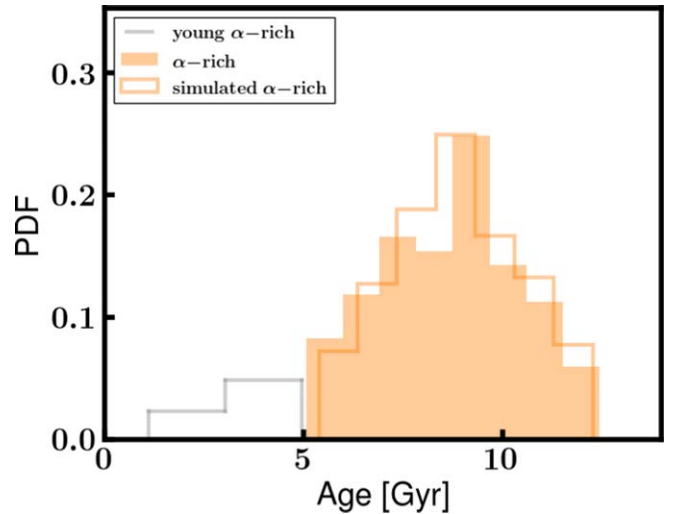


Figure 20. The distribution of high- α ages (filled orange) is consistent with being drawn from a uniform age of 9 Gyr (as simulated by the orange lines). A separate population of young high- α stars with ages $\lesssim 5$ Gyr is shown in gray, and is consistent with previous identifications of a young high- α population in the literature.

simulated population of these stars, assuming a mean age of 9 Gyr and with uncertainties taken from the fractional uncertainties of the data. The gray line indicates a population consistent with “young” high- α stars, which were originally identified in CoRoT ([Baglin et al. 2006](#)) and APOGEE data ([Chiappini et al. 2015](#)), and which have since been seen in Kepler and K2 data (e.g., [Martig et al. 2015](#); [Silva Aguirre et al. 2018](#); [Warfield et al. 2021](#)). These stars may be genuinely old but appear young due to having gained mass through stellar mergers (e.g., [Martig et al. 2015](#); [Jofré et al. 2016](#); [Izzard et al. 2018](#); [Sun et al. 2020](#)), or perhaps they are genuinely young and have formed in gas relatively unenriched by SNe Ia ([Chiappini et al. 2015](#); [Johnson et al. 2021](#)). We therefore draw a distinction between this population and the rest of the high- α population, which is consistent with a uniform age of ~ 9 Gyr according to a Kolmogorov–Smirnov test.

We show in Figures 21–29 abundance ratios ($[\text{X}/\text{Fe}]$ versus $[\text{Fe}/\text{H}]$ or $[\text{X}/\text{Mg}]$ versus $[\text{Mg}/\text{H}]$) and age-abundance patterns/enrichment histories ($[\text{X}/\text{Fe}]$ versus stellar age or $[\text{X}/\text{Mg}]$ versus stellar age) for different nucleosynthetic families of elements. A running weighted average of the data is shown as colored error bars connected by lines, with green indicating the low- α population and orange indicating the high- α population. Not plotted are stars with flagged GALAH DR3 abundance measurements in $[\text{Fe}/\text{H}]$ or in $[\text{X}/\text{Fe}]$. As mentioned above, the extent to which the low- α (green curves) pattern is above the high- α (orange curves) pattern in $[\text{X}/\text{Mg}]$ – $[\text{Mg}/\text{H}]$ space is generally indicative of a nucleosynthetic production site.

Regarding how to compare the [K20](#) models with the data in these figures, we note that at young and intermediate ages, the [K20](#) models may be best interpreted as a low- α population, while they represent a high- α population at old ages. Because the [K20](#) models are one-zone models, there is a one-to-one mapping of age to abundance, which is not necessarily the case in the data. To guide the eye, we therefore highlight in Figure 19 and subsequent figures where the data should be compared to the models: bold curves indicate solidly old/metal-poor high- α stars or young/metal-rich low- α stars,

³⁶ These are the number of stars with Mg and Fe measurements, which are necessary to define the high- α and low- α stars. Note that not all of these stars have abundance measurements for every element that we consider in what follows.

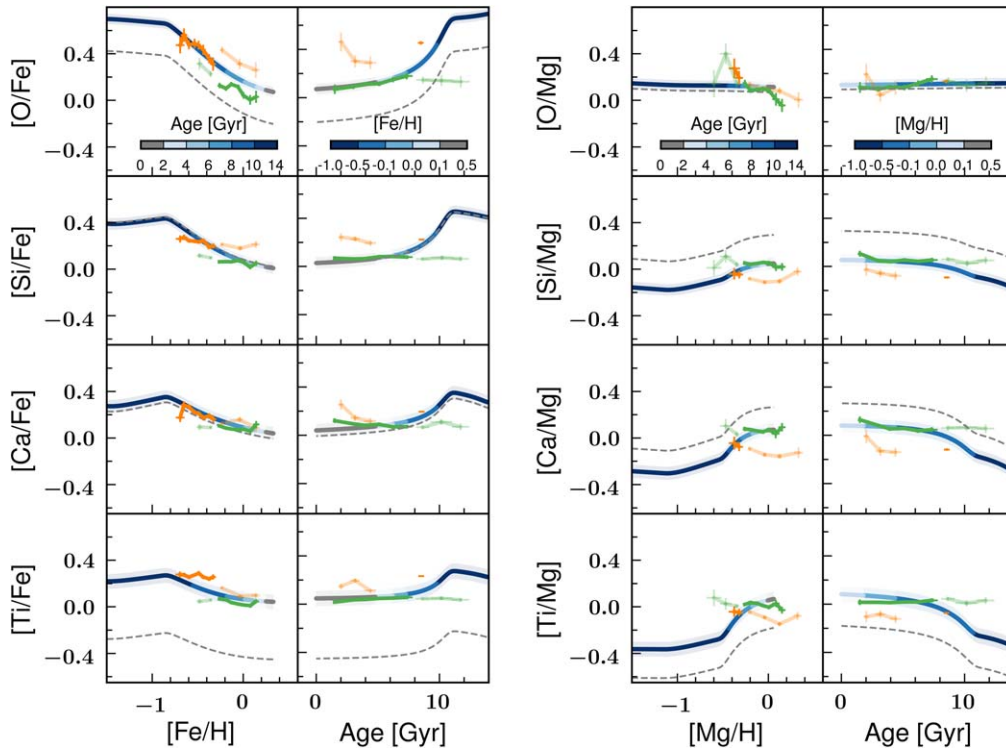


Figure 21. Abundance ratios and age-abundance patterns for α elements, shown in both $[X/\text{Fe}]$ and $[X/\text{Mg}]$ space. The green and orange error bars and curves indicate the 2σ uncertainties in the binned weighted means of the low- α and high- α stars. The blue segmented curves show the predictions from the Galactic chemical evolution model of K20, displaced additionally in X to agree with the median $[X/\text{Fe}]$ or $[X/\text{Mg}]$ of the observed stars (gray dashed curves indicate the models before this rescaling), and colored by either $[\text{Fe}/\text{H}]$, $[\text{Mg}/\text{H}]$, or age, according to the color bars. The transparencies in the weighted means of the data emphasize where the K20 models track the high- α stars ($[\text{Fe}/\text{H}] \lesssim -0.3$ and $\tau \gtrsim 5\text{Gyr}$) and the low- α stars ($[\text{Fe}/\text{H}] \gtrsim -0.3$ and $\tau \lesssim 8\text{Gyr}$). We note that not every star has GALAH measurements for every element, particularly at low metallicities.

Table 8
K2 GAP DR3 Ages with GALAH Spectroscopy

EPIC ID	subject_id	τ Gyr	σ_τ Gyr	$[\text{Fe}/\text{H}]$	$\sigma_{[\text{Fe}/\text{H}]}$	$[\text{Mg}/\text{Fe}]$	$\sigma_{[\text{Mg}/\text{Fe}]}$	T_{eff} K	$\sigma_{T_{\text{eff}}}$ K	α_{hi}
220387110	161007003801220	7.7	1.8	-0.2	0.1	0.2	0.1	4691	91	...
220352927	161007003801158	11.1	1.5	-1.3	0.1	0.1	0.1	4883	124	...
220420379	161007003801285	5.2	2.9	-0.6	0.1	0.3	0.2	4705	136	...
220329169	161007003801110	4.1	0.7	-0.3	0.1	0.1	0.1	4864	95	...
220425435	161007003801301	9.2	2.7	-1.6	0.2	0.1	0.2	5060	174	...
220377647	161007003801390	4.2	0.9	-0.4	0.1	0.2	0.1	4995	116	...
220382480	161007003801378	10.8	1.7	-0.7	0.2	0.2	0.2	5085	190	...
220392564	161007003801360	6.6	2.5	-0.9	0.1	0.3	0.2	4791	137	...
220408286	161007003801353	6.0	4.0	-0.2	0.1	0.1	0.1	4770	111	...
220272081	161006004401209	9.1	3.0	-0.6	0.1	0.4	0.1	4559	87	1

Note. Ages, GALAH metallicities, $[\text{Mg}/\text{Fe}]$, and effective temperatures for the subset of the K2 GAP DR3 sample with GALAH data. *subject_id* is the GALAH observation ID, which may be used to crossmatch with the GALAH catalogs. α_{hi} is 1 (0) if the star has GALAH abundances indicative of a high- α (low- α) star at 2σ confidence; if the classification is ambiguous, the entry is blank (see the text for details). A full version of this table is available in the online journal.

(This table is available in its entirety in machine-readable form.)

which are comparable to the K20-modeled populations shown in blue, whereas light curves indicate apparent young high- α or old low- α populations that are not directly comparable to the K20 models. To evaluate the agreement of the models with the data for older, high- α stars, we make reference here and in what follows to a single weighted average of the high- α abundances (which can be seen as a single orange error bar in the following figures), since the width of the high- α age distribution is dominated by uncertainties, and has a central value of ≈ 9 Gyr.

5.5. α Elements: O, Mg, Si, Ca, and Ti

Looking at O in Figure 21, it is clear that, after a global correction, the observed abundance ratios for $[\text{Fe}/\text{H}] > -1$ are in excellent agreement with the K20 model predictions. That the metallicity dependence of the O enrichment agrees with the observations is a built-in feature of the models: the K20 models are adjusted by tuning the total number of supernovae to agree with the observed O abundance metallicity dependence in the literature (K20). With age information in hand, however, we

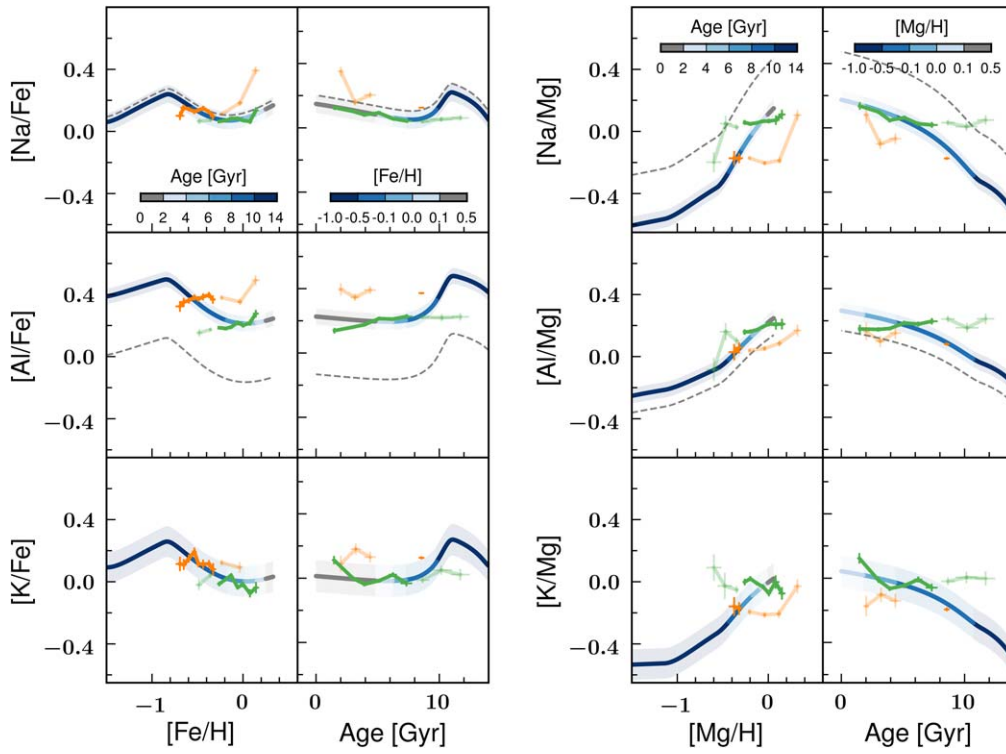


Figure 22. Same as Figure 21, but for light odd-Z elements.

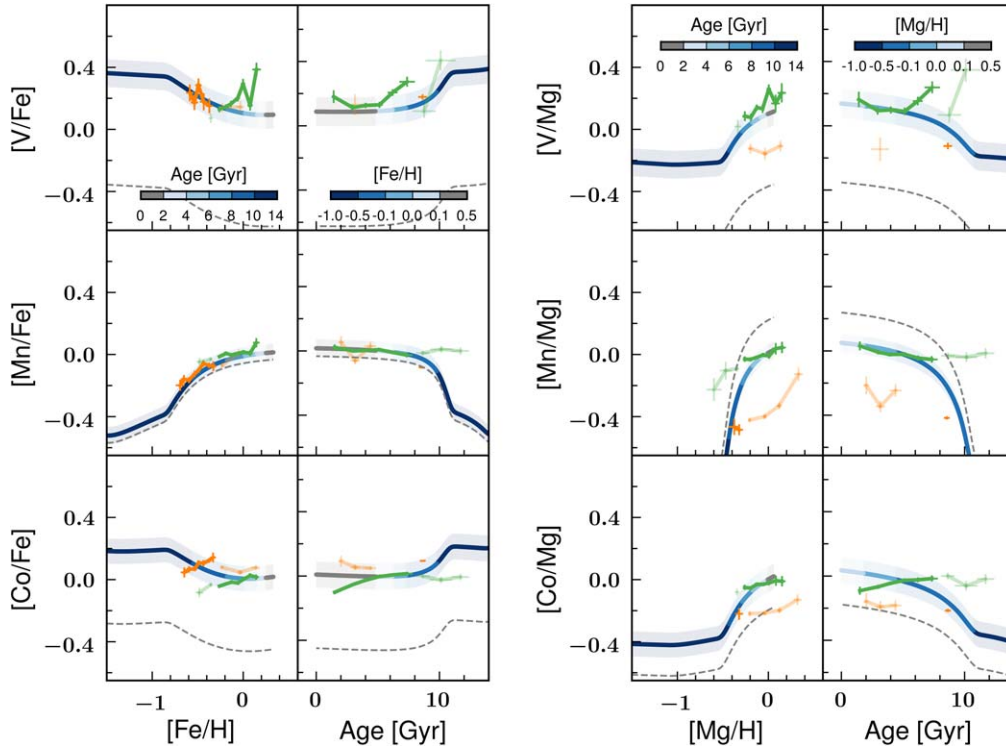


Figure 23. Same as Figure 21, but for odd-Z iron-peak elements.

can independently test the models. We see that the agreement is good when looking at the low- α [O/Mg] trend as a function of time up to $\tau \sim 8$ Gyr, tracking Mg production, as an α element would. We see that the high- α [O/Fe] enrichment history is in tension with the model predictions at 9 Gyr (orange error bar versus blue curve). Given the agreement of the high- α

population [O/Fe] as a function of [Fe/H], the disagreement of [O/Fe] for the high- α population in age space suggests an offset in the observed and predicted high- α ages. A natural solution would be to appeal to α -enhanced stellar model opacities. Indeed, Warfield et al. (2021) have demonstrated that the increase in stellar opacities due to nonsolar α abundances

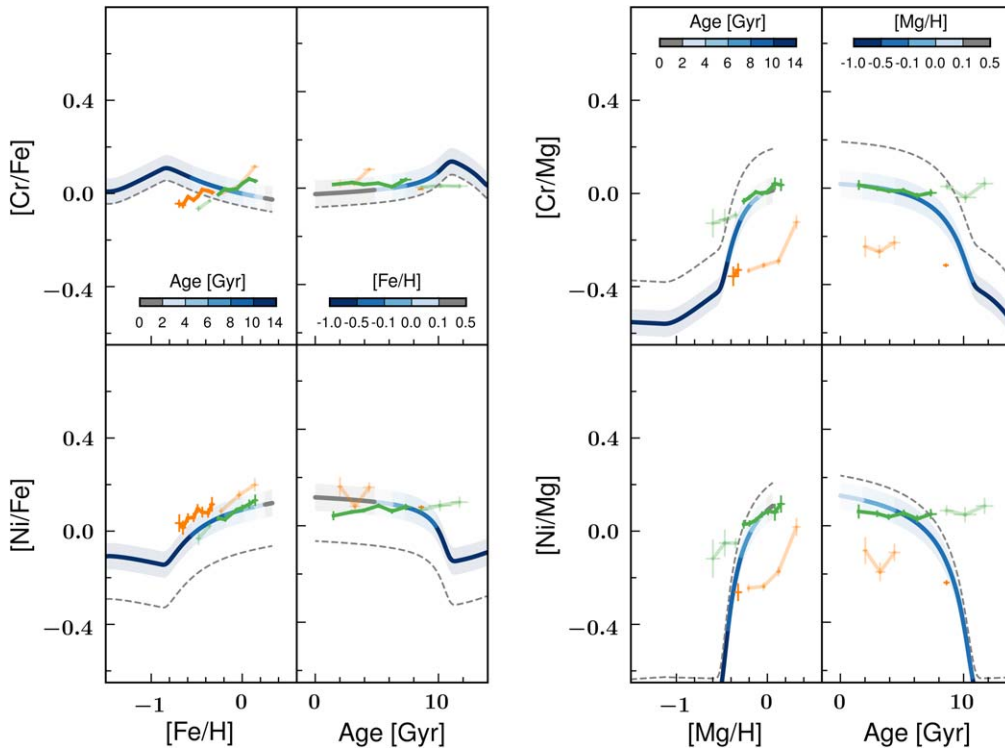


Figure 24. Same as Figure 21, but for even-Z iron-peak elements.

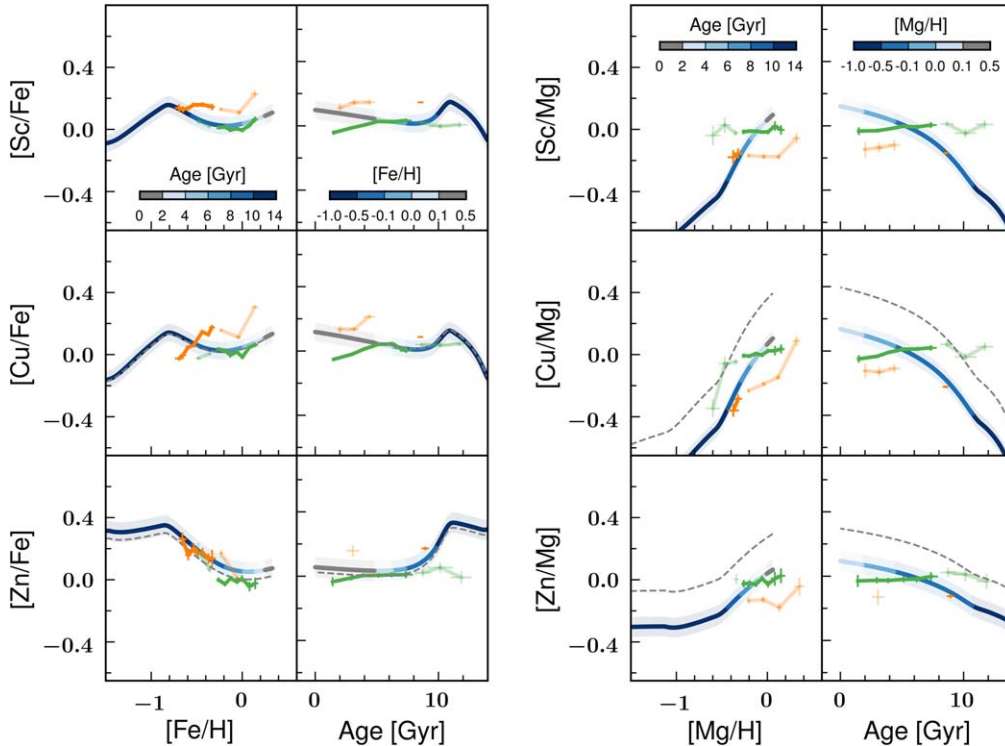


Figure 25. Same as Figure 21, but for iron-peak cliff elements.

can increase low-mass (old) stellar ages by $\approx 10\%$, by decreasing core temperature and extending a red giant’s main sequence lifetime. For the majority of the elements considered in what follows of Section 5, an increase in the high- α ages of that magnitude would improve the agreement between the data and the models. The global offset required to match the O abundances at high metallicities (blue curves versus gray

dashed curves) could be due to the GALAH α element abundances O, Mg, and Si having residual offsets of 0.1 dex, in the sense that giants have larger $[\alpha/\text{Fe}]$ compared to dwarfs even after non-LTE corrections (Amarsi et al. 2020).

Both Ca and Si in Figure 21 show good agreement between the predicted and the observed enrichment history: the predicted enrichment history at ages $\tau \lesssim 8$ Gyr tracks the

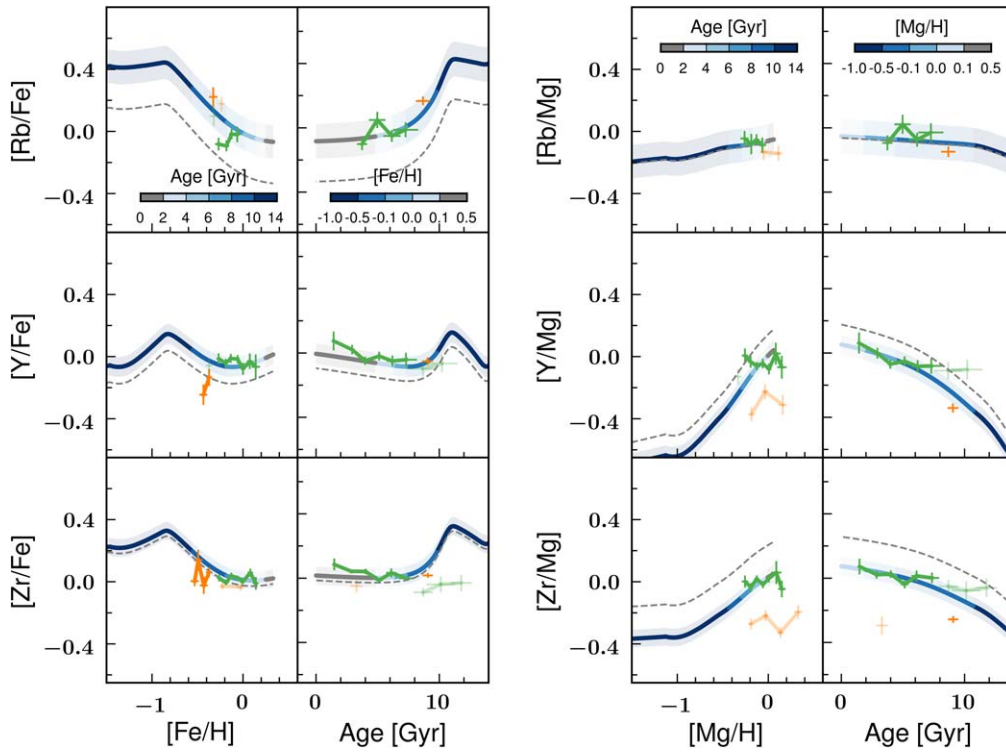


Figure 26. Same as Figure 21, but for weak s -process elements.

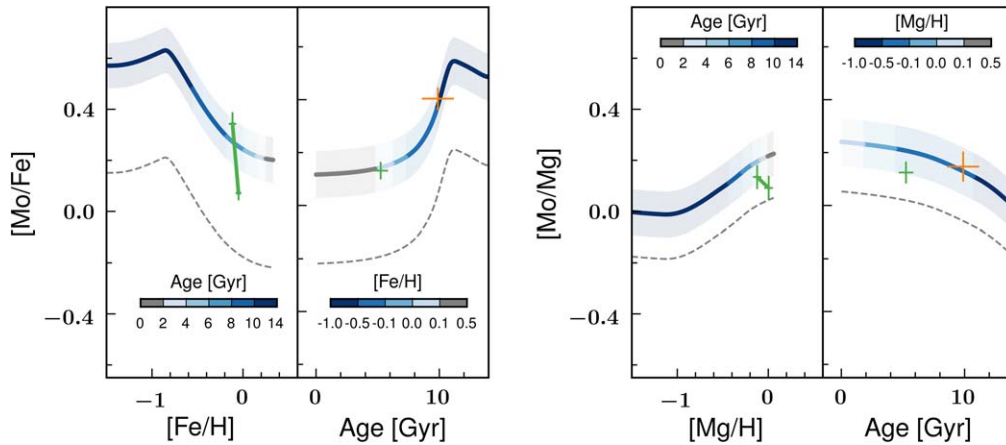


Figure 27. Same as Figure 21, but for the weak r -process element, Mo.

observed trend (green curve) in $[\text{Mg}/\text{H}]$ and $[\text{Fe}/\text{H}]$ space. The models also predict $[\text{Si}/\text{Fe}]$ at 9 Gyr consistent with the observed abundances of the old high- α population (orange error bar).

We consider Ti to be an α element, based on the findings in GJW19 that its production seems to be dominated by CCSNe contributions. Indeed, both the low- α and high- α curves share a similar $[\text{Ti}/\text{Mg}]$ in Figure 21. At older ages, however, the observed high- α $[\text{Ti}/\text{Fe}]$ abundances are in tension with the model predictions for 9 Gyr, which could be improved via older ages from the aforementioned α -enhanced stellar model opacities. Note that there is a large zero-point offset between the raw model abundances and the observed abundances (the offset to bring the raw model abundances into agreement with the observations is the difference between the gray dashed curves and the blue segmented curves), which is a

generic feature of nucleosynthetic Ti yield predictions, and may be remedied by two- or three-dimensional supernovae models (K20).

5.6. Light Odd-Z Elements: Na, Al, and K

Production of odd-Z elements is thought to depend upon progenitor metallicity, because their assumed production during explosive nucleosynthesis in CCSNe depends crucially upon the neutron excess prior to the supernova, which itself is dependent upon CNO cycle efficiency and therefore initial metal content (e.g., Truran & Arnett 1971). The predictions of the nucleosynthetic models for these elements, therefore, are that (1) they should follow a CCSNe enrichment history (either a decreasing $[\text{X}/\text{Fe}]$ with younger stellar ages or, equivalently, a constant $[\text{X}/\text{Mg}]$ with stellar age); and (2) they should be less abundant with decreasing metallicity. In Figure 22, we show

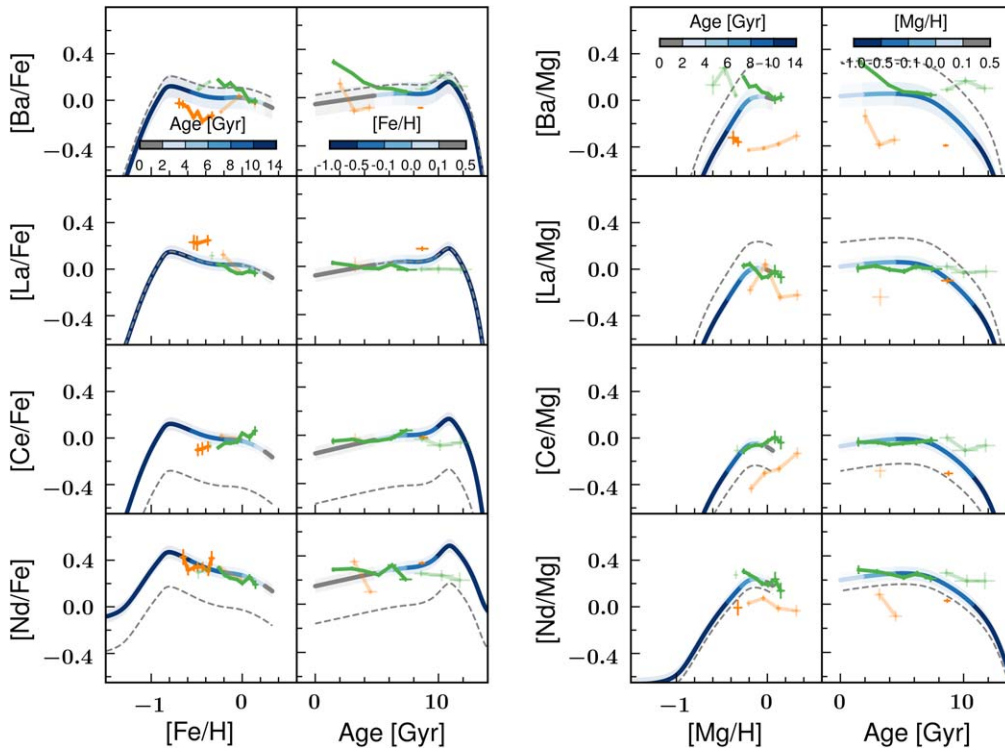


Figure 28. Same as Figure 21, but for main *s*-process elements.

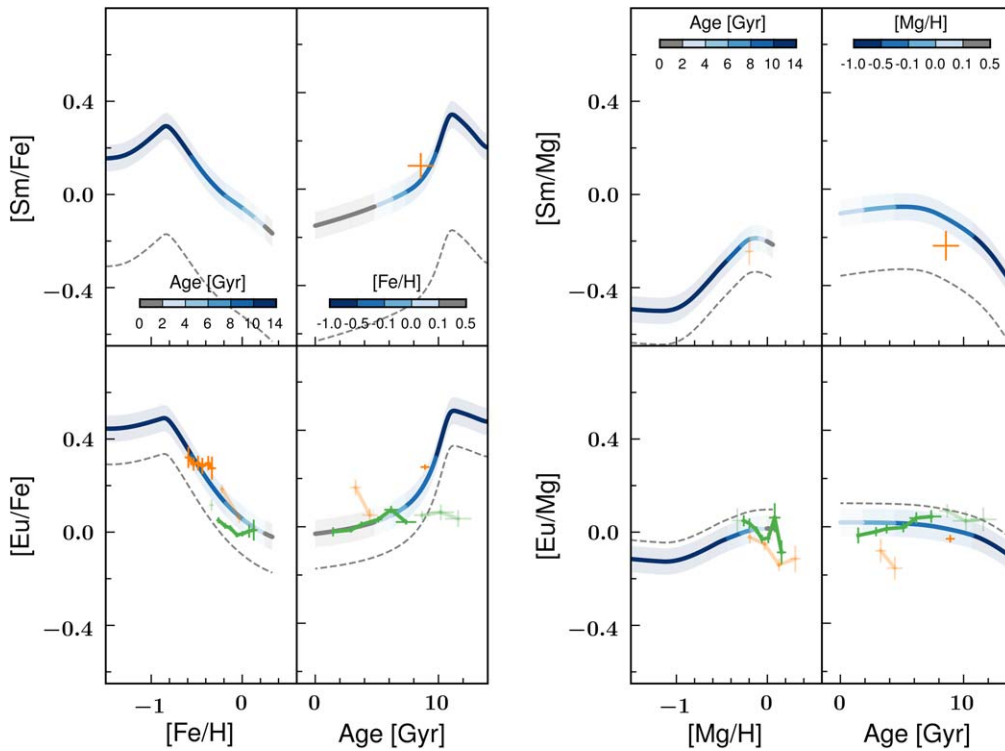


Figure 29. Same as Figure 21, but for main *r*-process elements.

the light odd-*Z* elements' abundance ratios and age-abundance patterns in order to test these predictions.

The DR3 GALAH [Na/Mg] abundance ratios show a positive metallicity trend, consistent with findings from GJW19 using GALAH DR2, and broadly consistent with the predicted metallicity slope from the K20 models. The enrichment history

predictions appear to be consistent with the observations, across all of the ages probed (keeping in mind the lack of resolution in age space for the high- α stars, which, to within uncertainties, are drawn from a single age of ≈ 9 Gyr).

The strong negative metallicity gradient seen by GJW19 in [K/Mg] is less pronounced with non-LTE corrections to

GALAH DR3, and is in good agreement with the **K20** models in $[\text{Fe}/\text{H}]$ space. The absolute abundances from **K20** for K, however, are well below the observed values (the gray dashed curve is below the plotted region), and this offset may be alleviated by appealing to, e.g., rotating stellar models (**K20**, and references therein). The predicted abundances at old stellar age are consistent with those observed among high- α at 9 Gyr.

The non-LTE GALAH DR3 corrections to Al reveal a strong metallicity trend, with $[\text{Al}/\text{Mg}]$ not being found in the GALAH DR2 abundances, corroborating the positive trend found in the APOGEE abundances (**GJW19**). We confirm **GJW19**'s interpretation of Al being produced largely during CCSNe production, given the relatively small separation between the high- and low- α tracks (orange and green curves in $[\text{Mg}/\text{H}]$ space) compared to, e.g., Na. These observations are both consistent with the theoretical predictions of significant metallicity-dependent Al production during explosive C burning (Truran & Arnett 1971). The observed and predicted enrichment histories are in disagreement. As with O, older high- α ages, resulting from α -enhanced stellar model opacities, could improve agreement at old ages. This adjustment would also bring Na and K into even better agreement at old ages. As with K, the absolute yields are severely underpredicted. This may very well be due to an overprediction of the abundances on the observational side: even after non-LTE corrections, the GALAH Al abundances for giants are larger than the abundances for dwarfs by 0.2 dex (Amarsi et al. 2020).

5.7. Iron-peak Elements

Following **GJW19**'s typology of iron-peak elements, we categorize the elements just beyond iron as cliff elements, which seem to have distinct properties from other iron-peak elements. First, we consider the odd-Z iron-peak elements, then the even-Z elements, and then, finally, the iron-peak cliff elements.

5.7.1. Odd-Z Iron-peak Elements: V, Mn, and Co

In this section, we discuss the odd-Z iron-peak element abundance patterns and enrichment histories, as shown in Figure 23. First, we confirm with GALAH DR3 the metallicity trends at high metallicities in V and Mn abundances, as noted by **W19** and **GJW19** using APOGEE and GALAH DR2 abundances, respectively. This metallicity-dependent effect is most pronounced in Mn, and is in excellent agreement with the model predictions of the trend, which are the result of Mn production occurring during deflagrations in the single-degenerate scenario (Kobayashi et al. 2020b). That the non-LTE Mn abundances from GALAH DR3 still show a metallicity dependence is in contrast to the decrease in metallicity dependence from LTE to non-LTE found in Battistini & Bensby (2016).

The observed low- α V pattern agrees well with the **K20**-predicted $[\text{V}/\text{Mg}]$ enrichment history, including at older ages, where the observed high- α abundances at 9 Gyr broadly agree with the predicted abundances. Nevertheless, the model abundances are uniformly vastly underpredicted compared to the observations before rescaling is applied (the gray dashed curves). This underprediction could be remedied, however, by using the yields from multidimensional supernovae yield predictions (**K20**).

The observed and predicted metallicity dependences for Mn are in very good agreement. The **K20** models also reproduce well the enrichment history of $[\text{Mn}/\text{Mg}]$ and $[\text{Mn}/\text{Fe}]$ in the low- α regime. For the old high- α populations, however, both the $[\text{Mn}/\text{Mg}]$ and $[\text{Mn}/\text{Fe}]$ enrichment histories could be improved with older high- α ages resulting from α -enhanced stellar model opacities (thereby shifting the orange error bar at 9 Gyr to older ages in the Mn enrichment history panels of Figure 23).

The Co enrichment history agrees well in $[\text{Co}/\text{Mg}]$ space at old ages, though **K20** predicts too-fast enrichment in the younger low- α population (the slope of the blue segmented curve versus the slope of the green curve). As with V, the models significantly underpredict the global abundances for Co.

5.7.2. Even-Z Iron-peak Elements: Cr and Ni

To better reproduce the $[\text{Cr}/\text{Fe}]$ enrichment history and the $[\text{Cr}/\text{Fe}]-[\text{Fe}/\text{H}]$ ratios as seen in Figure 24, overall $[\text{Cr}/\text{Fe}]$ production could be made to be less, such as in the double-degenerate scenario (the green dotted curve of Figure 18 in **K20**). Note, however, that such low $[\text{Cr}/\text{Fe}]$ results in higher $[\alpha/\text{Fe}]$ and lower $[\text{Mn}/\text{Fe}]$ and $[\text{Ni}/\text{Fe}]$ than observed. Otherwise, the observed enrichment history is flatter than that predicted in $[\text{Fe}/\text{H}]$ space, but is in better agreement with the models for $[\text{Mg}/\text{H}]$ space. The disagreement between observed and predicted high- α $[\text{Cr}/\text{Mg}]$ cannot be redressed only with the aforementioned appeals to older high- α ages resulting from α -enhanced stellar model opacities, which would increase the tension in high- α $[\text{Cr}/\text{Fe}]$. Rather, this would need to be coupled with a significant decrease in the production of Cr at early times.

Like Cr, the observed age-abundance pattern of Ni in $[\text{Fe}/\text{H}]$ space seen in Figure 24 is flatter than predicted. Though there is broad agreement between the $[\text{Ni}/\text{Fe}]$ and $[\text{Ni}/\text{Mg}]$ high- α enrichment history, it could be improved by an increase (as opposed to a decrease, as for Cr) in Ni at early times, combined with older high- α ages resulting from α -enhanced stellar model opacities, as mentioned earlier. There is also an offset between the raw model abundances (the gray dashed curves) and the observed abundances, though the offset is in the opposite direction to that of Cr. Note that the metallicity dependence is in good agreement with the model predictions in $[\text{Ni}/\text{Fe}]-[\text{Fe}/\text{H}]$ space, in contrast to Cr.

5.7.3. Iron-peak Cliff Elements: Sc, Cu, and Zn

Looking at Figure 25, the observed and predicted $[\text{Zn}/\text{Fe}]$ versus $[\text{Fe}/\text{H}]$ and age-abundance trends are in good agreement. The small separation in $[\text{Zn}/\text{Mg}]$ of the low- and high- α sequences corroborates the CCSNe-dominated production assumed in the **K20** models as well as the interpretations of the Zn abundance ratios in **GJW19** that Zn is mostly a CCSNe element.

The enrichment histories predicted by the **K20** models for Cu show strong increases in both $[\text{Cu}/\text{Mg}]$ and $[\text{Cu}/\text{Fe}]$ for younger stellar ages, which are in disagreement with the slight trend in the other direction among the low- α population (the green curves in Figure 25) in both $[\text{Fe}/\text{H}]$ and $[\text{Mg}/\text{H}]$ space. Slightly higher high- α ages in the data would help to reconcile the observed and predicted $[\text{Cu}/\text{Fe}]$.

The Sc age-abundance patterns in Figure 25 show the same behavior as Cu: the models predict an age-dependent trend in the opposite direction to that of the observed trends in [Fe/H] and [Mg/H] space, and the observed high- α population is offset in age compared to the models.

Taken together, the Cu and Sc trends are suggestive of different nucleosynthetic histories compared to Zn. The predicted increase in the Cu and Sc yields is theoretically expected, due to the metallicity dependence of Cu and Sc yields, since both elements are odd-Z (see Section 5.6). Indeed, the data show this increase in [Cu/Fe], and at least a flat trend in [Sc/Fe] with [Fe/H] among the low- α population. The observed age trend (a flat or increasing abundance with increasing age among low- α stars) is therefore not straightforwardly related to metallicity-dependent yields, and is an interesting constraint on production of these elements; a similar enrichment history is also seen in the odd-Z element Al (see Section 5.6).

5.8. Neutron-capture Elements

Neutron-capture elements can be produced in one of two primary channels: the *s*-process and *r*-process channels, which occur in neutron-poor and neutron-rich environments (for a review, see Truran et al. 2002).

There is evidence of two different kinds of *r*-process production: a “weak” process that creates elements $A \lesssim 130$ –140 (e.g., Honda et al. 2004) and the main *r*-process for elements with $A \gtrsim 130$ –140 (Truran et al. 2002). The main *r*-process production site has been proposed to be decompressing neutron-rich ejecta from a neutron star–neutron star (NS–NS) merger (Lattimer & Schramm 1974; Lattimer et al. 1977; Rosswog et al. 1999). However, the delay-time distribution of NS–NS mergers is difficult to reconcile with that needed to reproduce observed *r*-process enrichment histories, both at early and late times (e.g., Hotokezaka et al. 2018; Haynes & Kobayashi 2019). Other *r*-process channels involving neutrino-driven winds during neutron or magnetar birth may be plausible alternatives (e.g., Qian & Woosley 1996; Hoffman et al. 1997).

As with the *r*-process, there seem to be weak and main kinds of *s*-process. The weak *s*-process occurs during core He burning of $M > 25M_{\odot}$ stars (Peters 1968; Lamb et al. 1977; Raiteri et al. 1993), and works by way of neutron production from the $^{22}\text{Ne}(\alpha, n)^{25}\text{Mg}$ reaction, creating free neutrons that can then build elements up to $A \approx 90$ (Truran et al. 2002). The main *s*-process occurs during the AGB phase of low- and intermediate-mass stars ($M \sim 1$ – $3M_{\odot}$; Schwarzschild & Härm 1967), acting through the $^{13}\text{C}(\alpha, n)^{16}\text{O}$ reaction, and forming elements with $A \gtrsim 90$.

With K2 GAP DR3 age estimates and GALAH DR3 abundances, we are in a position to test assumed production mechanisms of neutron-capture elements by means of comparisons to the K20 models.

Electron-capture supernovae (ECSNe) are included as sources of neutron-capture elements in the K20 models, the effects of which are to form first-peak *s*-process elements Sr, Y, Zr, Mo, and Ru via nuclear equilibrium processes, as well as weak *r*-process production from Nd to In (Wanajo et al. 2011). ECSNe are assumed in the K20 models to occur in the relatively narrow mass range of ~ 8.8 – $9M_{\odot}$; increases of an order of magnitude to the ECSN rate have been assumed in the literature, and so this may be a tunable parameter in order to

increase bulk yields (see K20 and references therein). The largest contributors to *r*-process production in the K20 models, however, are magneto-rotational supernovae (MRSNe), which have been theorized as being CCSNe of massive stars with large magnetic fields and/or strong rotations, which develop accretion disks and jets that can be conducive to *r*-process production (e.g., Symbalisty et al. 1985; Cameron 2003; Nishimura et al. 2017). An NS–NS merger *r*-process contribution is also included in the K20 models, though its contribution is subdominant compared to that of MRSNe.

5.8.1. Weak *s*-process Elements: Rb, Y, and Zr

Shown in Figure 26 are the age-abundance ratios of elements thought to be formed through the “weak” *s*-process.³⁷

The agreement between the observed and predicted age-abundance patterns of [Rb/Mg] and [Rb/Fe] is very good, across both high- and low- α populations.

Although there is an overprediction in the abundances for the high- α stars at 9 Gyr, the agreement between the K20 models and data are good for [Zr/Mg] and [Zr/Fe] as well.

The K20 age–[Y/Mg] pattern does not reach an equilibrium value, indicating a metallicity dependence on the *s*-process production of Y. This metallicity dependence is also borne out in the data, save for a zero-point offset in [Y/Mg]. The predicted enrichment history is in good agreement in both [Y/Mg] and [Y/Fe] space. The agreement between the observed and predicted Y enrichment histories represents another endorsement of dating stars with Y abundances (e.g., Nissen 2015).

5.8.2. Weak *r*-process Element: Mo

Although GALAH can measure Ru, the number of stars with good Ru measurements is small, and so we only consider Mo as being representative of elements produced as part of the so-called “weak” *r*-process.

The K20 models underpredict Mo compared to GALAH (gray curve versus error bars in Figure 27), which is inconsistent with the inferred overproduction compared to high-resolution Mo abundance measurements in the literature (K20). Nevertheless, the predicted history of Mo enrichment is consistent with the observed [Mo/Fe] and [Mo/Mg] age-abundance patterns (the blue curve compared to the error bars).

5.8.3. Main *s*-process Elements: Ba, La, Ce, and Nd

Ba, shown in Figure 28, is thought to be primarily produced by the *s*-process at the metallicities considered here ([Fe/H] > -2 ; Gilroy et al. 1988; Arlandini et al. 1999; Burris et al. 2000). [Ba/Mg] is predicted to reach a plateau in young stars, according to the K20 models, but the data disfavor a plateau and rather suggest a continually increasing ratio with younger ages, like [Y/Mg].

D’Orazi et al. (2009) have observed a similar unexpected increase in [Ba/Fe] at young stellar ages, based on open cluster measurements. They proposed that increased production in low-mass stars would explain the observations, which could possibly be related to enhanced mixing in the helium-burning shell thought to be the site of *s*-process production in low- and

³⁷ In detail, the K20 models predict that Y and Zr are in fact produced mostly in low- and intermediate-mass AGB stars as part of what we label here the main *s*-process.

intermediate-mass AGB stars. Similar behavior has also been seen in more recent studies (Mishenina et al. 2013; Magrini et al. 2018; Casamiquela et al. 2021). It is unlikely that this enrichment history is explicable by an astrophysical, metallicity-dependent yield, since $[\text{Ba}/\text{Fe}]$ decreases with increasing $[\text{Fe}/\text{H}]$, which demonstrates the advantage of analyzing nucleosynthetic yields with age information.

Our results therefore corroborate a mass-dependent Ba yield interpretation, though it is possible that the GALAH DR3 Ba abundances themselves could be responsible: a trend in Ba with stellar mass would mimic this effect. One candidate for such a systematic may be the choice of the microturbulence parameter, given the sensitivity of one of the GALAH Ba lines, Ba II, to that parameter (Dobrovolskas et al. 2012). The GALAH DR3 Ba abundances are calculated by assuming that RGB stars with the same effective temperature, surface gravity, and $[\text{Fe}/\text{H}]$ have the same microturbulence velocity. This is not necessarily the case, and such assumptions could lead to artificial shifts in the measured Ba abundance with, e.g., mass/age. Regarding the zero-point offset in the Ba abundances compared to the K20 models under no rescaling (the gray dashed lines), the RGB Ba abundances are systematically larger than the dwarf abundances by 0.2 dex. Were the RGB Ba abundances placed on the dwarf scale, then, there would be an even larger global offset between the observations and models than is shown here. On the model side, K20 noted offsets compared to other Ba abundances in the literature, noting that they could be remedied by imposing a smaller mixing region during the AGB dredge-up. Based on our findings, the models may improve the agreement with the observations more specifically, with a mass-dependent increase in the mixing region.

The predicted and observed enrichment histories of La, Ce, and Nd are in good agreement, as seen in Figure 28. The exception to this agreement is Ce among high- α stars, which is low compared to the predictions, even after considering a $\approx 10\%$ increase in the observed ages, potentially indicating the need for less Ce production in the K20 models at early times.

5.8.4. Main r -process Elements: Sm and Eu

We show in Figure 29 the abundances of the two main r -process elements available in GALAH DR3, Sm and Eu.

Given the relatively few stars in GALAH DR3 with measured Sm abundances, it is difficult to determine the precise agreement with the K20 models as a function of age. It does, however, appear that the high- α abundances at old ages are broadly consistent with the predicted enrichment histories, though they could be further improved with older high- α ages resulting from α -enhanced stellar opacities.

Eu is mostly produced via the r -process (Arlandini et al. 1999; Battistini & Bensby 2016), and, according to the K20 models, the primary site of r -process production is MRSNe (see Figure 32 in K20), where the rate of MRSNe is chosen to be 3% of massive CCSNe (hypernovae) with mass $M > 25M_{\odot}$, in order to reproduce the $[\text{Eu}/\text{Fe}]$ – $[\text{Fe}/\text{H}]$ trend in the solar neighborhood.

The K20 models are in good agreement with both the GALAH abundance ratios and the asteroseismic age-abundance patterns in $[\text{Eu}/\text{Fe}]$, when comparing the models to low- α stars (the green curves) at intermediate and young ages ($\tau \lesssim 8\text{Gyr}$) and when comparing the models to high- α stars (the orange error bars at 9 Gyr in the Eu enrichment history panels of Figure 29) at older ages. Consistent with studies of

metal-poor systems with significant r -process enrichment (e.g., Barklem et al. 2005; Hansen et al. 2018), Lin et al. (2020) have corroborated the short time-delay of Eu production sites by using isochronal stellar ages of subgiants combined with GALAH DR2 abundances. In this context, the agreement of the observed K2 GAP DR3–GALAH DR3 Eu enrichment history with that of the MNSRe-dominated K20 Eu models gives further credence to a significant contribution to r -process elements from a prompt source—e.g., late-time collapsar accretion disk outflows associated with MRSNe (Symbalisty et al. 1985; Cameron 2003; Nicholl et al. 2013; Vlasov et al. 2014; Siegel et al. 2019).

6. Conclusions

The K2 GAP DR3 sample, as the largest asteroseismic sample published to date, which probes a range of Galactic environments, represents an important tool for Galactic archeology and stellar physics. With 18,821 total radius and mass coefficients for RGB and RC stars having been delivered as part of this final data release, below are our main results.

1. We calibrated our asteroseismic values to be on the Gaia parallactic scale. The radius and mass coefficients— κ_R and κ_M —that are released in K2 GAP DR3 need only be multiplied by a temperature-dependent factor according to the user’s preferred temperatures in order to yield radii and masses. The typical uncertainties in these coefficients are 2.9% (stat.) $\pm 0.1\%$ (syst.) and 6.7% (stat.) $\pm 0.3\%$ (syst.) in κ_R and κ_M for RGB stars and 4.7% (stat.) $\pm 0.3\%$ (syst.) and 11% (stat.) $\pm 0.9\%$ (syst.) for RC stars. All of the stars with κ_R and κ_M are classified as RGB or RC stars, according to a machine-learning approach.
2. Using injection tests, we estimate that our completeness in radius peaks for stars with $R \sim 10R_{\odot}$, where our recovery rate is around 80%. There is a sharp decline in completeness at smaller radii, and a more gradual decline in completeness at larger radii. We estimate a nearly uniform completeness in mass space of $\sim 60\%$.
3. Injection tests suggest systematics of 1%–3% may arise due to the shorter time baseline of K2 compared to Kepler, taking the form of both zero-point biases and trends as a function of ν_{max} , $\Delta\nu$, and S/N. These findings should be informative for future studies using short time baseline TESS light curves, which would presumably suffer from similar, if not more severe, systematics.
4. We derived ages with typical precisions of 20% for a subset of the K2 GAP DR3 sample, based on GALAH metallicities and effective temperatures. In combination with the GALAH abundances, we compared the observed age-abundance patterns with those predicted by Kobayashi et al. (2020a) as an independent check on the abundance evolution of low- and high- α stars. We corroborate recent inferences regarding the nucleosynthesis of α , light, iron-peak, and neutron-capture elements based on abundance ratios alone (e.g., Griffith et al. 2019). Following similar indications from the Lin et al. (2020) analysis of GALAH DR2 subgiants with isochronal ages, we find evidence for significant production of Eu at early times, consistent with CCSNe as the predominant site of r -process production. Our findings also suggest mass-dependent Ba yields, in support of indications from D’Orazi et al. (2009).

Studies of Galactic chemical evolution stand to benefit enormously from a continued focus on considering ages, and not just stellar abundances themselves, as we have shown here. Indeed, ages are of crucial importance in interpreting chemokinematic relations (Minchev et al. 2019)—particularly ages with the levels of precision reported here (e.g., Martig et al. 2014). As the largest asteroseismic data set in the literature, K2 GAP DR3 will prove useful not only for Galactic studies, but also for testing stellar models using the sample’s evolutionary state classifications together with its accurate and precise asteroseismic masses and radii.

We would like to thank the anonymous referee whose comments significantly improved the manuscript. J.C.Z. is supported by an NSF Astronomy and Astrophysics Postdoctoral Fellowship under award AST-2001869. J.C.Z. and M.H.P. acknowledge support from NASA grants 80NSSC18K0391 and NNX17AJ40G. Y.E. and C.J. acknowledge the support of the UK Science and Technology Facilities Council (STFC). S.M. acknowledges support from the Spanish Ministry of Science and Innovation with the Ramon y Cajal fellowship number RYC-2015-17697 and the grant number PID2019-107187GB-I00. R.A.G. acknowledges funding received from the PLATO CNES grant. C.K. acknowledges funding from the UK Science and Technology Facilities Council (STFC) through grants ST/M000958/1, ST/R000905/1, and ST/V000632/1.

Funding for the Stellar Astrophysics Centre (SAC) is provided by the Danish National Research Foundation (grant agreement No. DNR106).

The K2 Galactic Archaeology Program is supported by the National Aeronautics and Space Administration under grant NNX16AJ17G issued through the K2 Guest Observer Program. This publication makes use of data products from the Two Micron All Sky Survey, which is a joint project of the University of Massachusetts and the Infrared Processing and Analysis Center/California Institute of Technology, funded by the National Aeronautics and Space Administration and the National Science Foundation.

This paper includes data collected by the Kepler mission. Funding for the Kepler mission is provided by the NASA Science Mission directorate.

Parts of this research were supported by the Australian Research Council Centre of Excellence for All Sky Astrophysics in 3 Dimensions (ASTRO 3D), through project number CE170100013.

This research was partially conducted during the Exostar19 program at the Kavli Institute for Theoretical Physics at UC Santa Barbara, which was supported in part by the National Science Foundation under grant No. NSF PHY-1748958.

Based in part on data obtained at Siding Spring Observatory via GALAH. We acknowledge the traditional owners of the land on which the AAT stands, the Gamilaraay people, and pay our respects to elders past and present.

This work has made use of data from the European Space Agency (ESA) mission Gaia (<https://www.cosmos.esa.int/gaia>), processed by the Gaia Data Processing and Analysis Consortium (DPAC, <https://www.cosmos.esa.int/web/gaia/dpac/consortium>). Funding for DPAC has been provided by national institutions, in particular the institutions participating in the Gaia Multilateral Agreement.

Funding for the Sloan Digital Sky Survey IV has been provided by the Alfred P. Sloan Foundation, the U.S.

Department of Energy Office of Science, and the Participating Institutions. SDSS-IV acknowledges support and resources from the Center for High-Performance Computing at the University of Utah (www.sdss.org).

Software: asfgrid (Sharma & Stello 2016), corner (Foreman-Mackey 2016), emcee (Foreman-Mackey et al. 2013), NumPy (Walt 2011), pandas (McKinney 2010), Matplotlib (Hunter 2007), IPython (Pérez & Granger 2007), SciPy (Virtanen et al. 2020).

ORCID iDs

Joel C. Zinn  <https://orcid.org/0000-0002-7550-7151>
 Dennis Stello  <https://orcid.org/0000-0002-4879-3519>
 Rafael A. García  <https://orcid.org/0000-0002-8854-3776>
 Thomas Kallinger  <https://orcid.org/0000-0003-3627-2561>
 Savita Mathur  <https://orcid.org/0000-0002-0129-0316>
 Benoît Mosser  <https://orcid.org/0000-0002-7547-1208>
 Marc Hon  <https://orcid.org/0000-0003-2400-6960>
 Lisa Bugnet  <https://orcid.org/0000-0003-0142-4000>
 Sanjib Sharma  <https://orcid.org/0000-0002-0920-809X>
 Jack T. Warfield  <https://orcid.org/0000-0003-1634-4644>
 Rodrigo Luger  <https://orcid.org/0000-0002-0296-3826>
 Andrew Vanderburg  <https://orcid.org/0000-0001-7246-5438>
 Chiaki Kobayashi  <https://orcid.org/0000-0002-4343-0487>
 Marc H. Pinsonneault  <https://orcid.org/0000-0002-7549-7766>
 Jennifer A. Johnson  <https://orcid.org/0000-0001-7258-1834>
 Daniel Huber  <https://orcid.org/0000-0001-8832-4488>
 Sven Buder  <https://orcid.org/0000-0002-4031-8553>
 Meredith Joyce  <https://orcid.org/0000-0002-8717-127X>
 Joss Bland-Hawthorn  <https://orcid.org/0000-0001-7516-4016>
 Luca Casagrande  <https://orcid.org/0000-0003-2688-7511>
 Geraint F. Lewis  <https://orcid.org/0000-0003-3081-9319>
 Andrea Miglio  <https://orcid.org/0000-0001-5998-8533>
 Thomas Nordlander  <https://orcid.org/0000-0001-5344-8069>
 Guy R. Davies  <https://orcid.org/0000-0002-4290-7351>
 William J. Chaplin  <https://orcid.org/0000-0002-5714-8618>
 Victor Silva Aguirre  <https://orcid.org/0000-0002-6137-903X>

References

- Adibekyan, V. Z., Sousa, S. G., Santos, N. C., et al. 2012, *A&A*, 545, A32
 Ahumada, R., Prieto, C. A., Almeida, A., et al. 2020, *ApJS*, 249, 3
 Alonso, A., Arribas, S., & Martínez-Roger, C. 1999, *A&AS*, 139, 335
 Amarsi, A. M., Lind, K., Osorio, Y., et al. 2020, *A&A*, 642, A62
 Amarsi, A. M. 2020, Grid/NLTE, v3, Zenodo, doi:10.5281/zenodo.3982506
 An, D., Pinsonneault, M. H., Terndrup, D. M., & Chung, C. 2019, *ApJ*, 879, 81
 Anders, F., Chiappini, C., Rodrigues, T. S., et al. 2017, *A&A*, 597, A30
 Arlandini, C., Käppeler, F., Wisshak, K., et al. 1999, *ApJ*, 525, 886
 Asplund, M., Grevesse, N., Sauval, A. J., & Scott, P. 2009, *ARA&A*, 47, 481
 Baglin, A., Michel, E., & Auvergne, M. 2006, in ESA SP-624, Proc. of SOHO 18/GONG 2006/HELAS I, Beyond the Spherical Sun, ed. K. Fletcher (Noordwijk: ESA), 34
 Barklem, P. S., Christlieb, N., Beers, T. C., et al. 2005, *A&A*, 439, 129
 Battistini, C., & Bensby, T. 2016, *A&A*, 586, A49
 Bedding, T. R., Mosser, B., Huber, D., et al. 2011, *Natur*, 471, 608
 Belkacem, K., Goupil, M. J., Dupret, M. A., et al. 2011, *A&A*, 530, A142
 Belkacem, K., Samadi, R., Mosser, B., Goupil, M. J., & Ludwig, H. G. 2013, in ASP Conf. Ser. 479, Progress in Physics of the Sun and Stars: A New Era in Helio- and Asteroseismology, ed. H. Shibahashi & A. E. Lynas-Gray (San Francisco, CA: ASP), 61
 Belokurov, V., Erkal, D., Evans, N. W., Koposov, S. E., & Deason, A. J. 2018, *MNRAS*, 478, 611

- Bennett, M., & Bovy, J. 2019, *MNRAS*, **482**, 1417
- Bensby, T., Feltzing, S., & Lundström, I. 2003, *A&A*, **410**, 527
- Bland-Hawthorn, J., Sharma, S., Tepper-Garcia, T., et al. 2019, *MNRAS*, **486**, 1167
- Blanton, M. R., Bershad, M. A., Abolfathi, B., et al. 2017, *AJ*, **154**, 28
- Borucki, W. J., Koch, D., Basri, G., et al. 2010, *Sci*, **327**, 977
- Bovy, J., Rix, H.-W., Green, G. M., Schlafly, E. F., & Finkbeiner, D. P. 2016, *ApJ*, **818**, 130
- Brogaard, K., Hansen, C. J., Miglio, A., et al. 2018, *MNRAS*, **476**, 3729
- Brown, T. M., Gilliland, R. L., Noyes, R. W., & Ramsey, L. W. 1991, *ApJ*, **368**, 599
- Buder, S., Asplund, M., Duong, L., et al. 2018, *MNRAS*, **478**, 4513
- Buder, S., Sharma, S., Kos, J., et al. 2021, *MNRAS*, **506**, 150
- Burbidge, E. M., Burbidge, G. R., Fowler, W. A., & Hoyle, F. 1957, *RvMP*, **29**, 547
- Burris, D. L., Pilachowski, C. A., Armand roff, T. E., et al. 2000, *ApJ*, **544**, 302
- Cameron, A. G. W. 2003, *ApJ*, **587**, 327
- Campante, T. L., Schofield, M., Kuzlewicz, J. S., et al. 2016, *ApJ*, **830**, 138
- Carlberg, R. G., & Sellwood, J. A. 1985, *ApJ*, **292**, 79
- Casagrande, L., Silva Aguirre, V., Schlesinger, K. J., et al. 2016, *MNRAS*, **455**, 987
- Casamiquela, L., Soubiran, C., Jofré, P., et al. 2021, *A&A*, **652**, A25
- Chan, V. C., & Bovy, J. 2020, *MNRAS*, **493**, 4367
- Chaplin, W. J., Houdek, G., Appourchoux, T., et al. 2008, *A&A*, **485**, 813
- Chiappini, C., Anders, F., Rodrigues, T. S., et al. 2015, *A&A*, **576**, L12
- Chiappini, C., Matteucci, F., & Gratton, R. 1997, *ApJ*, **477**, 765
- Clarke, A. J., Debattista, V. P., Nidever, D. L., et al. 2019, *MNRAS*, **484**, 3476
- Corsaro, E., Fröhlich, H. E., Bonanno, A., et al. 2013, *MNRAS*, **430**, 2313
- De Silva, G. M., Freeman, K. C., Bland-Hawthorn, J., et al. 2015, *MNRAS*, **449**, 2604
- Dobrovol'skas, V., Kučinskias, A., Andrievsky, S. M., et al. 2012, *A&A*, **540**, A128
- D'Orazi, V., Magrini, L., Randich, S., et al. 2009, *ApJL*, **693**, L31
- Epstein, C. R., Elsworth, Y. P., Johnson, J. A., et al. 2014, *ApJL*, **785**, L28
- Foreman-Mackey, D. 2016, *JOSS*, **1**, 24
- Foreman-Mackey, D., Hogg, D. W., Lang, D., & Goodman, J. 2013, *PASP*, **125**, 306
- Fuhrmann, K. 1998, *A&A*, **338**, 161
- Gaia Collaboration, Brown, A. G. A., Vallenari, A., et al. 2016, *A&A*, **595**, A2
- Gaia Collaboration, Brown, A. G. A., Vallenari, A., et al. 2018, *A&A*, **616**, A1
- García Pérez, A. E., Allende Prieto, C., Holtzman, J. A., et al. 2016, *AJ*, **151**, 144
- García, R. A., Mathur, S., Pires, S., et al. 2014, *A&A*, **568**, A10
- Gilroy, K. K., Sneden, C., Pilachowski, C. A., & Cowan, J. J. 1988, *ApJ*, **327**, 298
- González Hernández, J. I., & Bonifacio, P. 2009, *A&A*, **497**, 497
- Grand, R. J. J., Springel, V., Gómez, F. A., et al. 2016, *MNRAS*, **459**, 199
- Gratton, R. G., Carretta, E., Matteucci, F., & Sneden, C. 2000, *A&A*, **358**, 671
- Gravity Collaboration, Abuter, R., Amorim, A., et al. 2019, *A&A*, **625**, L10
- Green, G. M., Schlafly, E. F., Finkbeiner, D. P., et al. 2015, *ApJ*, **810**, 25
- Griffith, E., Johnson, J. A., & Weinberg, D. H. 2019, *ApJ*, **886**, 84
- Gunn, J. E., Siegmund, W. A., Mannery, E. J., et al. 2006, *AJ*, **131**, 2332
- Hachisu, I., Kato, M., & Nomoto, K. 1996, *ApJL*, **470**, L97
- Hall, O. J., Davies, G. R., Elsworth, Y. P., et al. 2019, *MNRAS*, **486**, 3569
- Handberg, R., & Lund, M. N. 2014, *MNRAS*, **445**, 2698
- Hansen, T. T., Holmbeck, E. M., Beers, T. C., et al. 2018, *ApJ*, **858**, 92
- Hayden, M. R., Bovy, J., Holtzman, J. A., et al. 2015, *ApJ*, **808**, 132
- Hayden, M. R., Recio-Blanco, A., de Laverny, P., Mikolaitis, S., & Worley, C. C. 2017, *A&A*, **608**, L1
- Hayek, W., Asplund, M., Collet, R., & Nordlund, Å. 2011, *A&A*, **529**, A158
- Haynes, C. J., & Kobayashi, C. 2019, *MNRAS*, **483**, 5123
- Haywood, M., Di Matteo, P., Lehnert, M. D., et al. 2018, *ApJ*, **863**, 113
- Haywood, M., Di Matteo, P., Lehnert, M. D., Katz, D., & Gómez, A. 2013, *A&A*, **560**, A109
- Heiter, U., Jofré, P., Gustafsson, B., et al. 2015, *A&A*, **582**, A49
- Hekker, S., Broomhall, A.-M., Chaplin, W. J., et al. 2010, *MNRAS*, **402**, 2049
- Hekker, S., Elsworth, Y., Mosser, B., et al. 2012, *A&A*, **544**, A90
- Hoffman, R. D., Woosley, S. E., & Qian, Y. Z. 1997, *ApJ*, **482**, 951
- Holtzman, J. A., Hasselquist, S., Shetrone, M., et al. 2018, *AJ*, **156**, 125
- Holtzman, J. A., Shetrone, M., Johnson, J. A., et al. 2015, *AJ*, **150**, 148
- Hon, M., Stello, D., & Yu, J. 2017, *MNRAS*, **469**, 4578
- Hon, M., Stello, D., & Yu, J. 2018, *MNRAS*, **476**, 3233
- Honda, S., Aoki, W., Kajino, T., et al. 2004, *ApJ*, **607**, 474
- Hotokezaka, K., Beniamini, P., & Piran, T. 2018, *IJMPD*, **27**, 1842005
- Howell, S. B., Sobeck, C., Haas, M., et al. 2014, *PASP*, **126**, 398
- Huber, D., Bedding, T. R., Stello, D., et al. 2010, *ApJ*, **723**, 1607
- Huber, D., Bryson, S. T., Haas, M. R., et al. 2016, *ApJS*, **224**, 2
- Huber, D., Ireland, M. J., Bedding, T. R., et al. 2012, *ApJ*, **760**, 32
- Huber, D., Stello, D., Bedding, T. R., et al. 2009, *CoAst*, **160**, 74
- Huber, D., Zinn, J., Bojsen-Hansen, M., et al. 2017, *ApJ*, **844**, 102
- Hunter, J. D. 2007, *CSE*, **9**, 90
- Izzard, R. G., Preece, H., Jofre, P., et al. 2018, *MNRAS*, **473**, 2984
- Jofré, P., Jorissen, A., Van Eck, S., et al. 2016, *A&A*, **595**, A60
- Johnson, J. W., Weinberg, D. H., Vincenzo, F., et al. 2021, *MNRAS*, **508**, 4484
- Jørgensen, A. C. S., Montalbán, J., Angelou, G. C., et al. 2021, *MNRAS*, **500**, 4277
- Jørgensen, A. C. S., Montalbán, J., Miglio, A., et al. 2020, *MNRAS*, **495**, 4965
- Jørgensen, B. R., & Lindegren, L. 2005, *A&A*, **436**, 127
- Kallinger, T., Beck, P. G., Stello, D., & Garcia, R. A. 2018, *A&A*, **616**, A104
- Kallinger, T., Hekker, S., Garcia, R. A., Huber, D., & Matthews, J. M. 2016, *SciA*, **2**, 1500654
- Kallinger, T., Mosser, B., Hekker, S., et al. 2010, *A&A*, **522**, A1
- Kenney, J. F., & Keeping, E. S. 1962, *Mathematics of Statistics* (3rd ed.; Princeton, NJ: Van Nostrand)
- Khan, S., Miglio, A., Mosser, B., et al. 2019, *A&A*, **628**, A35
- Kjeldsen, H., & Bedding, T. R. 1995, *A&A*, **293**, 87
- Kobayashi, C., Karakas, A. I., & Lugaro, M. 2020a, *ApJ*, **900**, 179
- Kobayashi, C., Leung, S.-C., & Nomoto, K. 2020b, *ApJ*, **895**, 138
- Kobayashi, C., & Nakasato, N. 2011, *ApJ*, **729**, 16
- Kobayashi, C., & Nomoto, K. 2009, *ApJ*, **707**, 1466
- Kobayashi, C., Tsujimoto, T., Nomoto, K., Hachisu, I., & Kato, M. 1998, *ApJL*, **503**, L155
- Kos, J., Lin, J., Zwitter, T., et al. 2017, *MNRAS*, **464**, 1259
- Lamb, S. A., Howard, W. M., Truran, J. W., & Iben, I. J. 1977, *ApJ*, **217**, 213
- Lattimer, J. M., Mackie, F., Ravenhall, D. G., & Schramm, D. N. 1977, *ApJ*, **213**, 225
- Lattimer, J. M., & Schramm, D. N. 1974, *ApJL*, **192**, L145
- Lin, J., Asplund, M., Ting, Y.-S., et al. 2020, *MNRAS*, **491**, 2043
- Lindgren, L., Hernández, J., Bombrun, A., et al. 2018, *A&A*, **616**, A2
- Luger, R., Kruse, E., Foreman-Mackey, D., Agol, E., & Saunders, N. 2018, *AJ*, **156**, 99
- Mackereth, J. T., Crain, R. A., Schiavon, R. P., et al. 2018, *MNRAS*, **477**, 5072
- Magrini, L., Spina, L., Randich, S., et al. 2018, *A&A*, **617**, A106
- Majewski, S. R., Schiavon, R. P., Frinchaboy, P. M., et al. 2017, *AJ*, **154**, 94
- Majewski, S. R., Wilson, J. C., Hearty, F., Schiavon, R. R., & Skrutskie, M. F. 2010, in *IAU Symp. 265, Chemical Abundances in the Universe: Connecting First Stars to Planets*, ed. K. Cunha, M. Spite, & B. Barbuy (Cambridge: Cambridge Univ. Press), 480
- Mamajek, E. E., Prsa, A., Torres, G., et al. 2015, arXiv:1510.07674
- Martell, S. L., Sharma, S., Buder, S., et al. 2017, *MNRAS*, **465**, 3203
- Martig, M., Minchev, I., & Flynn, C. 2014, *MNRAS*, **443**, 2452
- Martig, M., Rix, H.-W., Silva Aguirre, V., et al. 2015, *MNRAS*, **451**, 2230
- Mathur, S., García, R. A., Huber, D., et al. 2016, *ApJ*, **827**, 50
- Mathur, S., García, R. A., Régulo, C., et al. 2010, *A&A*, **511**, A46
- McKinney, W. 2010, in *Proc. of the 9th Python in Science Conf.*, ed. S. van der Walt & J. Millman, 51
- McWilliam, A. 1997, *ARA&A*, **35**, 503
- Miglio, A., Brogaard, K., Stello, D., et al. 2012, *MNRAS*, **419**, 2077
- Miglio, A., Chiappini, C., Mackereth, J. T., et al. 2021, *A&A*, **645**, A85
- Minchev, I., Martig, M., Streich, D., et al. 2015, *ApJL*, **804**, L9
- Minchev, I., Matijević, G., Hogg, D. W., et al. 2019, *MNRAS*, **487**, 3946
- Minchev, I., & Quillen, A. C. 2006, *MNRAS*, **368**, 623
- Mishenina, T., Korotin, S., Carraro, G., Kovtyukh, V. V., & Yegorova, I. A. 2013, *MNRAS*, **433**, 1436
- Mosser, B., & Appourchoux, T. 2009, *A&A*, **508**, 877
- Mosser, B., Belkacem, K., Goupil, M. J., et al. 2010, *A&A*, **517**, A22
- Mosser, B., Dziembowski, W. A., Belkacem, K., et al. 2013, *A&A*, **559**, A137
- Ness, M., Hogg, D. W., Rix, H.-W., et al. 2016, *ApJ*, **823**, 114
- Ness, M., Hogg, D. W., Rix, H. W., Ho, A. Y. Q., & Zasowski, G. 2015, *ApJ*, **808**, 16
- Newberg, H. J., Carlin, J. L., Chen, L., et al. 2012, in *ASP Conf. Ser. 458, Galactic Archaeology: Near-Field Cosmology and the Formation of the Milky Way*, ed. W. Aoki (San Francisco, CA: ASP), 405
- Nicholl, M., Smartt, S. J., Jerkstrand, A., et al. 2013, *Natur*, **502**, 346
- Nidever, D. L., Bovy, J., Bird, J. C., et al. 2014, *ApJ*, **796**, 38
- Nidever, D. L., Holtzman, J. A., Allende Prieto, C., et al. 2015, *AJ*, **150**, 173
- Nishimura, N., Sawai, H., Takiwaki, T., Yamada, S., & Thielemann, F.-K. 2017, *ApJ*, **836**, L21
- Nissen, P. E. 2015, *A&A*, **579**, A52
- Nissen, P. E., Christensen-Dalsgaard, J., Mosumgaard, J. R., et al. 2020, *A&A*, **640**, A81

- Nordström, B., Mayor, M., Andersen, J., et al. 2004, *A&A*, **418**, 989
- Pérez, F., & Granger, B. E. 2007, *CSE*, **9**, 21
- Peters, J. G. 1968, *ApJ*, **154**, 225
- Pinsonneault, M. H., Elsworth, Y. P., Tayar, J., et al. 2018, *ApJS*, **239**, 32
- Pires, S., Mathur, S., García, R. A., et al. 2015, *A&A*, **574**, A18
- Piskunov, N., & Valenti, J. A. 2017, *A&A*, **597**, A16
- Pont, F., & Eyer, L. 2004, *MNRAS*, **351**, 487
- Prochaska, J. X., Naumov, S. O., Carney, B. W., McWilliam, A., & Wolfe, A. M. 2000, *AJ*, **120**, 2513
- Qian, Y. Z., & Woosley, S. E. 1996, *ApJ*, **471**, 331
- Raiteri, C. M., Gallino, R., Busso, M., Neuberger, D., & Kaeppler, F. 1993, *ApJ*, **419**, 207
- Rendle, B. M., Miglio, A., Chiappini, C., et al. 2019, *MNRAS*, **490**, 4465
- Reyes, C., Stello, D., Hon, M., & Zinn, J. C. 2022, arXiv:2202.05478
- Ricker, G. R., Winn, J. N., Vanderspek, R., et al. 2014, *Proc. SPIE*, **9143**, 914320
- Rosswog, S., Liebendörfer, M., Thielemann, F. K., et al. 1999, *A&A*, **341**, 499
- Saha, K., Tseng, Y.-H., & Taam, R. E. 2010, *ApJ*, **721**, 1878
- Salaris, M., Chieffi, A., & Straniero, O. 1993, *ApJ*, **414**, 580
- Schönrich, R., & Aumer, M. 2017, *MNRAS*, **472**, 3979
- Schönrich, R., & Binney, J. 2009a, *MNRAS*, **396**, 203
- Schönrich, R., & Binney, J. 2009b, *MNRAS*, **399**, 1145
- Schönrich, R., McMillan, P., & Eyer, L. 2019, *MNRAS*, **487**, 3568
- Schwarzschild, M., & Härm, R. 1967, *ApJ*, **150**, 961
- Sharma, S., Hayden, M. R., Bland-Hawthorn, J., et al. 2021, *MNRAS*, **506**, 1761
- Sharma, S., & Stello, D. 2016, Asfgrid: Asteroseismic parameters for a star, Astrophysics Source Code Library, ascl:1603.009
- Sharma, S., Stello, D., Bland-Hawthorn, J., et al. 2019, *MNRAS*, **490**, 5335
- Sharma, S., Stello, D., Bland-Hawthorn, J., Huber, D., & Bedding, T. R. 2016, *ApJ*, **822**, 15
- Sharma, S., Stello, D., Buder, S., et al. 2018, *MNRAS*, **473**, 2004
- Sheinis, A., Barden, S., Birchall, M., et al. 2014, *Proc. SPIE*, **9147**, 91470Y
- Siegel, D. M., Barnes, J., & Metzger, B. D. 2019, *Natur*, **569**, 241
- Silva Aguirre, V., Bojsen-Hansen, M., Slumstrup, D., et al. 2018, *MNRAS*, **475**, 5487
- Silva Aguirre, V., Casagrande, L., Basu, S., et al. 2012, *ApJ*, **757**, 99
- Spitoni, E., Silva Aguirre, V., Matteucci, F., Calura, F., & Grisoni, V. 2019, *A&A*, **623**, A60
- Spitzer, L., Jr., & Schwarzschild, M. 1951, *ApJ*, **114**, 385
- Steffen, M., Prakapavičius, D., Caffau, E., et al. 2015, *A&A*, **583**, A57
- Steinmetz, M., Zwitter, T., Siebert, A., et al. 2006, *AJ*, **132**, 1645
- Stello, D., Chaplin, W. J., Basu, S., Elsworth, Y., & Bedding, T. R. 2009, *MNRAS*, **400**, L80
- Stello, D., Compton, D. L., Bedding, T. R., et al. 2014, *ApJL*, **788**, L10
- Stello, D., Huber, D., Sharma, S., et al. 2015, *ApJL*, **809**, L3
- Stello, D., Saunders, N., Grunblatt, S., et al. 2021, arXiv:2107.05831
- Stello, D., Zinn, J., Elsworth, Y., et al. 2017, *ApJ*, **835**, 83
- Sun, W. X., Huang, Y., Wang, H. F., et al. 2020, *ApJ*, **903**, 12
- Symbalisty, E. M. D., Schramm, D. N., & Wilson, J. R. 1985, *ApJL*, **291**, L11
- Timmes, F. X., Woosley, S. E., & Weaver, T. A. 1995, *ApJS*, **98**, 617
- Ting, Y.-S., & Rix, H.-W. 2019, *ApJ*, **878**, 21
- Tinsley, B. M. 1979, *ApJ*, **229**, 1046
- Truran, J. W., & Arnett, W. D. 1971, *Ap&SS*, **11**, 430
- Truran, J. W., Cowan, J. J., Pilachowski, C. A., & Sneden, C. 2002, *PASP*, **114**, 1293
- Ulrich, R. K. 1986, *ApJL*, **306**, L37
- Valenti, J. A., & Piskunov, N. 1996, *A&AS*, **118**, 595
- Vanderburg, A., & Johnson, J. A. 2014, *PASP*, **126**, 948
- Viani, L. S., Basu, S., Chaplin, W. J., Davies, G. R., & Elsworth, Y. 2017, *ApJ*, **843**, 11
- Virtanen, P., Gommers, R., Oliphant, T. E., et al. 2020, *NatMe*, **17**, 261
- Vlasov, A. D., Metzger, B. D., & Thompson, T. A. 2014, *MNRAS*, **444**, 3537
- Walt, S. 2011, *CSE*, **13**, 22
- Wanajo, S., Janka, H.-T., & Müller, B. 2011, *ApJL*, **726**, L15
- Warfield, J. T., Zinn, J. C., Pinsonneault, M. H., et al. 2021, *AJ*, **161**, 100
- Weinberg, D. H., Holtzman, J. A., Havelquist, S., et al. 2019, *ApJ*, **874**, 102
- White, T. R., Bedding, T. R., Stello, D., et al. 2011, *ApJ*, **743**, 161
- Wilson, J. C., Hearty, F. R., Skrutskie, M. F., et al. 2019, *PASP*, **131**, 055001
- Wittenmyer, R. A., Sharma, S., Stello, D., et al. 2018, *AJ*, **155**, 84
- Wolniewicz, L. M., Berger, T. A., & Huber, D. 2021, *AJ*, **161**, 231
- Yanny, B., Rockosi, C., Newberg, H. J., et al. 2009, *AJ*, **137**, 4377
- Yıldız, M., Çelik Orhan, Z., & Kayhan, C. 2016, *MNRAS*, **462**, 1577
- Yu, J., Huber, D., Bedding, T. R., et al. 2018, *ApJS*, **236**, 42
- Zasowski, G., Cohen, R. E., Chojnowski, S. D., et al. 2017, *AJ*, **154**, 198
- Zasowski, G., Johnson, J. A., Frinchaboy, P. M., et al. 2013, *AJ*, **146**, 81
- Zhao, G., Mashonkina, L., Yan, H. L., et al. 2016, *ApJ*, **833**, 225
- Zhou, Y., Asplund, M., Collet, R., & Joyce, M. 2020, *MNRAS*, **495**, 4904
- Zinn, J. C., Huber, D., Pinsonneault, M. H., & Stello, D. 2017, *ApJ*, **844**, 166
- Zinn, J. C., Pinsonneault, M. H., Huber, D., et al. 2019b, *ApJ*, **885**, 166
- Zinn, J. C., Pinsonneault, M. H., Huber, D., & Stello, D. 2019a, *ApJ*, **878**, 136
- Zinn, J. C., Stello, D., Elsworth, Y., et al. 2020, *ApJS*, **251**, 23
- Zinn, J. C., Stello, D., Huber, D., & Sharma, S. 2019c, *ApJ*, **884**, 107